

UNIVERSITY OF BERGEN



Department of Physics and Technology

MASTER'S THESIS IN OCEAN TECHNOLOGY

**Estimation and Verification of Hydrodynamic
Parameters of an ROV using CFD**

By:

Oskar Voldsund

June 2023

Abstract

The hydrodynamic added mass and damping of a Remotely Operated Vehicle (ROV) are estimated using Computational Fluid Dynamics (CFD) based on OpenFOAM. The estimated hydrodynamic parameters are verified with recorded data from an operating ROV at Snorre B (SNB). Then, the added mass and damping are adjusted to assess if a more accurate fit with the recorded data can be obtained.

The ROV under investigation is the Merlin UCV, a work-class ROV. The UCV is first simplified to perform CFD. Two simplified versions are made, and the thin side plates are included in the more complex version. Two mesh convergence studies are conducted to verify the mesh and the computational domain. The Reynolds number is set to be 2.25×10^6 . Numerical simulation based on Steady- and Unsteady-Reynolds-Averaged Navier–Stokes combined with the $k-\omega$ Shear Stress Transport (SST) turbulence model are performed to obtain the hydrodynamic parameters. By studying the influence of the side plates, it is found that the drag increases considerably when the plates are directly exposed to the flow. When there is a constant flow in sway, the value of C_d is 1.4682 when the side plates are not considered. However, when side plates are introduced, the value of C_d increases by 15 % to 1.6880.

Three different experiments are recreated numerically to find the added mass and damping in all Degrees Of Freedom (DOF) as a result of respective acceleration and constant velocity in the corresponding direction. The first numerical simulation is the towing tank test conducted to find the damping in the translational directions. Steady-Reynolds-Averaged Navier–Stokes (RANS) is used, and a constant velocity in the applicable directions are implemented. Then, rotating arm simulations are conducted to find the damping in the rotational directions. A similar procedure is used for the towing tank simulations, but a constant angular velocity is implemented. Planar Motion Mechanism (PMM) simulations are performed to obtain the added mass and inertia in all 6 DOF. Oscillatory linear and angular movements are executed to find the added mass and inertia in the translational and rotational directions. Since the movement is oscillatory, Unsteady-Reynolds-Averaged Navier–Stokes (URANS) is used to capture the time-varying flow.

Furthermore, the numerical model used to estimate hydrodynamic parameters is validated by being compared to recorded data of an operational ROV at SNB. The recorded data were logged using the SPRINT, consisting of linear and angular position and velocity. A simulator

code built on the classical equations of motion is made to simulate the movement data. Moreover, the CFD estimated added mass and damping are implemented in the equations. In the present study, the simulated movement of the ROV is later fitted with the recorded data. The fit between the recorded and simulated movement is satisfactory using the CFD estimated parameters. The added mass and damping are then adjusted, and an improved fit with the recorded data is achievable. Therefore, the conclusion is to adjust the hydrodynamic parameters if recorded data is available. This method is more efficient than CFD and gives more accurate results. However, if recorded data is unavailable, CFD can provide an efficient method to accurately predict the damping and added mass.

Acknowledgment

This thesis is the result of my Master's research in Ocean Technology (HTEK399) at the University of Bergen (UiB) during the spring of 2023, comprising 60 ECTS.

I would like to express my sincere gratitude to Dr. Guang Yin for his unwavering support, guidance, and patience throughout my research journey. His expertise in the field and willingness to go above and beyond have been invaluable in shaping my work and helping me overcome any challenges I faced. I also want to thank Professor Muk Chen Ong for facilitating the cooperation between IKM Subsea, UiS, and myself, ensuring the success of this project.

My heartfelt appreciation goes to IKM Subsea for providing me with the opportunity to undertake this project. Ments Tore Møller, the driving force behind this collaboration, your support and cooperation were indispensable in completing this thesis. Håkon Teigland, your expertise and willingness to assist have been invaluable, and I sincerely appreciate your guidance throughout the project. Sigbjørn Slettebø, thank you for your assistance and insightful discussions.

I extend my gratitude to Professor Bjørn Tore Hjertaker for his unwavering support and availability. Your guidance helped me navigate the challenges. I would also like to thank my fellow students for their support and shared experiences over the past five years. To my family and partner, thank you for your unwavering support throughout this journey.

Bergen, June 2023

Oskar Voldsund

Contents

Abstract	ii
Acknowledgment	iii
List of Figures	vii
List of Tables	ix
1 Introduction	1
1.1 Objective of Thesis	1
1.2 Merlin UCV	3
1.3 Previous Work	5
1.4 Thesis Structure	7
2 Theoretical Background	9
2.1 Flow Around Bluff Bodies	9
2.2 Reynolds Number	11
2.3 Navier–Stokes Equations	12
2.4 Hydrodynamic forces	13
2.5 Computational Fluid Dynamics	14
2.5.1 OpenFOAM	14
2.5.2 Steady-Reynolds-Averaged Navier–Stokes	15
2.5.3 Unsteady-Reynolds-Averaged Navier–Stokes	15
2.5.4 $k - \omega$ Shear Stress Transport Turbulence Model	16
2.5.5 Law of the Wall	17
2.6 ROV Motion	20
2.6.1 Reference Frames	20

2.6.2	Kinematic	21
2.6.3	6 DOF Equations of Motion	22
2.7	Calculations of Hydrodynamic Parameters	27
2.7.1	Hydrodynamic Damping	27
2.7.2	Hydrodynamic Added Mass and Inertia	28
2.8	Instrumentation	32
2.8.1	SPRINT-Nav 500	32
2.8.2	Model 803 ROV Current Meter	34
3	Methodology	35
3.1	Numerical Modeling	36
3.1.1	3D Model	37
3.1.2	Computational Domain	38
3.1.3	Mesh	42
3.2	Experimental Method and Validation	46
4	Results and Discussion	49
4.1	Mesh Convergence Study	50
4.1.1	Comparison of the Hydrodynamic Forces of V1 and V2	52
4.2	Towing Tank Simulation	53
4.2.1	Surge	53
4.2.2	Sway	55
4.2.3	Heave	57
4.3	Rotation Arm Simulation	60
4.3.1	Roll	60
4.3.2	Pitch	62
4.3.3	Yaw	64
4.4	Planar Motion Mechanism Simulation	68
4.4.1	Surge	68
4.4.2	Sway	71
4.4.3	Heave	73
4.4.4	Roll	76
4.4.5	Pitch	79

- 4.4.6 Yaw 81
- 4.5 Validation with Operational ROV 84
 - 4.5.1 Validation of the Translational Directions 85
 - 4.5.2 Validation of the Rotational Directions 87
 - 4.5.3 Adjustment of the Hydrodynamic Parameters 90
- 4.6 Main Discussion 94

- 5 Conclusion 99**
 - 5.1 Suggestions for Future Work 101

- References 102**

List of Figures

1.1	Overview photo of the ROV, Merlin UCV	4
2.1	Drag coefficient together with the UCV	10
2.2	Behavior of flow near the wall (red line), together with two empirical wall functions	18
2.3	Definition of the BODY and NED reference system	20
2.4	Picture of the a general SPRINT-Nav	33
2.5	Picture of the current meter	34
3.1	Difference between detailed ROV model and simplified versions	38
3.2	Domain used for towing tank and PMM simulations	39
3.3	Domain used for the rotating arm simulations	41
3.4	An example of the mesh for the two versions in the present study	43
3.5	Circular mesh when the angular flow is in yaw	44
3.6	Dynamic oscillating mesh in the XZ-plane	45
3.7	Overview of the OCC	46
4.1	The results of C_d for different numbers of meshes with an incoming flow in the surge direction	50
4.2	The results of C_d for different numbers of meshes with an incoming flow in the sway direction	51
4.3	Contours of the stream-wise velocity and the pressure under the incoming flow velocity of 1 m/s	54
4.4	The linear and quadratic damping in surge found by using polyfit in MATLAB	55
4.5	Contours of the stream-wise velocity and the distributed pressure under the incoming flow velocity of 1 m/s	56

4.6	The linear and quadratic damping in sway found by using polyfit in MATLAB . . .	57
4.7	Contours of the stream-wise velocity and the pressure distributed under the incoming flow velocity of 1 m/s in heave	58
4.8	The linear and quadratic damping in heave found by using polyfit in MATLAB . .	59
4.9	Contours of the flow velocity and the distributed pressure, 0.2 rad/s	61
4.10	The linear and quadratic damping in roll found by using polyfit in MATLAB . .	62
4.11	Contours of the flow velocity and the distributed pressure, 0.2 rad/s	63
4.12	The linear and quadratic damping in pitch found by using polyfit in MATLAB . .	64
4.13	Contours of the flow velocity and the distributed pressure, 0.2 rad/s	65
4.14	The linear and quadratic damping in yaw found by using polyfit in MATLAB . .	66
4.15	Vorticity and pressure as a result of an oscillating movement in surge with an oscillating frequency of $f = 0.6$ Hz	69
4.16	Added mass in surge for the different frequencies	70
4.17	Vorticity as a result of an oscillating movement in sway with an oscillating frequency of $f = 0.6$ Hz	72
4.18	Vorticity as a result of an oscillating movement in heave with an oscillating frequency of $f = 0.6$ Hz	74
4.19	The vorticity and pressure measured at the representative stages of the roll motion with an oscillating frequency of $f = 0.5$ Hz	77
4.20	Added inertia in roll for the different frequencies	79
4.21	The vortex intensity measured at the representative stages of the pitch motion with an oscillating frequency of $f = 0.5$ Hz	80
4.22	The vortex intensity measured at the representative stages of the yaw motion with an oscillating frequency of $f = 0.5$ Hz	82
4.23	Logged and simulated position and velocity in heave	85
4.24	Logged and simulated velocity in surge and sway	87
4.25	Logged and simulated positions and angular velocities in the rotational directions	88
4.26	Logged and simulated data for the position in heave and velocities in sway and heave using adjusted hydrodynamic parameters	91
4.27	Logged and simulated data for the velocity in pitch and yaw using adjusted hydrodynamic parameters	92

List of Tables

1.1	Merlin UCV technical specifications	4
2.1	The different notations used for the DOF p. 16]Fossen2011	20
2.2	Performance and accuracy for the SPRINT-Nav 500	34
2.3	Performance and accuracy for the current meter	34
4.1	The results of y^+ for different number of meshes	51
4.2	The results of y^+ for different number of meshes	52
4.3	Comparison of V1 and V2 by studying the drag coefficient and drag force	52

List of Abbreviations

- CB** Center of Buoyancy
- CFD** Computational Fluid Dynamics
- CO** Center of Origin
- CPU** Central Processing Unit
- DOF** Degrees Of Freedom
- DP** Dynamic Positioning
- DVL** Doppler Velocity Log
- FVM** Finite Volume Method
- HPC** High Performance Computing
- HVL** Western Norway University of Applied Sciences
- INS** Inertial Navigation System
- MRF** Multiple Reference Frames
- NED** North East Down
- NS** Navier-Stokes
- OCC** Onshore Control Center
- PISO** Pressure Implicit with Splitting of Operators
- PMM** Planar Motion Mechanism
- RANS** Reynolds-Averaged Navier–Stokes
- ROV** Remotely Operated Vehicle
- RPM** Rounds Per Minute

SIMPLE Semi-Implicit Method for Pressure-Linked Equations

SNB Snorre B

SST Shear Stress Transport

UCV Ultra Compact Vehicle

UiB University of Bergen

UiS University of Stavanger

URANS Unsteady-Reynolds-Averaged Navier–Stokes

Chapter 1

Introduction

1.1 Objective of Thesis

The thesis aims to develop a reliable and realistic Remotely Operated Vehicle (ROV) simulator code by improving the hydrodynamic quantities estimations for IKM Subsea. The simulator trains inexperienced pilots in different operation cases and tests new technology. However, the existing simulator needs to be updated. Experienced ROV pilots and engineers have reported that the simulator does not act like the real ROV [1]. Improving these capabilities is crucial for enhancing operators' preparedness and safety while operating the actual ROV. Moreover, the current technology testing validity needs to be improved, highlighting the need to address these factors. Hence, this work aims to improve these capabilities.

The old and new simulator is built on the classical equations of motion, presented in Chapter 2. The added mass and damping matrices are essential in the equations to determine the ROV motion and are of main interest. However, the value of added mass and damping were estimated using simplifications and updated using feedback from ROV pilots for the existing simulator. First, the simplifications were implemented, and then the ROV pilots tested the simulator. Finally, the added mass and damping of the existing ROV simulator were adjusted to match the motion feedback reported by the ROV pilots. This method is highly based on intuition and not systematic.

This work uses Computational Fluid Dynamics (CFD) to find the unknown parameters. The resulting parameters will then be implemented in the simulator code and validated, compared with data recorded from a real ROV operating from Equinor's Snorre B (SNB). The estimated

added mass and damping will then serve as the base for adjusting the parameters to assess if more accurate simulated data can be achieved. The intent is to assess if the method can lead to a more accurate and realistic ROV simulator than the conventional method.

To the author's knowledge, although ROV simulators have previously been developed using CFD [2], the numerical results have not been compared to the data of an ROV in operation. If successful, this method can improve the accuracy of the ROV simulator and pave the way for developing digital twins for existing ROVs. The virtual ROV can monitor, predict and improve the performance of the ROV digitally, allowing for the testing of new technologies and systems without the need to take the ROV out of operation or send engineers offshore [3].

Suppose the estimated parameters from the CFD simulations match the recorded data. In that case, this method can also be used to develop a digital prototype of new ROVs and test them under various scenarios, resulting in a more time- and cost-efficient development procedure. The same CFD analyses could be carried out, and a new vehicle could be introduced as a digital twin before construction. If the thesis results are positive, this method may revolutionize the development of ROVs.

1.2 Merlin UCV

In this thesis, the IKM Subsea Merlin UCV is simulated using CFD. UCV is short for Ultra Compact Vehicle and is an ROV. An ROV makes it possible to get live video underwater, and the vehicle can be used for different purposes, such as surveys, valve operations, and subsea lift operations. It is connected to the surface through a tether cable for real-time control. The ROV is often controlled from a ship or a platform.

Since the ROV can be used for many different purposes, there are different types of ROVs. The Merlin UCV is a work-class ROV, and this type of ROV is one of the larger ROVs and can perform complex and demanding operations. It can be equipped with various tools and equipment, such as manipulators, skids, torque tools, cutting tools, and subsea saws. The UCV has both interfaces for electrical and hydraulic-operated tooling. Regardless, the UCV is superior in lifting and power compared to similar work-class ROVs [1] [4].

When operating an ROV, a considerable challenge is managing the tether. The tether is both vulnerable and critical to the system. Most ROVs implement a tether management system (TMS) to address this challenge. This system typically consists of a winch that spools and unspools the tether to gain control of the tether. One way to control the tether is using an E-cage, as implemented in the ROV described in this work. The cage is stationary on the seabed, which provides several advantages, such as the ability to stay submerged for an extended period and a fixed, known position. Besides, engineers can mount sensors such as current meters on the TMS to measure current and other parameters [1] [4]. Figure 1.1 shows a photo of the ROV.

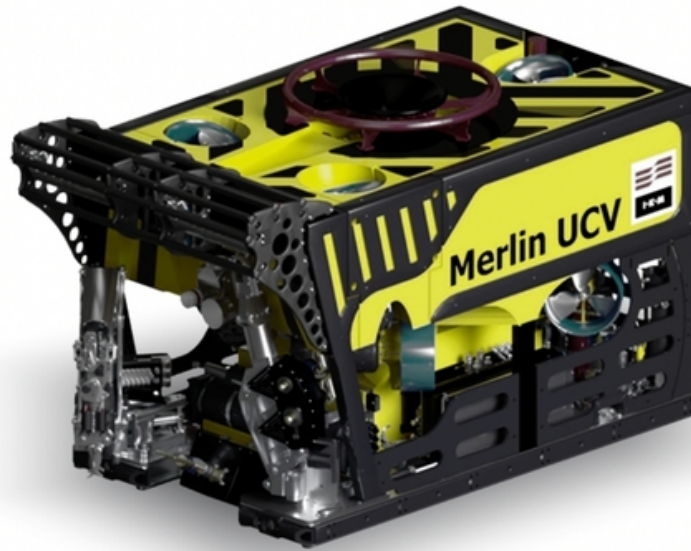


Figure 1.1: Overview photo of the ROV, Merlin UCV [5]

The Merlin UCV ROV has seven thrusters, three vertical and four horizontal. It has two manipulators installed, specifically a Schilling Robotics TITAN 4 Manipulator on the starboard side and a Schilling Robotics RigMaster on the port side. For navigation, the UCV is implemented with the SPRINT-Nav 500 with Syrinx Doppler Velocity Log (DVL) [1] [4]. Table 1.1 provides the ROV specifications.

Table 1.1: Merlin UCV technical specifications [1] [4]

Dimensions	Symbol	Value
Length	L	2.5 m
Width	W	1.5 m
Height	H	1.5 m
Weight	m	2750.0 kg
Angular mass, x-axis	I_x	1223.2 kg m ²
Angular mass, y-axis	I_y	2234.3 kg m ²
Angular mass, z-axis	I_z	2125.2 kg m ²

1.3 Previous Work

A thesis was completed by S.Skorpa (2012) to study the IKM Subsea WR200 using CFD. The flow around a simplified ROV was simulated using detached eddy simulations and the $k-\omega$ Shear Stress Transport (SST) turbulence model. The simulations were carried out at a Reynolds number of 8.5×10^5 , corresponding to a free stream velocity of one knot, which is a reasonable cruising speed of the ROV. The CFD code ANSYS Fluent was used. The stability of the ROV was studied, and the reported issues were also found in the numerical results. The author suggested two CFD-related topics for further work. It is suggested to perform further numerical simulations to study the effect of components on the stability. The other is to study the instability in sway. To this date, these topics still need to be completed [6]. In recent years, IKM Subsea made a new ROV, the UCV, and this ROV is prioritized. As known, IKM Subsea are investigating upgrading their ROV simulator for the UCV [1]. Therefore, a comprehensive investigation should be conducted to find the hydrodynamic damping and added mass.

In recent years, Q. Li et al. (2020) have done more relevant studies, which simulated the flow around a simplified BlueRov2. This study obtains hydrodynamic damping in its four principal Degrees Of Freedom (DOF). The numerical model employed a Reynolds-Averaged Navier-Stokes solver and was validated compared to experimental measurements of hydrodynamic forces and moments obtained. The study found that the numerical model was reliable in estimating the hydrodynamic damping in the four DOF. The proposed methodologies and techniques could be applied to other ROVs [7].

This study only calculates the hydrodynamic damping, but obtaining the hydrodynamic added mass and inertia is also necessary. Another recent study by L. Hong et al. (2022) estimate the translational and rotational damping and added mass. This study used numerical simulations to estimate an underactuated underwater vehicle's hydrodynamic coefficients using CFD. The study established the numerical model of the underwater vehicle and carried out steady- and unsteady-RANS simulations. The towing tank, rotating arm, and Planar Motion Mechanism (PMM) tests were simulated to calculate the vehicle's damping and added mass. The study used a sliding mesh model to simulate the PMM tests to recreate the vehicle's unsteady motions. The study validated the estimated hydrodynamic coefficients through an experiment and found that the numerical estimations agreed with the experimental data. The study also concluded that the proposed numerical methods could be applied to other

underwater vehicles to estimate the hydrodynamic damping and added mass [8].

A study by A. Hammoud et al. (2021) proposed another numerical method to estimate the damping of an ROV in the rotational DOF. The computational domain used in the simulations consists of two cylinders, with the smaller cylinder containing the ROV and rotating at an angular velocity while the larger cylinder remains steady. The two cylinders are interfaced using Multiple Reference Frames (MRF) available in ANSYS Fluent. The rotational moments were obtained in these simulations. The damping for the rotational directions was obtained by fitting a quadratic function to the moment and the corresponding angular velocities. The linear terms in the damping matrix were negligible at low velocities. This approach provides an accurate and efficient way to estimate the damping in the rotational direction of an ROV [9].

In this work, to validate the results of the numerical simulations, the movement of the ROV will be simulated using the equations of motion with the estimated parameters obtained through CFD. The results will then be compared to log data from an operational ROV at SNB. Similar work has been done previously, but comparing the simulated movement with CFD estimated parameters to an ROV in operation has not been done before. In cooperation with IKM Subsea, a thesis was completed by L. M. Knausgård (2013), where the same equations were used to develop a dynamic positioning system for the WR200. In the thesis, the Dynamic Positioning (DP) system was modeled, developed, and implemented for the WR200. The system was tested and validated by completing a sea trial. Making a DP system increases the pilot's and ROV's efficiency, reliability, and endurance. However, more work was needed before it could be installed as a control system for operational use. The thesis also concluded with the importance of accurate models for the controller [3].

1.4 Thesis Structure

In Chapter 2, the theoretical basis of the thesis is introduced. The main focus of Chapter 2 is the introduction of general fluid dynamics, CFD, and the motion of the ROV.

Chapter 3 describes the different methods used in the thesis. The methodology is divided into two different principal parts of this work. The first part is the numerical method. Here, the numerical model is presented, and the procedures for calculating the different hydrodynamic parameters are presented. The second part is the experimental method. A sea test at SNB is performed to validate the numerical results, and a simulator code built on the equations of motion is developed. The numerical results are used to simulate the movement of the ROV and then compared to the recorded data.

Chapter 4 presents the results with discussion. The chapter presents the results from the estimation of hydrodynamic parameters using CFD. Three different experiments are recreated numerically: the towing tank test, the rotating arm test, and the PMM test. Furthermore, the numerical results are compared to recorded data from the ROV in operations. Toward the end of the chapter, the added mass and damping are adjusted to achieve the best possible match between the simulated movement and the recorded data.

Chapter 5 is the final chapter of the thesis. The chapter concludes the findings of the thesis and recommends what problems should be looked at more thoroughly to build on the scientific findings.

(This page is intentionally left blank)



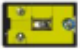























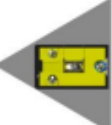

















Chapter 2

Theoretical Background

2.1 Flow Around Bluff Bodies

The study of flow around bluff bodies is a fundamental aspect of CFD. The drag coefficient, C_d , is a dimensionless number representing the resistance of a fluid to the motion of a body. It plays a crucial role in determining the performance of an ROV, and it depends on various factors, such as fluid density, velocity, and body shape [10].

Various methods are available to measure the drag coefficient of an ROV, including wind tunnel testing [11], CFD simulation [6], and testing in a towing tank [7]. Regardless of the method used, it is crucial to determine the drag coefficient as accurately as possible to understand and improve the performance of the ROV in fluid flow. Accurate estimation of the drag coefficient is essential in practical applications, such as optimizing the ROV's speed and energy consumption, stability, and maneuverability. Figure 2.1 shows the drag coefficient for different bluff bodies, and the information is gathered from [10].

DESCRIPTION	SHAPE	UCV PROFILE	UCV PLAN	UCV SECTION	DRAG COEFFICIENT
Cube/Cuboid					1.05
Sphere					0.47
Hollow hemisphere					0.38
Solid hemisphere					0.42
Ellipse					0.59
Cube/Cuboid rotated					0.80
60° cone					0.50
Reversed solid hemisphere					1.17
Long cylinder					0.82
Short cylinder					1.15
Streamlined body					0.04


Flow Direction 

Figure 2.1: Drag coefficient together with the UCV [1] [10]

To estimate the drag coefficient of the present investigated ROV, comparing the shape and data to the different bluff bodies in Figure 2.1 is helpful. The ROV has a cuboid shape with a typical drag coefficient of 1.05. However, it is important to note that the present ROV has unique characteristics and differences from the bluff bodies in Figure 2.1. Therefore, the actual coefficient is expected to differ from this value.

2.2 Reynolds Number

The Reynolds number is an essential dimensionless value in fluid dynamics. It is defined as the ratio between inertial forces and viscous forces in a flow and is expressed as:

$$Re = \frac{uL}{\nu} \quad (2.1)$$

In this work, u is the characteristic fluid flow velocity, L is the characteristic height of the ROV, and ν is the kinematic viscosity of the fluid. The Reynolds number is used to predict the expected behavior of the flow. When the Reynolds number is low, the flow is considered laminar. However, when it is high, it becomes turbulent. There is no exact threshold for when the flow is laminar and when it is turbulent. There exist different criteria and one from [12, p. 324] state that:

- Laminar flow, $Re < 2300$
- Transition region, $2300 < Re < 4000$
- Turbulent flow, $Re > 4000$

When performing CFD, the Reynolds number is also an important parameter. If the flow is turbulent, a suitable turbulence model should be chosen. For investigating the flow around an ROV, the flow is assumed to be turbulent under high Re . Therefore, a turbulence model is adopted and will be described in this chapter.

2.3 Navier–Stokes Equations

The Navier-Stokes (NS) equations are the partial differential equations describing the motion of the fluid. The equation for the conservation of mass is as follows:

$$\nabla \cdot \mathbf{U} = 0 \quad (2.2)$$

The equation for the conservation of momentum is:

$$\rho \frac{D\mathbf{U}}{Dt} = -\nabla p + \rho \mathbf{g} + \mu \nabla^2 \mathbf{V} \quad (2.3)$$

where \mathbf{U} is the vector of the 3D flow velocity, ρ is the density of the fluid, t is the time, and p is the pressure of the fluids. The gravitational force vector is represented as \mathbf{g} , and the dynamic fluid viscosity is μ [12, p. 426-431]. The Navier-Stokes equations are crucial in understanding and simulating fluid flow in various applications, including in the design and optimization of ROVs. The accuracy of CFD simulations depends on the ability to solve the Navier-Stokes equations.

2.4 Hydrodynamic forces

The drag force is crucial to determine the performance of the ROV and will be the center of the present study. This force is obtained by integrating the pressure and the viscous stress on the ROV surface, given by Equation 2.4.

$$F_d = \int_A (-p \cos \theta_n + \tau_w \sin \theta_n) dA \quad (2.4)$$

Here, the area is represented by A , and p is the pressure. θ_n is the angle between the normal vector of the area and the positive flow direction. The Surface shear stress caused by the viscous forces is represented by τ_w [12, p. 564]. A disadvantage of relying solely on the drag force is that it has dimensions and can vary based on factors such as the velocity of the flow and the surface area. A solution to this problem is to use the drag coefficient C_d , which is dimensionless and eliminates the influence of cross-section area, density, and velocity. Using the drag coefficient makes comparing and analyzing results obtained from different sources easier. The equation for obtaining the drag coefficient is given as follows:

$$C_d = \frac{F_d}{\frac{1}{2} \rho A u^2} \quad (2.5)$$

Here, the density of the fluid is represented by ρ , the cross-section area subjected to the incoming flow as A , and the characteristic flow velocity is u [12, p. 287]. In fluid and computational fluid dynamics, accurately predicting the drag coefficient of a body is essential to understand the behavior of the flow around the body and how it affects the overall performance. The drag coefficient is also crucial to understand when performing design optimization and predicting the performance of new designs.

2.5 Computational Fluid Dynamics

CFD, short for Computational Fluid Dynamics, is a numerical method for solving complex fluid problems. CFD uses computers to numerically solve the NS equations presented in Equation 2.2 and 2.3, since there is almost no analytical solution to the equations. Turbulence, often a part of the solutions to the equations, is one of many unsolved problems in physics.

CFD is a method that can solve partial differential equations such as Steady- and Unsteady-Reynolds-Averaged Navier–Stokes presented respectively in Equation 2.6/2.7 and 2.8/2.9. The approach is to discretize the partial differential equations into a set of algebraic equations by dividing the computational domain into cells/elements to solve these equations. The flow quantities are predicted at the cell center of each element, and an approximation of the NS equations is made. The method used to solve the NS equations is typically the Finite Volume Method (FVM). This method integrates the equations over each cell and calculates the flow change for each timestep. CFD has become a powerful tool in engineering and design optimization by providing insight into the behavior of fluids [13].

2.5.1 OpenFOAM

OpenFOAM is an open-source CFD toolbox short for Open Field Operation And Manipulation. OpenFOAM has many users in most areas of engineering and science, both academically and commercially. It has many features to solve various engineering problems, from complex fluid problems involving chemical reactions, turbulence, and heat transfer to acoustics, solid mechanics, and electromagnetics [13].

This software runs on the operating system Linux and is written in C++. To run simulations using OpenFOAM, a case must contain at least three folders: *0*, *constant*, and *system*. The *0* folder contains the initial and boundary conditions of the case. The *constant* folder consists of the turbulence properties, the mesh, and the physical properties of the fluid. The *system* folder controls the simulations and determines the discretization schemes and the numerical methods. A *postProcessing* folder will be created when the case is running. This folder will contain the results, such as the hydrodynamic quantities of the simulations. The flow velocities and pressure solutions will be generated and named after the timesteps during simulations. Then, the present study uses Paraview, an open-source data analysis and visualization program to inspect the simulation results [13].

2.5.2 Steady-Reynolds-Averaged Navier–Stokes

Steady-Reynolds-Averaged Navier–Stokes (RANS) approximates the original Navier-Stokes equations. The Reynolds decomposition of the flow field assumes that the pressure and velocity can be decomposed into fluctuating and time-averaged components. The numerical solution of the flow field using the steady RANS equations represents an average flow field behavior, and the time capture is not in real-time [14].

The equation for the conservation of mass and momentum for incompressible fluid is given respectively in Equation 2.6 and 2.7.

$$\frac{\partial \bar{u}_i}{\partial x_i} = 0 \quad (2.6)$$

$$\bar{u}_j \frac{\partial \bar{u}_i}{\partial x_j} = -\frac{1}{\rho} \frac{\partial \bar{p}}{\partial x_i} + \nu \frac{\partial^2 \bar{u}_i}{\partial x_j \partial x_j} - \frac{\partial \overline{u'_i u'_j}}{\partial x_j} \quad (2.7)$$

In these equations, $i, j = 1, 2, 3$, x_1 is the flow direction, and x_2 and x_3 are both cross-flow directions. The X-, Y-, and Z-direction is symbolized as x_1 , x_2 , and x_3 . The three Reynolds averaged velocity components are \bar{u}_1 and \bar{u}_2 , \bar{u}_3 . The fluid density is ρ , and the pressure is p . The kinematic viscosity is ν and $\overline{u'_i u'_j}$ is the Reynolds stress [15].

2.5.3 Unsteady-Reynolds-Averaged Navier–Stokes

Unsteady-Reynolds-Averaged Navier–Stokes (URANS) simulations are also carried out in the present study to capture the time-dependent flow. These equations are another approximation of the original Navier-Stokes equations, and this approach can be used to study unsteady phenomena such as vortex shedding.

This thesis uses the SIMPLE algorithm, Semi-Implicit Method for Pressure-Linked Equations, and the PIMPLE algorithm. PIMPLE combines the SIMPLE and PISO, Pressure Implicit with Splitting of Operators, algorithm. SIMPLE is used for the Steady-RANS simulations, and PIMPLE is used for the Unsteady-RANS simulations. The SIMPLE and PIMPLE algorithms are iterative procedures to solve NS equations for the pressure and velocity fields. It is based on decomposing the momentum equation into two steps. First, the momentum equation is solved to obtain the predicted flow velocity results. Then, a Laplacian equation is solved for

the pressure to fulfill the mass conservation equation [13].

The equation for conservation of mass and momentum for incompressible fluid of URANS is given respectively in Equation 2.8 and 2.9.

$$\frac{\partial \bar{u}_i}{\partial x_i} = 0 \quad (2.8)$$

$$\frac{\partial \bar{u}_i}{\partial t} + \bar{u}_j \frac{\partial \bar{u}_i}{\partial x_j} = -\frac{1}{\rho} \frac{\partial \bar{p}}{\partial x_i} + \nu \frac{\partial^2 \bar{u}_i}{\partial x_j \partial x_j} - \frac{\partial \overline{u'_i u'_j}}{\partial x_j} \quad (2.9)$$

The new component in the equation, compared to the Steady- RANS, is the time-dependent term, $\frac{\partial \bar{u}_i}{\partial t}$. The rest of the symbols is the same as the Steady-RANS equations [15]. An important condition when carrying out URANS simulations is the Courant–Friedrichs–Lewy condition, which governs the stability of the simulation and must be fulfilled. The equation for the Courant number is presented in Equation 2.10.

$$C = \frac{u \Delta t}{\Delta x} \leq C_{MAX} \quad (2.10)$$

Here, u is the local velocity within the cell, Δt is the timestep, and Δx is the characteristic length of the cell. This condition indicates the stability of the simulation. C is the Courant number and should not exceed the value of 1, and the magnitude of the number differs under different meshes. When choosing the appropriate mesh, choosing the timestep with care is crucial to fulfill the condition and achieve a stable simulation [7] [13].

2.5.4 $k - \omega$ Shear Stress Transport Turbulence Model

Turbulence models are applied to resolve the Reynolds stress of the turbulent flow. The present study uses the $k - \omega$ Shear Stress Transport (SST) turbulence model. This turbulence model contains a blend function and combines the $k - \epsilon$ and the $k - \omega$ turbulence model. The first turbulence model is used in the far field, and the second in the near-wall region. This shift of turbulence models is beneficial since the different models perform differently in resolving turbulence characteristics. The $k - \omega$ is more accurate in the near wall region compared to $k - \epsilon$. However, $k - \omega$ experiences sensitivity for ω values in the far field. The $k - \epsilon$ model has good performances in the far field and is therefore implemented in the far

field using the blend [16].

The k is the turbulent kinetic energy, and the ω is the specific dissipation rate. Both transport equations are presented respectively in Equation 2.11 and 2.12 [16] [17].

$$\frac{\partial(\rho k)}{\partial t} + \frac{\partial(\rho U_i k)}{\partial x_i} = \tilde{P}_k - \beta^* \rho k \omega + \frac{\partial}{\partial x_i} \left((\mu + \sigma_k \mu_t) \frac{\partial k}{\partial x_i} \right) \quad (2.11)$$

$$\frac{\partial(\rho \omega)}{\partial t} + \frac{\partial(\rho U_i \omega)}{\partial x_i} = \alpha \rho S^2 - \beta \rho \omega^2 + \frac{\partial}{\partial x_i} \left((\mu + \sigma_\omega \mu_t) \frac{\partial \omega}{\partial x_i} \right) + 2(1 - F_1) \rho \sigma_{\omega 2} \frac{1}{\omega} \frac{\partial k}{\partial x_i} \frac{\partial \omega}{\partial x_i} \quad (2.12)$$

In these two equations, ρ is the fluid density, and the production limiter of the model is \tilde{P}_k and prevents the build-up of turbulence in stagnation regions. S is the invariant measure of the strain rate, and β^* , α , β , σ_k , σ_ω , and $\sigma_{\omega 2}$ are model constants. The blend function makes the shift between k - ϵ and the k - ω turbulence models possible. This function is symbolized as F_1 [16].

2.5.5 Law of the Wall

This study uses a Spalding wall function to resolve the near-wall boundary layer. Wall functions are needed because of the large velocity gradient in the near-wall region. A fine mesh must be made near the wall to resolve the velocity gradient, which is inconvenient due to the increase in the mesh number. Therefore, the law of the wall for the velocity is employed. This law states the relationship between the Reynolds-averaged velocity in the flow direction and the distance from the wall [18].

Understanding how the flow behaves near the wall is crucial to propose a wall function. Over the years, many numerical simulations and experiments have been carried out to predict the behavior of the flow near the wall, and the simulation results give a velocity profile shown in Figure 2.2.

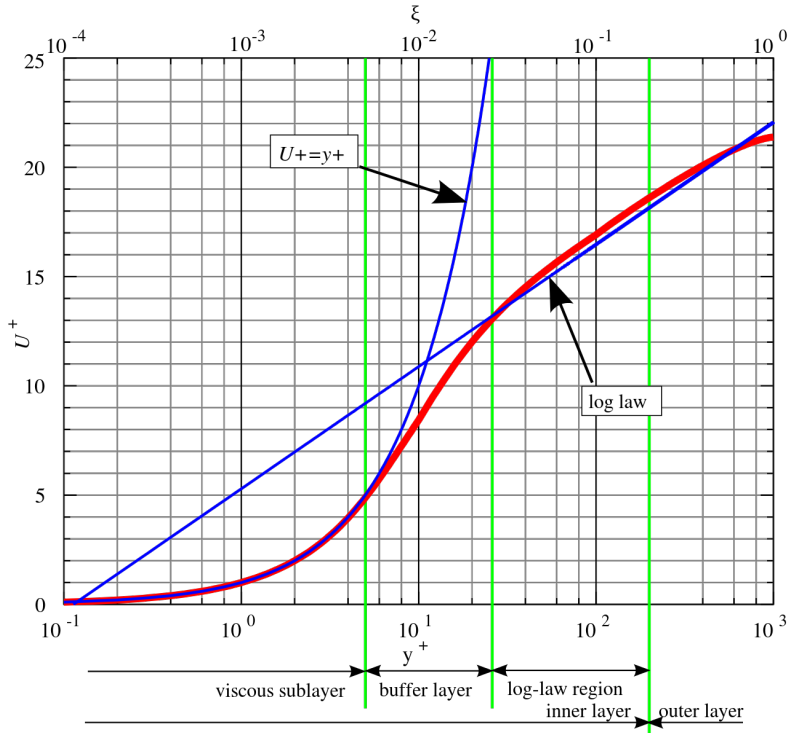


Figure 2.2: Behavior of flow near the wall (red line), together with two empirical wall functions [19]

The figure shows that the velocity profile near the wall can be divided into different regions. The first region is the viscous sublayer. Here, the velocity gradient is almost linear, and the viscous effects dominate. The second layer is the buffer layer above the viscous layer, with a high velocity gradient and turbulent flow. The next layer is the log-law region, where the velocity profile behaves logarithmically with the distance to the wall, where the viscous effects can be negligible. The last layer is the outer layer, and here the turbulent effects dominate [12, p. 364-366].

Since traditional wall functions do not provide a relationship between the flow and the distance to the wall in the buffer layer, a Spalding wall function is introduced. This wall function is a blending function that blends different wall functions and makes a good fit in the buffer layer [18]. In the present study, the *nutUSpaldingWallFunction* is used by employing the relationship of u^+ and y^+ as [20].

$$y^+ = u^+ + \frac{1}{E} \left(e^{\kappa u^+} - 1 - \kappa u^+ - 0.5(\kappa u^+)^2 - \frac{1}{6}(\kappa u^+)^3 \right) \quad (2.13)$$

E is the wall roughness parameter, and κ is the von Kármán constant. y^+ is the estimated non-dimensional wall-normal height of the cell center in wall units, and u^+ is the velocity

near the wall in wall units. y^+ and u^+ is defined respectively in Equation 2.14 and 2.15 [18] [20].

$$y^+ = \frac{yu^*}{\nu} \quad (2.14)$$

$$u^+ = \frac{u}{u^*} \quad (2.15)$$

Here, y is the distance to the wall, and u^* is the friction velocity on the wall. u is the velocity parallel to the wall as a function of y [12, p. 339].

2.6 ROV Motion

In this work, a 6 DOF simulated model will be developed to simulate the movement of the ROV. The motivation behind developing this simulator code is to verify the numerical result and study if the chosen CFD methods could be sufficient to create a reliable and realistic ROV simulator. The simulator code will be compared to the recorded data of a real ROV and is built on the equations in the current section.

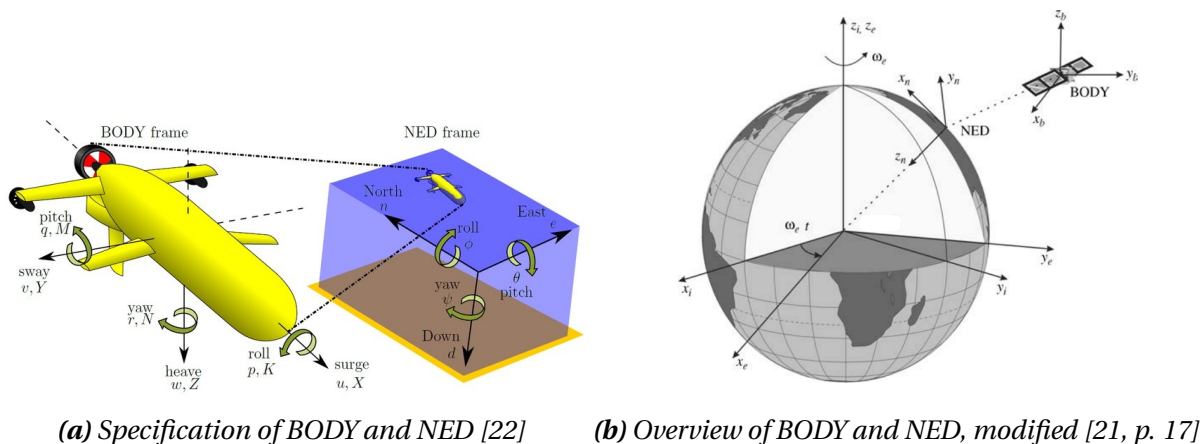
2.6.1 Reference Frames

Different notations will be used when defining the simulated 6 DOF model of the ROV. The notation for all 6 DOF is gathered in an overview and presented in Table 2.1.

Table 2.1: The different notations used for the DOF [21, p. 16]

DOF		Forces and moments	Linear and angular velocities	Positions and Euler angles
1	Motions in x-direction (surge)	X	u	x
2	Motions in y-direction (sway)	Y	v	y
3	Motions in z-direction (heave)	Z	w	z
4	Rotation about the x-axis (roll)	K	p	ϕ
5	Rotation about the y-axis (pitch)	M	q	θ
6	Rotation about the z-axis (yaw)	N	r	ψ

In this thesis, different reference systems are used. The first system is called the body-fixed reference frame, often called BODY. The other reference system is called NED, short for North East Down. Figure 2.3 visually explains the systems.



(a) Specification of BODY and NED [22]

(b) Overview of BODY and NED, modified [21, p. 17]

Figure 2.3: Definition of the BODY and NED reference system

The NED coordinate system $\{n\} = (x_n, y_n, z_n)$ with origin o_n is defined relative to the Earth's reference ellipsoid. The standard interpretation entails a tangent plane moving with the ROV on the Earth's surface. However, the axis point in the directions relative to the Earth's reference ellipsoid. By combining the figures in Figure 2.3, the x-axis points towards true north, the y-axis towards true east, and the z-axis points downwards, normal to the surface of the Earth [21, p. 17].

The BODY-fixed reference frame $\{b\} = (x_b, y_b, z_b)$ with origin o_b , and is fixed to the ROV. In this work, the position and orientation are relative to an inertial reference frame, the NED coordinate system. The linear and angular velocities are expressed in BODY [21, p. 17].

2.6.2 Kinematic

The 6 DOF kinematic equations are given in Equation 2.16.

$$\dot{\boldsymbol{\eta}} = J_{\Theta}(\boldsymbol{\eta})\mathbf{v} \quad (2.16)$$

Where $\dot{\boldsymbol{\eta}}$ is the velocities, and $\boldsymbol{\eta}$ is the position in all DOF for the ROV in NED. The last symbol in Equation 2.16 is \mathbf{v} , the velocities in all 6 DOF in the BODY reference frame [21, p. 194]. To be able to switch between the two reference frames, \mathbf{v} is multiplied with the transformation matrix $J_{\Theta}(\boldsymbol{\eta})$.

$$J_{\Theta}(\boldsymbol{\eta}) = \begin{bmatrix} \mathbf{R}_b^n(\boldsymbol{\Theta}_{nb}) & \mathbf{0}_{3 \times 3} \\ \mathbf{0}_{3 \times 3} & \mathbf{T}_{\Theta}(\boldsymbol{\Theta}_{nb}) \end{bmatrix} \quad (2.17)$$

This transformation matrix consists of four 3×3 matrices, where two of them are zero matrices [21, p. 26]. The Euler angle rotation matrix is expressed as $\mathbf{R}_b^n(\boldsymbol{\Theta}_{nb})$ and is shown in Equation 2.18. This matrix transforms the translational directions surge, sway and heave [21, p. 22].

$$\mathbf{R}_b^n(\boldsymbol{\Theta}_{nb}) = \begin{bmatrix} \cos(\psi) \cos(\theta) & -\sin(\psi) \cos(\phi) + \cos(\psi) \sin(\theta) \sin(\phi) & \sin(\psi) \sin(\phi) + \cos(\psi) \cos(\phi) \sin(\theta) \\ \sin(\psi) \cos(\theta) & \cos(\psi) \cos(\phi) + \sin(\psi) \sin(\theta) \sin(\phi) & -\cos(\psi) \sin(\phi) + \sin(\theta) \sin(\psi) \cos(\phi) \\ -\sin(\theta) & \cos(\theta) \sin(\phi) & \cos(\theta) \cos(\phi) \end{bmatrix} \quad (2.18)$$

The angular velocity transformation matrix is written as $T_{\Theta}(\Theta_{nb})$ and is presented in Equation 2.19. This matrix transforms the rotational directions of roll, pitch, and yaw [21, p. 25]. The resulting transformation matrix enables the conversion from BODY to NED of all DOF. The Euler angles expressed in this vector are presented in Table 2.1

$$T_{\Theta}(\Theta_{nb}) = \begin{bmatrix} 1 & \sin(\phi) \tan(\theta) & \cos(\phi) \tan(\theta) \\ 0 & \cos(\phi) & -\sin(\phi) \\ 0 & \frac{\sin(\phi)}{\cos(\theta)} & \frac{\cos(\phi)}{\cos(\theta)} \end{bmatrix} \quad (2.19)$$

2.6.3 6 DOF Equations of Motion

The foundation of the simulator code developed in the present study is the 6 DOF equations of motion represented by Equation 2.20. This equation can be used to simulate the motions of the ROV in all DOF [21, p. 194].

$$M\dot{\mathbf{v}} + C(\mathbf{v})\mathbf{v} + D(\mathbf{v})\mathbf{v} + \mathbf{g}(\boldsymbol{\eta}) = \boldsymbol{\tau} \quad (2.20)$$

Here, $\dot{\mathbf{v}}$ contains the accelerations, and \mathbf{v} contains the velocities of the vehicle in BODY. M is the system inertia matrix and consists of the mass of the ROV and the added mass [21, p. 194]:

$$M = M_{RB} + M_A \quad (2.21)$$

In Equation 2.21, M_{RB} is the rigid-body inertia matrix and M_A is the added mass matrix. Assuming that the ROV possesses three planes of symmetry and the ROV will be restricted to low-speed movement, it implies that the contribution from the off-diagonal elements in M_A can be neglected [21, p. 121].

$$\mathbf{M} = \begin{bmatrix} m + X_{\dot{u}} & 0 & 0 & 0 & 0 & 0 \\ 0 & m + Y_{\dot{v}} & 0 & 0 & 0 & 0 \\ 0 & 0 & m + Z_{\dot{w}} & 0 & 0 & 0 \\ 0 & 0 & 0 & I_x + K_{\dot{p}} & 0 & 0 \\ 0 & 0 & 0 & 0 & I_y + M_{\dot{q}} & 0 \\ 0 & 0 & 0 & 0 & 0 & I_z + N_{\dot{r}} \end{bmatrix} \quad (2.22)$$

Here, m is the mass of the ROV, and I_x , I_y , and I_z is the angular mass respectively about x-, y-, and z-axis. The added mass in the translational directions $X_{\dot{u}}$, $Y_{\dot{v}}$, and $Z_{\dot{w}}$ is the added mass in respectively surge, sway and heave as a result of acceleration in each own direction. The added inertia in the rotational directions $K_{\dot{p}}$, $M_{\dot{q}}$, and $N_{\dot{r}}$ is the added inertia in roll, pitch, and yaw as a result of angular acceleration in each own direction.

At low operational velocity, the Coriolis/centripetal force has a low contribution to the result. This ROV typically operates under 2 m/s and is considered a low-speed vehicle. Therefore, $\mathbf{C}(\mathbf{v})\mathbf{v}$ can be neglected. The same simplification also implies that the damping should be linearized at low velocity, but this is not considered [3] [21, p. 174-175]. For vehicles performing a noncoupled motion, the damping matrix $\mathbf{D}(\mathbf{v})$ can be written as [3] [21, p. 194]:

$$\mathbf{D}(\mathbf{v}) = \begin{bmatrix} X_u + X_{u|u}|u| & 0 & 0 & 0 & 0 & 0 \\ 0 & Y_v + Y_{v|v}|v| & 0 & 0 & 0 & 0 \\ 0 & 0 & Z_w + Z_{w|w}|w| & 0 & 0 & 0 \\ 0 & 0 & 0 & K_p + K_{p|p}|p| & 0 & 0 \\ 0 & 0 & 0 & 0 & M_q + M_{q|q}|q| & 0 \\ 0 & 0 & 0 & 0 & 0 & N_r + N_{r|r}|r| \end{bmatrix} \quad (2.23)$$

The linear damping in surge, sway, and heave due to constant flow in the same direction is represented by X_u , Y_v , and Z_w . Quadratic damping is indicated by $X_{u|u}$, $Y_{v|v}$, and $Z_{w|w}$, as a result of flow in the same direction. For the rotational direction roll, pitch, and yaw, the linear damping is symbolized as K_p , M_q , and N_r , and the quadratic damping as $K_{p|p}$, $M_{q|q}$ and $N_{r|r}$. These dampings are a result of constant angular velocity in each own direction. All the quadratic dampings are multiplied by a velocity or an angular velocity and are expressed in Table 2.1.

When performing sea trials, the ocean current enters the equations of motion. The velocity logged from the ROV is relative to the seabed. Therefore, the current is an essential source of

error and can make the ROV drift in directions that are not intended. This work assumes that the ocean current is constant and only influences surge and sway. The ocean current velocity, \mathbf{v}_c , is defined as:

$$\mathbf{v}_c = [u_c \quad v_c \quad 0 \quad 0 \quad 0 \quad 0]^T \quad (2.24)$$

The u_c and the v_c are the current velocities in the surge and sway direction. When considering the ocean current, the relative velocity between the seabed and the current, \mathbf{v}_r , must be calculated and is expressed as [3] [21, p. 43]:

$$\mathbf{v}_r = \mathbf{v} - \mathbf{v}_c \quad (2.25)$$

In this work, the current measured is in NED. Furthermore, the current velocity must be transferred to the BODY reference frame. The inverse velocity transformation is defined as:

$$\mathbf{v}_{b/n}^b = \mathbf{R}_b^n(\Theta_{nb})^{-1} \dot{\mathbf{p}}_{b/n}^n \quad (2.26)$$

In this case, $\mathbf{v}_{b/n}^b$ is the current velocity in BODY and $\dot{\mathbf{p}}_{b/n}^n$ is the measured current velocity in NED [21, p. 37].

For underwater vehicles, the gravity and buoyancy forces and moments are expressed as $\mathbf{g}(\boldsymbol{\eta})$ under:

$$\mathbf{g}(\boldsymbol{\eta}) = \begin{bmatrix} (W - B) \sin(\theta) \\ -(W - B) \cos(\theta) \sin(\phi) \\ -(W - B) \cos(\theta) \cos(\phi) \\ y_b B \cos(\theta) \cos(\phi) - z_b B \cos(\theta) \sin(\phi) \\ -z_b B \sin(\theta) - x_b B \cos(\theta) \cos(\phi) \\ x_b B \cos(\theta) \sin(\phi) + y_b B \sin(\theta) \end{bmatrix} \quad (2.27)$$

W is the gravity force, and B is the buoyancy force acting on the ROV. The distance along each axis from the Center of Origin (CO) to the Center of Buoyancy (CB) is marked as x_b , y_b , and z_b [21, p. 180]. The Euler angles expressed in this vector are presented in Table 2.1.

The last part of the 6 DOF equations of motion is $\boldsymbol{\tau}$, the generalized force. This force is found

with Equation 2.28.

$$\boldsymbol{\tau} = \boldsymbol{\tau}_{thrust} + \boldsymbol{\tau}_{external} = \mathbf{T}\mathbf{F} \quad (2.28)$$

Here, $\boldsymbol{\tau}_{thrust}$ is the thrust force, and $\boldsymbol{\tau}_{external}$ is the present external forces. The specific external forces in this study remain unknown. However, potential factors could be drag caused by the tether, collisions, or the utilization of manipulators. \mathbf{T} is the thruster configuration matrix and is presented in Equation 2.29. This matrix depends on the number of thrusters and the placement [21, p. 398-415]. The matrix found in this work only applies to the present ROV.

$$\mathbf{T} = \begin{bmatrix} \mathbf{k} \\ \mathbf{r} \times \mathbf{k} \end{bmatrix} = \begin{bmatrix} k_x \\ k_y \\ k_z \\ k_z l_y - k_y l_z \\ k_x l_z - k_z l_x \\ k_y l_x - k_x l_y \end{bmatrix} \quad (2.29)$$

Here, $\mathbf{k} = [k_x, k_y, k_z]^T$ and $\mathbf{r} = [l_x, l_y, l_z]^T$, which is respectively the decomposed direction and the moment arms in all the translational directions [21, p. 398-415]. The matrix of the decomposed direction is found in Equation 2.30.

$$\mathbf{k} = \begin{bmatrix} 0 & 0 & \sin(\alpha_v) & \cos(\alpha_h) & \cos(\alpha_h) & \cos(\alpha_h) & \cos(\alpha_h) \\ -\sin(\alpha_v) & \sin(\alpha_v) & 0 & \sin(\alpha_h) & -\sin(\alpha_h) & -\sin(\alpha_h) & \sin(\alpha_h) \\ \cos(\alpha_v) & \cos(\alpha_v) & \cos(\alpha_v) & 0 & 0 & 0 & 0 \end{bmatrix} \quad (2.30)$$

Here, $\alpha_v = 17.5^\circ$, and is the angle of the vertical thrusters. The angle of the horizontal thrusters is symbolized as $\alpha_h = 45^\circ$. The moment arms \mathbf{r} is a matrix with the same size as \mathbf{k} , but here the rows are the distance from CO to each thruster, respectively in x-, y- and z-direction in the BODY frame [21, p. 398-415]. The decomposed direction, the moment arms, and angles are extracted from the 3D model received from IKM Subsea [1].

The last variable is \mathbf{F} and is the thrust force from each thruster as a function of frequency. The magnitude of the frequency applied controls the thrusters, and the higher the frequency, the more force from the thruster. There is no analytical method to find this function, but one

method is to perform a pull test of the thruster alone or with the ROV [21, p. 398-415].

IKM Subsea has performed two pull tests in the past. One pull test with a single thruster and one with the UCV alone. Ideally, the pull test performed with the ROV would be used alone. However, it is decided to combine both pull tests due to the need for measures on several frequencies for the ROV [1].

This work uses two methods to convert the RPM to thrust by creating a conversion function. Equation 2.31 describes the relationship between the rotor's frequency and thrust force. This equation has a steady-state description and is presented in [23].

$$F(\Omega) = c\Omega|\Omega| \quad (2.31)$$

F is the thrust force, Ω is the frequency, and c is a proportionality constant. The problem with this function is that it often gives too high thrust force at a low frequency. A solution to this problem is to set a dead zone around $\Omega = 0$, and the explanation is presented in Equation 2.32 [24].

$$F(\Omega) = \begin{cases} C_1 (\Omega|\Omega| - \delta_1), & \text{if } \Omega|\Omega| < \delta_1 \\ C_2 (\Omega|\Omega| - \delta_2), & \text{if } \Omega|\Omega| > \delta_2 \\ 0, & \text{otherwise} \end{cases} \quad (2.32)$$

The unknown values c , C_1 , C_2 , δ_1 , and δ_2 depend on the thruster's characteristics and must be determined experimentally. Equation 2.31 or 2.32 is fitted together with the experimentally measured values, and the thrust conversion function is found [21, p. 398-415].

2.7 Calculations of Hydrodynamic Parameters

Different CFD simulations must be carried out to obtain the different hydrodynamic parameters. The damping is obtained by carrying out simulations under constant velocities, while the added mass and inertia is obtained by simulating oscillatory movement.

2.7.1 Hydrodynamic Damping

Hydrodynamic damping is defined as a reduction of the amplitude of a fluctuation and the reduction results from energy being emptied from the system. In this case, the fluid works as a break [25]. If the ROV is moving under a given velocity by using the thrusters and then shuts them off, the ROV will stop after a while due to hydrodynamic damping. The damping is divided into linear and quadratic terms. Linear damping is due to potential damping and possible skin friction, and quadratic damping is due to higher-order dampings, such as vortex shedding [21, p. 122-123].

To determine the damping in the translational directions, a constant inlet flow is applied in surge, sway, and heave using CFD. Furthermore, assumptions must be made by using the equations of motion. Since the flow is constant, there is no acceleration. In addition, the Coriolis force is neglected alongside the gravitational and buoyancy forces. According to these assumptions, the equations of motion considering a constant flow in surge can be simplified into the following [7] [9]:

$$D(\mathbf{v})\mathbf{v} = \boldsymbol{\tau} \quad (2.33)$$

For simplicity, each direction is considered independently to obtain the damping in the corresponding direction. Moreover, it is possible to simplify the equation of motion to calculate the total force in surge caused by an inlet flow in the same direction:

$$F_x(u) = X_u u + X_{u|u}|u|^2 \quad (2.34)$$

Here, F_x is the total force in the x-direction due to the constant inlet flow. X_u and $X_{u|u}|$ are the linear and quadratic damping due to the constant flow in the x-direction. The inlet flow velocity in surge is symbolized as u . When interpreting this equation, the force in the surge

direction is a function of the flow velocity in the same direction. Therefore, the procedure to find the damping is to conduct simulations under different inlet velocities and then find the linear and quadratic coefficients of the function. A similar method is used to obtain the damping in sway and heave under different inlet flow directions [7] [9].

The ROV is rotated with a constant speed to find the rotational damping. The simplifications employed in the translational directions are also applied in the rotational directions. This method resembles the approach for calculating the damping in the translational directions. However, the angular velocity and the moment about the corresponding axis are considered. The simplified equation of motion to calculate the moment in roll as a function of a constant rotation in roll is presented as:

$$M_k(p) = K_p p + K_{p|p|} p^2 \quad (2.35)$$

Here, $M_k(p)$ is the rotational moment around the x-axis as a function of the rotational velocity around the same axis. The linear and quadratic damping in roll is symbolized as K_p and $K_{p|p|}$, and p is the rotational velocity. Different angular velocities are simulated, and the linear and quadratic coefficients of the function are obtained. The same method is applied for pitch and yaw [9].

2.7.2 Hydrodynamic Added Mass and Inertia

The matrix presented in Equation 2.22 consists of the mass, inertia, and added mass and inertia. The mass and inertia are known, but the added mass and inertia can also be obtained using CFD. Added mass is an extra mass of the surrounding flow the body must move when accelerating in the fluid, and the added mass is a weighted integration of this entire mass. The increasing added mass will decrease the acceleration of the ROV [26].

To obtain the added mass and inertia in all 6 DOF, an unsteady PMM test is simulated. A forced oscillatory motion is prescribed for surge, sway, and heave with a linear oscillatory displacement. In Equation 2.36, a pure oscillatory surge motion is expressed as

$$\begin{cases} x = x_0 \sin(\omega t) \\ u = \dot{x} = x_0 \omega \cos(\omega t) \\ \dot{u} = \ddot{x} = -x_0 \omega^2 \sin(\omega t) \end{cases} \quad (2.36)$$

where x , u , and \dot{u} represent the displacement, velocity, and acceleration in surge. The amplitude of the movement is written as x_0 , and the angular frequency is $\omega = \frac{2\pi}{T}$, where T is the period, and t is the time. [8].

A constant inlet flow is required to achieve a pure sway and heave motion [8] [27]. Therefore, a constant inlet flow in surge, U_0 , is implemented in the simulations. The forced oscillating displacement in sway is presented in Equation 2.37, where y , v , and \dot{v} are the displacement, velocity, and acceleration in sway.

$$\begin{cases} y = y_0 \sin(\omega t) \\ v = \dot{y} = y_0 \omega \cos(\omega t) \\ \dot{v} = \ddot{y} = -y_0 \omega^2 \sin(\omega t) \\ u = U_0 \end{cases} \quad (2.37)$$

The oscillatory translational motions of the ROV result in oscillatory hydrodynamic forces. By simplifying the equations of motion and combining it with Equation 2.36, the total force in surge, F_x , can be expressed as [8] [27]:

$$\begin{aligned} F_x &= (m + X_{\dot{u}})\dot{u} + X_u u \\ &= X_{in} \sin(\omega t) + X_{out} \cos(\omega t) \end{aligned} \quad (2.38)$$

m is the mass of the ROV, and $X_{\dot{u}}$ is the hydrodynamic added mass in surge. The total hydrodynamic damping in surge is symbolized as X_u . Furthermore, X_{in} and X_{out} are the in-phase and out-phase components of the oscillating hydrodynamic force. These coefficients are found by using the fit function in MATLAB. The same method is used to obtain the added mass in sway and heave, but Equation 2.37 and 2.38 are specified for their corresponding directions.

The added mass can be calculated when the in-phase and out-phase coefficients are established. By combining Equation 2.36 and 2.38, the added mass in surge can be expressed as:

$$X_{\dot{u}} = \frac{X_{in}}{x_0 \omega^2} - m \quad (2.39)$$

Since these calculations will be conducted on numerical simulations, there will be no moment and inertial forces. The mass is not considered because only the hydrodynamic forces are calculated [27]. By performing CFD, the hydrodynamic forces, such as F_x , are found by integrating the pressure and viscous forces over the body (Equation 2.4).

Minor method changes must be made to find the added inertia for the rotational directions. An angular oscillatory displacement is forced in roll, pitch, and yaw. In Equation 2.40, a pure roll motion is expressed [8].

$$\begin{cases} \phi = \phi_0 \sin(\omega t) \\ p = \dot{\phi} = \phi_0 \omega \cos(\omega t) \\ \dot{p} = \ddot{\phi} = -\phi_0 \omega^2 \sin(\omega t) \end{cases} \quad (2.40)$$

The difference from Equation 2.36 is that ϕ , p , and \dot{p} are the angular displacement, angular velocity, and angular acceleration of the forced oscillatory roll movement.

To achieve a pure pitch, it is necessary to have zero velocity and acceleration in the heave direction. Similarly, zero velocity and acceleration in the sway direction are required to achieve a pure yaw. These conditions are essential to achieve a tangential path. It is necessary to generate a coupled motion simulation to accomplish this [8] [27]. Because the ROV is a slow-moving vehicle and the rotational angle is assumed to be small, only the rotational motion is considered. Also, in other studies, the translational displacement is small in couple motions [28]. Therefore, neglecting the coupled motion for pitch and yaw motions is reasonable. Furthermore, a constant inlet flow in surge is implemented, similar to sway and heave. The pitch motion is defined in equation 2.41.

$$\begin{cases} \theta = \theta_0 \sin(\omega t) \\ q = \dot{\theta} = \theta_0 \omega \cos(\omega t) \\ \dot{q} = \ddot{\theta} = -\theta_0 \omega^2 \sin(\omega t) \\ u = U_0 \end{cases} \quad (2.41)$$

Here, θ , q , and \dot{q} are the angular displacement, angular velocity, and angular acceleration for the oscillatory pitch motion. The total moment in the corresponding axis must be studied to find the hydrodynamic added inertia. The total hydrodynamic moment in roll generated by a forced oscillatory rotational motion combined with Equation 2.40, can be expressed as [8] [27]:

$$\begin{aligned} M_k &= (I_x + K_{\dot{p}})\dot{p} + K_p p \\ &= K_{in} \sin(\omega t) + K_{out} \cos(\omega t) \end{aligned} \quad (2.42)$$

In this equation, M_k is the total moment about the x-axis, I_x is the inertia about the x-axis, $K_{\dot{p}}$ is the hydrodynamic added inertia in roll, and K_p is the total hydrodynamic damping in roll. The in-phase and out-phase coefficients are K_{in} and K_{out} . The MATLAB fit function is used to find these components. This method can be applied when calculating the applicable hydrodynamic parameters for pitch and yaw, but Equation 2.41 and 2.42 are specified for the corresponding direction.

In the end, Equation 2.41 and 2.42 can be combined, and the added inertia in roll can be calculated. Therefore, the equation to find the added inertia in roll can be simplified as the following:

$$K_{\dot{p}} = \frac{K_{in}}{\phi_0 \omega^2} - I_x \quad (2.43)$$

Like the linear directions, the oscillating angular displacement simulations do not numerically solve the moment and inertial forces. Instead, only the hydrodynamic forces are calculated. Therefore, the inertia is not considered [27].

2.8 Instrumentation

Validation of the numerical estimated parameters is a crucial objective of this work. In order to achieve this, motion data of the ROV must be logged. The motion data is captured using the SPRINT-Nav 500, presented below. This instrument conducts various measurements to determine the position and velocity of the ROV accurately. However, it is essential to note that sea currents in the North Sea can be a critical source of error. The current should be considered in the calculations to ensure accurate results. A current meter is mounted on the cage, and the current is captured in the NED coordinate system. The current meter is presented below.

2.8.1 SPRINT-Nav 500

The SPRINT system uses a DVL and an Inertial Navigation System (INS) to determine the positions and velocities of a subsea vehicle. The central part of the DVL is the ultrasonic transceiver. The main components of the INS are the accelerometer and the gyroscope. The SPRINT can use different methods to calculate the positions and velocities. One of the methods is to use a DVL to capture the relative velocities and positions. In this study, the DVL is used relative to the seabed. The ultrasonic transponders and transceivers transmit and receive the signal. The delay or change of the signal can be used to calculate the relative distance between the ROV and the seabed. Furthermore, the signal change can be used to calculate the relative position and velocity of the ROV [29]. In Figure 2.4, a picture of a general SPRINT is presented.



Figure 2.4: Picture of the a general SPRINT-Nav [30]

The SPRINT also consists of an accelerometer to calculate the velocity. The velocity is found by integrating the acceleration measured from the accelerometer. It can measure the linear acceleration of the ROV in the x -, y -, and z -directions. It is conducted by measuring the electrical signal generated when forces act on a proof mass in the accelerometer. This signal is proportional to acceleration [29].

Another important sensor is the gyroscope. It uses the Sagnac effect to measure the rotation and angular velocity of the ROV. A ring laser gyro consists of 3 or 4 mirrors, creating a cavity for laser beams to travel in opposite directions. As the cavity rotates, one beam travels further than the other. A semi-transparent mirror allows some laser light to escape and form a fringe pattern, which optical sensors use to count the number and direction of fringes passed [29].

The information from the INS and the DVL are fused using a Kalman filter. It uses a mathematical algorithm to estimate the position and orientation of the ROV based on measurements from the accelerometer, gyroscopes, DVL, and pressure sensor. In addition, measurements from acoustic transponders can be considered. The role of the filter is to estimate and compensate for errors from the INS. The proper functioning of all sensors is crucial when measuring the position and velocity of the ROV [29]. In Table 2.2, the accuracy of the performance of the SPRINT is presented. By studying the table, it is assumed that the SPRINT is well suited for the engineering purposes in this work.

Table 2.2: Performance and accuracy for the SPRINT-Nav 500 [30]

Typical survey, position	0.02 %
Distance from origin, position	0.07 %
INS heading	0.04 °
INS roll and pitch	0.01 °
Velocity range and RMS	Up to ± 11.2 m/s ± 0.4 % of measured value
Altitude min/max	0.4/175 m

2.8.2 Model 803 ROV Current Meter

The Valeport Model 803 2-axis ROV Electromagnetic Current Meter is a specialized instrument for measuring relative water velocity. The system consists of an electronics housing containing the system electronics and the electromagnetic sensors. It can be mounted on the ROV and TMS. In this work, it is mounted on the cage and can measure the current relative to the NED system. The Model 803 consists of 2 axis electromagnetic flow sensor, which uses the Faraday principle to measure the flow. The sensor consists of a coil that generates a magnetic field, and a signal is generated across two pairs of electrodes. The change of the induced electrode voltage is proportional to the current flow. The data is periodically updated to provide flow information along the x- and y-axis. The x-axis is the flow across the sensor, while the y-axis indicates flow into the vehicle/cage [31]. Figure 2.5 and Table 2.3 presents a visual representation and performance accuracy.

**Figure 2.5:** Picture of the current meter [32]**Table 2.3:** Performance and accuracy for the current meter [32]

Range	± 5 m/s
Accuracy	± 0.01 m/s + 1 % reading
Resolution	0.001m/s

Chapter 3

Methodology

Three experiments will be recreated numerically to obtain the hydrodynamic parameters. The following experiments are the towing tank test [7] [8], the rotating arm test [9] [33], and the PMM test [8] [27]. In this chapter, the numerical modeling for the different simulations will be presented. The numerical modeling includes the simplification of the 3D model, the computational domain, and the mesh.

In addition, the experimental and validation method will be demonstrated in this chapter. This section presents the background and the processes of the data logging of the operational ROV. Furthermore, the method of validation using a simulator code is explained. At last, the approach of adjusting the hydrodynamic added mass and damping is presented.

3.1 Numerical Modeling

CFD simulations are carried out to acquire the hydrodynamic quantities of damping and added mass. CFD simulations demand high computational power. Therefore, the simulations are run on the University of Stavanger (UiS) High Performance Computing (HPC) unit Gorina 11. This HPC unit has 34 different nodes where some have up to 64 Central Processing Units (CPU), which can all be used to perform parallel computing of the CFD simulations. The computational meshes are distributed among the different CPUs, and the job will be finished faster than on a single CPU.

An appropriate simplification of the complicated ROV should be conducted before the simulations. Then, the computational domain is defined, and the mesh is generated. A mesh convergence study is conducted on two different versions of the UCV to decide if the mesh and the computational domain are sufficient. Thereafter, the two versions are compared to determine which version should be employed to acquire the hydrodynamic parameters concerning the distinct DOF.

Towing tank simulations are conducted to obtain the hydrodynamic damping in the translational directions. The towing tank test involves towing an ROV in a long tank of water to measure the resistance. This test could be used to obtain the hydrodynamic damping in the translational directions and where the ROV is moving in a straight line along the x-, y-, and z-direction [7] [8]. The drag force as a function of velocity in surge, sway, and heave is calculated by simulating various velocities in each direction to determine the hydrodynamic damping. Equation 2.34 is customized to calculate the linear and quadratic damping in surge, sway, and heave.

Rotating arm tests are numerically recreated for roll, pitch, and yaw to find the damping in the rotational directions. The rotating arm test obtains hydrodynamic coefficients related to the angular velocity. Hence, the coefficient is related to a turning maneuver of the ROV. These types of tests cannot be performed in a standard towing tank. Usually, the ROV model is attached to a rotating arm that spins around a vertical axis in a large circular pool to produce an angular velocity, which is challenging to conduct [33]. The simulations conducted in this work use a method similar to the MRF method [9]. The whole domain rotates to implement a constant angular velocity. These simulations use the same principle as the towing tank test and rotating arm test, and a constant angular velocity in roll, pitch, and yaw is conducted. In

this context, the moment around the relevant axis determines the damping in the rotational directions. Equation 2.35 is customized to calculate the linear and quadratic damping in roll, pitch, and yaw.

An acceleration of the ROV must be created to obtain the added mass and inertia. A well-known experimental test to find the added mass and inertia of an underwater vehicle is the PMM test, where a forced oscillatory motion is prescribed for the ROV. Even though it can be performed in a towing tank, it is still expensive and time-consuming [8] [27] [33]. Therefore, the solution and method used in the present study are to numerically recreate a PMM test. The ROV is subjected to a sinusoidal forced oscillatory displacement to obtain the hydrodynamic added mass and inertia. This forced motion is implemented individually in all 6 DOF to find the corresponding added mass and inertia.

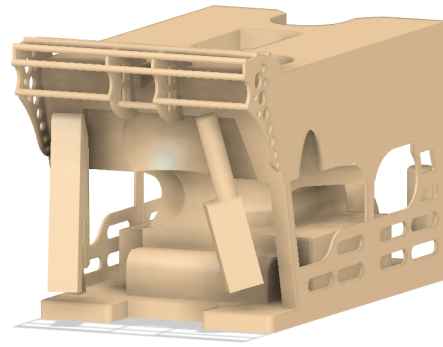
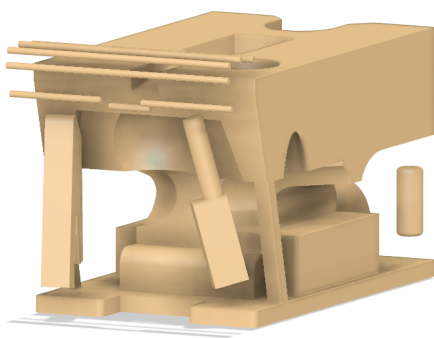
For surge, Equation 2.36 defines the oscillatory movement, and Equation 2.38 is the total force resulting from the movement. Curve fitting is used to obtain the unknown in-phase and out-phase parameters. Equation 2.39 is used to obtain the added mass in surge. A constant inlet flow is required to achieve a pure sway and heave motion [8] [27]. Therefore, Equation 2.37 defines the movement for sway. This equation is individualized to fit an oscillatory movement in heave. Equation 2.38 and 2.39 is customized for sway and heave to calculate the added mass. A similar method is used to find the added inertia in the rotational directions and is explained in Section 2.7.2.

3.1.1 3D Model

The Merlin UCV is investigated in the present study, and the 3D model is required from IKM Subsea [1]. This ROV is complex and has many different components and instruments, which makes the simulations difficult. More detailed mesh is required for a more complex 3D model, and the required computational power is increased with an increasing mesh number. Therefore, a simplification of the ROV is necessary. The idea is to delete or merge different parts as a more compact component. As a result, two simplified ROV versions are generated and presented in Figure 3.1.



(a) Detailed ROV model provided by IKM Subsea [1]



(b) Simplified version of detailed ROV, V1

(c) More detailed, but simple version of ROV, V2

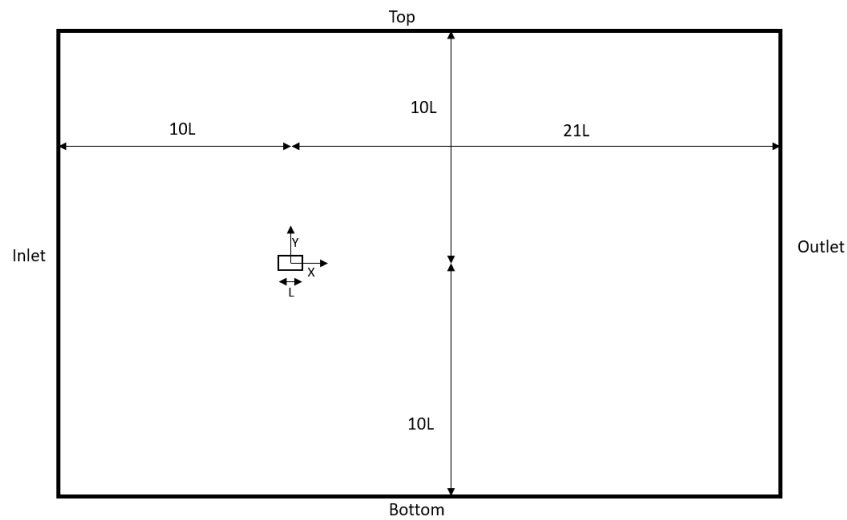
Figure 3.1: Difference between detailed ROV model and simplified versions

When performing the simplification, physical intuition and experience are essential. Therefore, two simplified models of the ROV are tested, one without side plates and one with side plates. Since the plates installed on the two sides may influence the hydrodynamic forces in sway, it is worth investigating the influence. They are presented respectively in Figure 3.1b and 3.1c, respectively called V1 and V2.

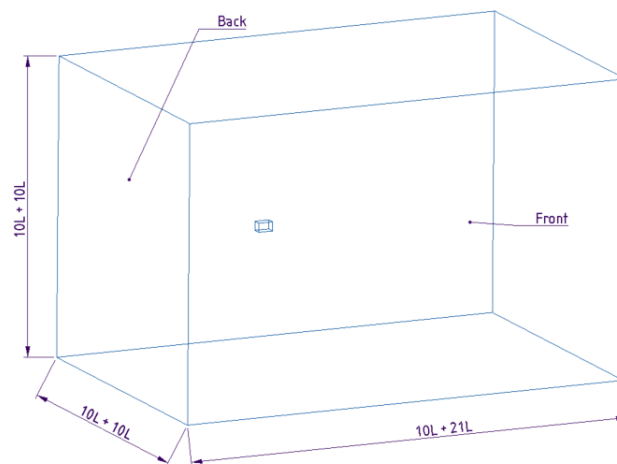
3.1.2 Computational Domain

The present study uses the same computational domain for the towing tank and PMM simulations. This computational domain is presented as a 2D view in Figure 3.2a and a 3D view in Figure 3.2b. To establish the numerical model, the center of the ROV serves as the point of origin. L represents the length of the ROV, while the inlet, top, bottom, front, and back are positioned at a distance of $10L$ from the ROV. The outlet is positioned $21L$ away from the ROV. The domain size in the present study is larger than the domain used in similar previous work

[8]. Therefore, the present domain is reasonable.



(a) View of the XY-plane, 2D domain



(b) 3D view of the domain

Figure 3.2: Domain used for towing tank and PMM simulations

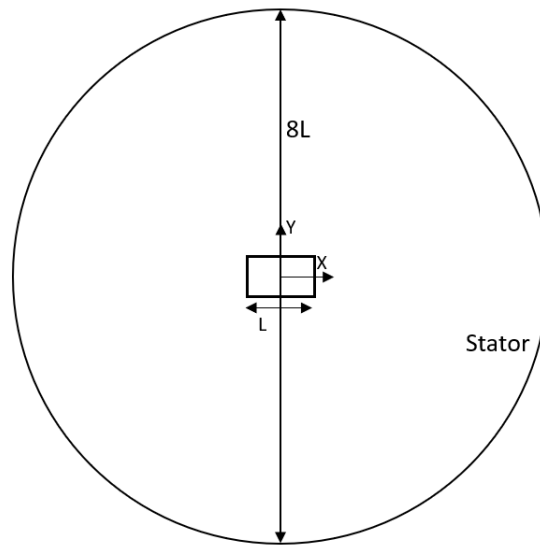
Towing tank simulations are conducted to find the damping in the translational directions, surge, sway, and heave. The ROV is flipped to study the different directions by changing the inlet, outlet, and boundaries. In this way, the direction of the towing of the ROV changes, and the rest computational domain is the same for all directions. A constant incoming flow is prescribed to simulate the towing in the translation directions to find the damping. The boundary conditions are therefore set as the following:

- At the inlet, the velocity is set to 0.25 m/s to 1.5 m/s with an increment of 0.25 m/s and the pressure to *zeroGradient*.
- At the outlet, the velocity is set to *inletOutlet* with the same velocity as the inlet, and pressure is set to *fixedValue* equal to zero.
- At the surface of the ROV, the velocity is set to *fixedValue* equal to zero and the pressure to *zeroGradient*. Wall functions based on the Spalding law resolve the boundary layer [18].

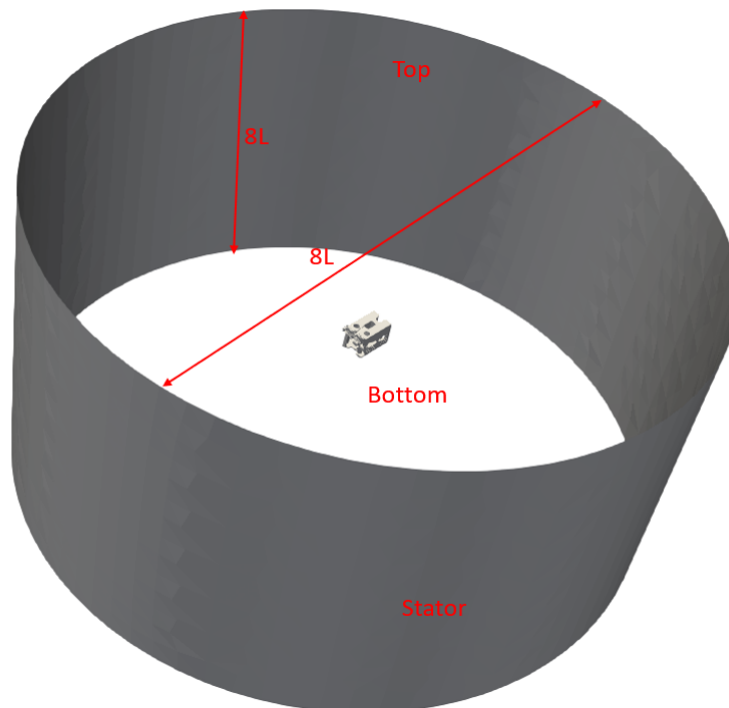
To calculate the added mass and inertia using CFD, an acceleration of the ROV is recreated through PMM simulations. A forced oscillating linear and angular displacement is implemented to reproduce the PMM test for all 6 DOF. All the simulations have an incoming flow to achieve a pure motion, except those in surge and roll [8] [27]. To simulate a linear oscillating movement, the *solidBodyMotionFunction*, *oscillatingLinearMotion* is utilized, and *oscillatingRotatingMotion*, is used to simulate the rotational motion. The *pointDisplacement* is introduced to determine the various types of oscillatory movements. It is defined based on whether the motion is linear or rotational and its direction. The amplitude is set respectively to 0.25 m and 15 ° for the linear and rotational motion. The frequency is defined between 1 Hz and 0.2 Hz. The boundary conditions for the oscillating displacement cases are set to the following:

- At the inlet, the velocity is set to zero for simulations in surge and roll. The inlet velocity is set to 0.25 m/s for the other DOF, equal to a reasonable operational velocity. The pressure is equal for all DOF and is set to *zeroGradient*.
- At the outlet, the velocity is set to *zeroGradient*, and pressure are set to *fixedValue* equal to zero.
- At the surface of the ROV, the velocity is set as *movingWallVelocity* equal to zero and the pressure to *zeroGradient*. Wall functions based on the Spalding law resolve the boundary layer [18].

Rotational arm simulations are carried out to find the damping in the rotational directions roll, pitch, and yaw. Figure 3.3 presents the circular domain used to simulate a rotating arm. The circular domain has a form of a stator with a diameter and height of 8L. The current domain has a larger boundary size than similar previous research [9], indicating that the domain used in this study is reasonable.



(a) View of the XY-plane, 2D domain



(b) 3D view of the domain

Figure 3.3: Domain used for the rotating arm simulations

The rotational arm simulations are similar to the towing tank simulations, but a constant angular velocity is applied. The ROV's position remains unchanged to transform between the rotational directions. The boundary is rotated to simulate rotational flow in roll, pitch, and yaw. In these simulations, the domain rotates to create a constant angular flow. The file *MRFProperties* is implemented in the constant folder to change the angular velocity. Here, the rotational velocity and axis can be defined, and the velocities are set from 0.1 rad/s to

0.4 rad/s with a 0.1 rad/s step. The boundary conditions for the rotating arm cases are set to the following:

- At the top and stator, the velocity and pressure are set to *zeroGradient*.
- At the bottom, the velocity is set to *zeroGradient* and the pressure to *fixedValue* equal to zero.
- At the ROV, the velocity is set to *noSlip*, and pressure is set to *zeroGradient*. Wall functions based on the Spalding law resolve the boundary layer [18].

3.1.3 Mesh

To discretize the computational domain to solve the governing equations numerically, an open-source library mesh generator, cfMesh, generates the mesh, implemented within the OpenFOAM framework. cfMesh allows for simple implementation of new meshing workflows and applications[34]. There have mainly been used two different functions within cfMesh to refine the mesh: *objectRefinements* and *boundaryLayers*. The first tool is used to refine volumetric regions within the mesh, and it is possible to use object refinement to specify a zone using coordinates. The function *box* is defined for the local refinement of the mesh, and it is possible to decide the size of the volume and the element size.

The other function used is boundary layer refinement. It is possible to use a setting inside this function called *patchBoundaryLayers*. This setting is a dictionary for specifying local properties of boundary layers for individual elements. This property of making inflation layers is helpful to control the y^+ value and refine the mesh inside the boundary layer [34]. Example meshes for the two different simplifications of the ROV (V1 and V2) are shown in Figure 3.4.

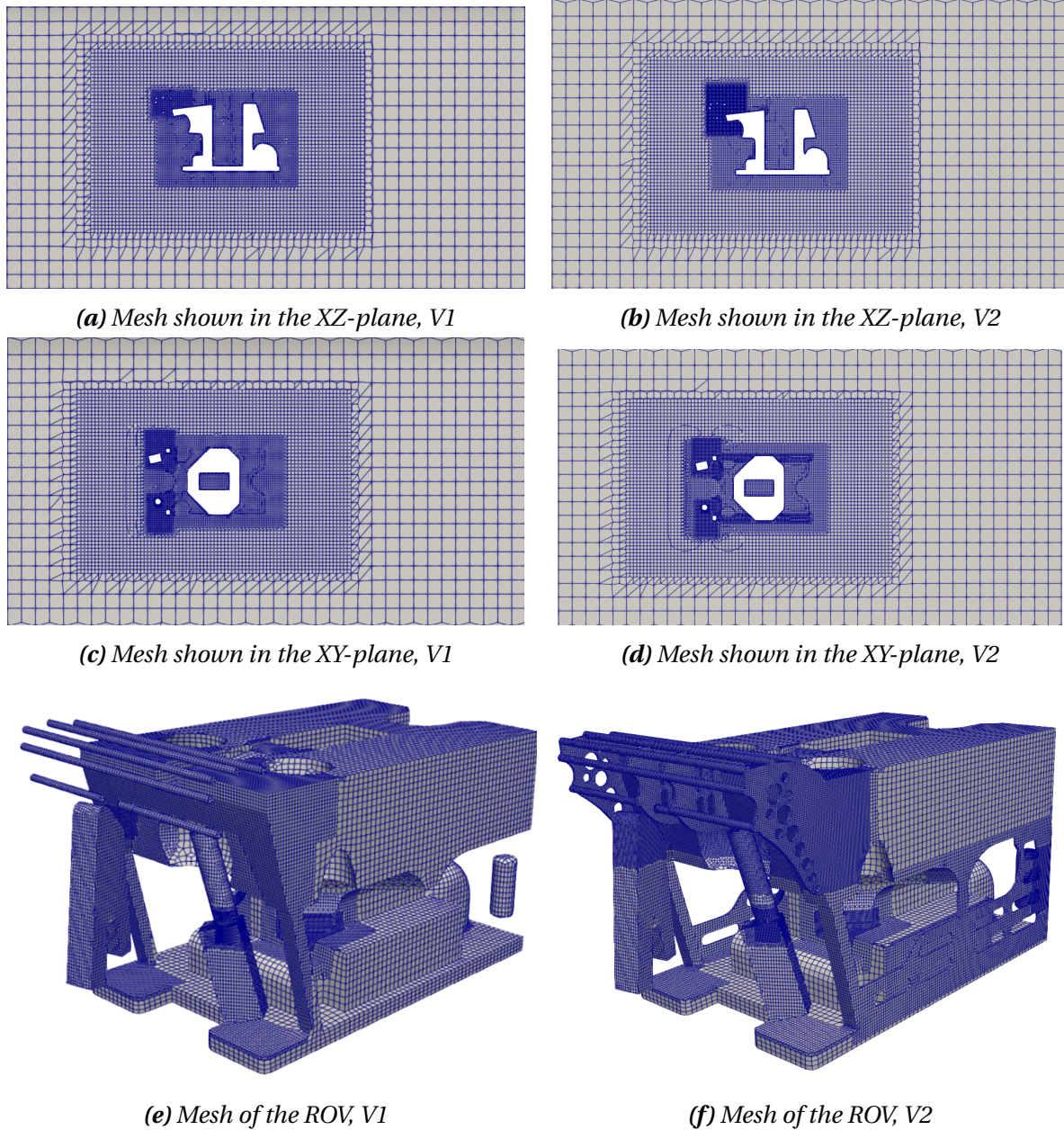


Figure 3.4: An example of the mesh for the two versions in the present study

The grid resolution and mesh topology for the circular domain is similar to the mesh presented in Figure 3.4. The refine function *box* is replaced with *cone* to capture the angular velocity better. This subdomain is intended for defining circular mesh and, therefore, more efficiently resolving a rotational flow [34]. The circular mesh in Figure 3.5 provides an example of angular flow in yaw. Here, the flow is rotating around the normal vector of the plane presented.

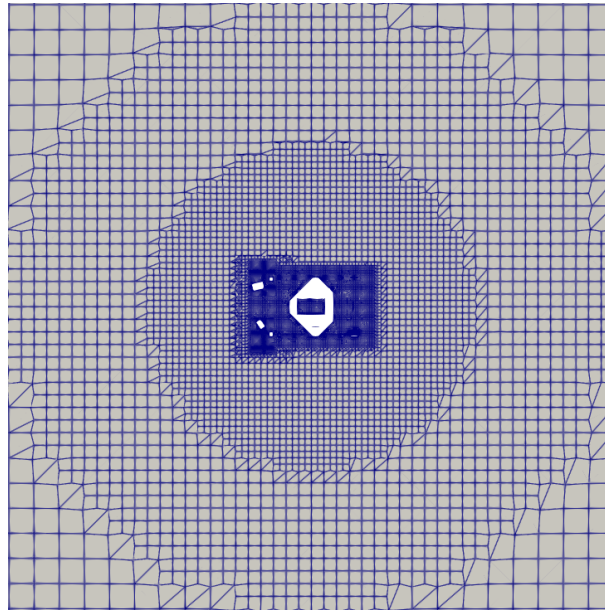
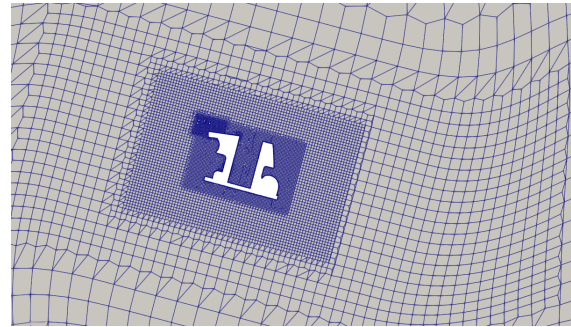
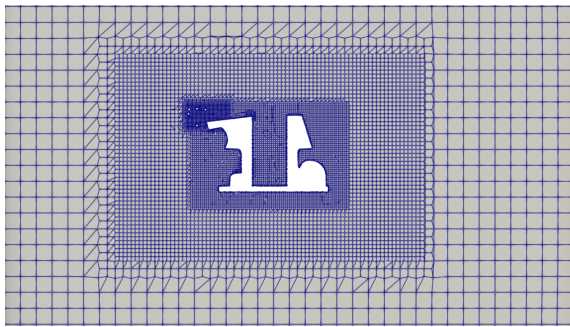
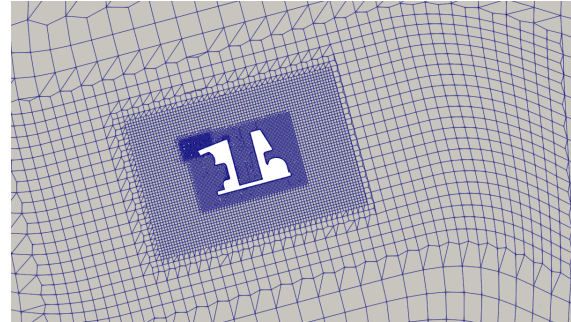
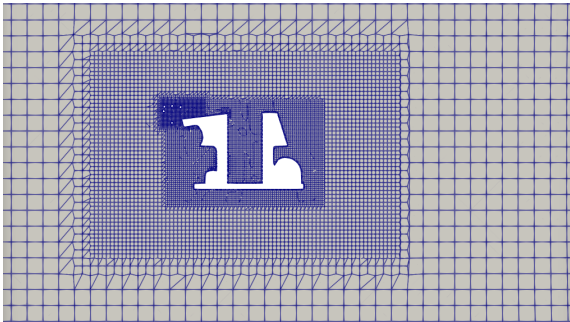


Figure 3.5: Circular mesh when the angular flow is in yaw

Different methods can make the ROV model oscillate in linear and rotating directions. This movement is carried out by implementing a *dynamicMeshDict* in the constant directory. It is possible to define the center of interest, the inner and outer regions using this dictionary, and the *solidBodyMotionFunction*. The center of rotation is defined as the center of the ROV, and the inner and outer region is defined as a circle with a distance as a radius from the center. The mesh can deform within the two regions. Figure 3.6 shows an example of the deformed mesh.



(a) Oscillating linear motion in surge, $t/T = 0.25$ (b) Oscillating rotation motion in pitch, $t/T = 0.25$



(c) Oscillating linear motion in surge, $t/T = 0.75$ (d) Oscillating rotation motion in pitch, $t/T = 0.75$

Figure 3.6: Dynamic oscillating mesh in the XZ-plane

In this figure, t is the time, and T is the period of oscillation. Figure 3.6 shows the amplitude in both directions of the movement, and all the sub-figures have the starting point of $t/T = 0$, shown in Figure 3.4a. As shown in Figure 3.6, the mesh around the ROV keeps the geometry and seems frozen, but the mesh is getting deformed between the inner and outer regions. This observation is more visible for the rotational motion than the linear motion. However, elements with high skewness near the wall are avoided.

3.2 Experimental Method and Validation

Since the hydrodynamic coefficients are found numerically, they must be validated. The ideal method for validation is an experimental test with the ROV in a controlled environment and being able to do measurements of the added mass and damping in all DOF directly. This method is expensive and time-consuming because testing a full-size working ROV requires a large lab. The queue is long, and the price is high to test in a large-scale lab. Stadt towing tank is a large-large scale lab where IKM Subsea has tested an ROV using a full-scale ROV model [1].

Another preferred validation method is a down-scaled model in a smaller, less expensive lab. An example of such a facility is MarinLab at Western Norway University of Applied Sciences (HVL) in Bergen. Due to the tight schedule at MarinLab, this project was not prioritized to perform experimental tests.

Therefore, sea tests at SNB are performed to validate the hydrodynamic coefficients. IKM Subsea has an Onshore Control Center (OCC) at Bryne, where they remotely control an ROV at SNB. An overview of the OCC is presented in Figure 3.7. It is possible to log live data from the ROV through the fiber connection [1]. The data logged is the time, position, and velocity in all DOF and thruster Rounds Per Minute (RPM). The motion data are measured through the SPRINT-Nav 500 [29]. The thruster RPM is logged using two different methods. The first method is to log the commanded input RPM, which is the RPM the thrusters are trying to reach. The second method is the measured RPM which uses a magnetic RPM sensor to count the number of rotations per minute [1].



Figure 3.7: Overview of the OCC [1]

As the environment at SNB cannot be regulated, there are several sources of error compared to a controlled laboratory environment. Therefore, implementing measures that minimize errors is essential. One of the most impotent sources of error is the sea current. The current could decompose the actual movement of the ROV and make it drift in an unknown direction. This error could result in the ROV advancing in a different direction than first intended. A solution to this problem could be to install a current meter on the ROV cage. The current meter will then be able to measure the current direction and velocity, and the influence of the current can be considered.

The equations of motion are introduced to recreate the movement of the ROV to validate the numerical estimated parameters. The idea is to make an ROV simulator code in MATLAB built on these equations to compare the recorded movement with the simulated movement. The simulator code will read the thruster RPM and convert the RPM into thrust force using a thrust conversion function. For the conversion to be accurate, it is important to correctly define the thrusters based on their angles and distance from the CO. The converted thrust force will propel the ROV in the same direction as the recorded data. The added mass and damping calculated using CFD are implemented in the equation and determine the magnitude of the movement. The movement of the ROV is numerically simulated using a Runge–Kutta method to solve the equations of motion. The experimental logged and simulated position and velocity should be around the same magnitude for the hydrodynamic parameters to be valid.

In this work, newly logged data will be gathered at SNB. For the sake of simplicity, four types of sea trials will be logged. The first three will contain a constant surge, sway, and heave velocity followed by a shutdown of the thrusters and waiting until the ROV stops. The thought is to individually verify the transitional added mass and damping by implementing an acceleration followed by the damping by the fluid. The last new dataset will consist of different movements in yaw. A constant speed in yaw cannot be achieved due to the twisting and tearing of the tether. Roll and pitch must be programmed to move more significantly in these directions. However, movement in roll and pitch is often a result of movement in the first four DOFs. Therefore, position and velocity in roll and pitch will be studied accordingly in the four datasets.

At last, when the simulator code is working with the simple movements, a dataset from 2021 will be used to study the whole movement and challenge the simulator code. Here, all six

degrees of freedom will be studied. The dataset consists of random movement, and if the calculations are correct, the simulator code should capture the whole movement.

Ultimately, the hydrodynamic parameters will be adjusted to optimize the accuracy of the simulated position and velocity. The procedure is close to "data assimilation" in which recorded or observation data is utilized to adjust the CFD estimated parameters used in the simulator. The objective is to achieve a good model of the simulator for the ROV. In this work, the goal of using this method is to assess its effectiveness and accuracy. Notably, the method is based on experience and intuition to achieve this optimization. The added mass and damping in each direction will be adjusted to achieve the best fit, and examples of the adjusted simulated position and velocity will be presented.

Chapter 4

Results and Discussion

Initially, two convergence studies for V1 and V2 are performed. Additionally, a comparison between the two versions of the ROV is carried out, and a decision is made on which version to use for each DOF. During towing tank simulations, the damping in surge, sway, and heave is investigated by conducting a constant inlet flow. The remaining damping in the rotational directions uses the same principle of constant velocity. However, an angular velocity is implemented by conducting rotational arm simulations. The last simulations are the PMM tests. The added mass and inertia in all DOF is obtained by implementing an oscillatory displacement.

Furthermore, the hydrodynamic added mass and damping are validated by comparing the numerical results through a simulator code with recorded data of an operational ROV. Then the hydrodynamic parameters are adjusted to assess if a better fit between the simulated and recorded data is achievable. All the results are discussed throughout the chapter, but the main discussion is presented at the end. Here, the main challenges with the work are discussed and tied together.

4.1 Mesh Convergence Study

Performing a mesh convergence study as a verification study is essential for CFD simulations. Typically, a finer mesh gives a more accurate result than a coarser mesh. However, a finer mesh requires more computational power, requiring long computational runtime. The objective of performing a convergence study is to find the balance between the number of used cells and the accuracy of the results. When this mesh has been found and verified, the selected mesh resolution can be used for further investigation.

In the present study, two simplified models represent the Merlin UCV, V1 and V2. Since there are two different versions, two different mesh convergence studies must be conducted. Both studies simulate a flow at the highest Reynolds number, with an inlet flow velocity of 1.5 m/s. The Reynolds number is 2.25×10^6 , and the flow can be regarded as fully developed turbulence. The first convergence study to be completed is for V1, and the results of the drag coefficient, C_d , are plotted in Figure 4.1. The value of C_d for different meshes is shown in Table 4.1 to evaluate the grid resolution. In this study, the incoming flows are in the surge direction.

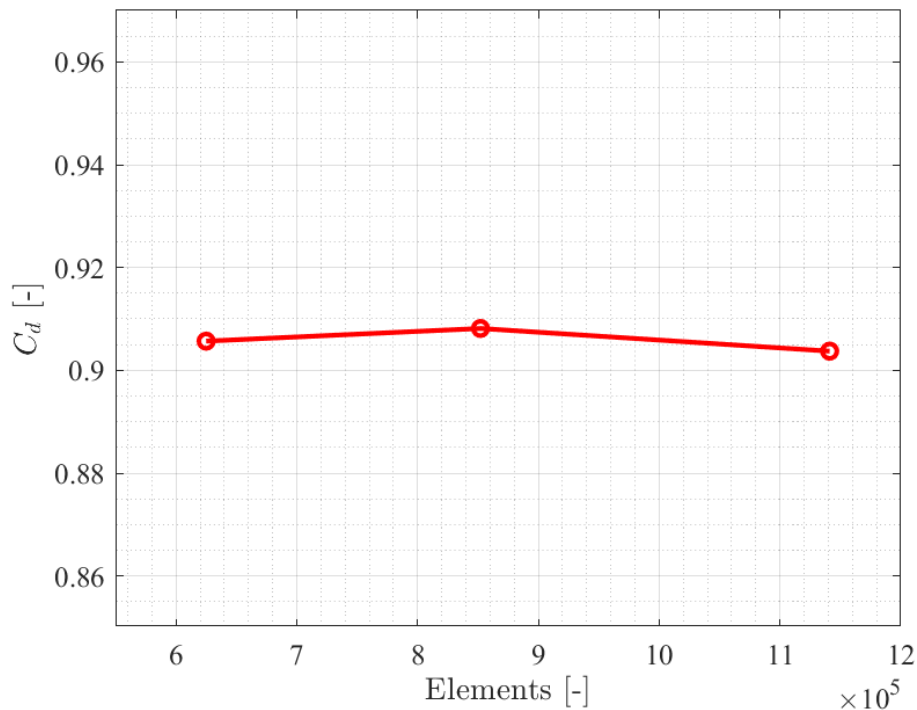


Figure 4.1: The results of C_d for different numbers of meshes with an incoming flow in the surge direction

Table 4.1: The results of y^+ for different number of meshes

	No. of cells	y^+	C_d	% difference
Case 1	624991	58	0.9057	0.22 %
Case 2	852085	59	0.9081	0.49 %
Case 3	1141128	60	0.9037	-

The relative difference between different cases is under 1 % and can be neglected. Therefore, to achieve the balance between the number of cells and the accuracy, the mesh resolution of Case 2 is chosen. This grid resolution is sufficient to resolve the flow near the wall and in the far field without any noticeable deformed elements. This mesh is used to perform all the simulations using V1 in the present study.

The objective of V2 is to further study the effect of the thin plates on the two sides of the ROV. From the basic physical understanding, it is obvious to assume that these plates will influence the drag in the sway direction. Therefore, the convergence study performed on V2 is under the flow in the sway direction. This version is also tested in surge and heave directions to examine if these plates influence the drag coefficient in these directions. The comparison between V1 and V2 is presented in the following section. The results for the mesh convergence study of V2 are presented in Figure 4.2 and Table 4.2.

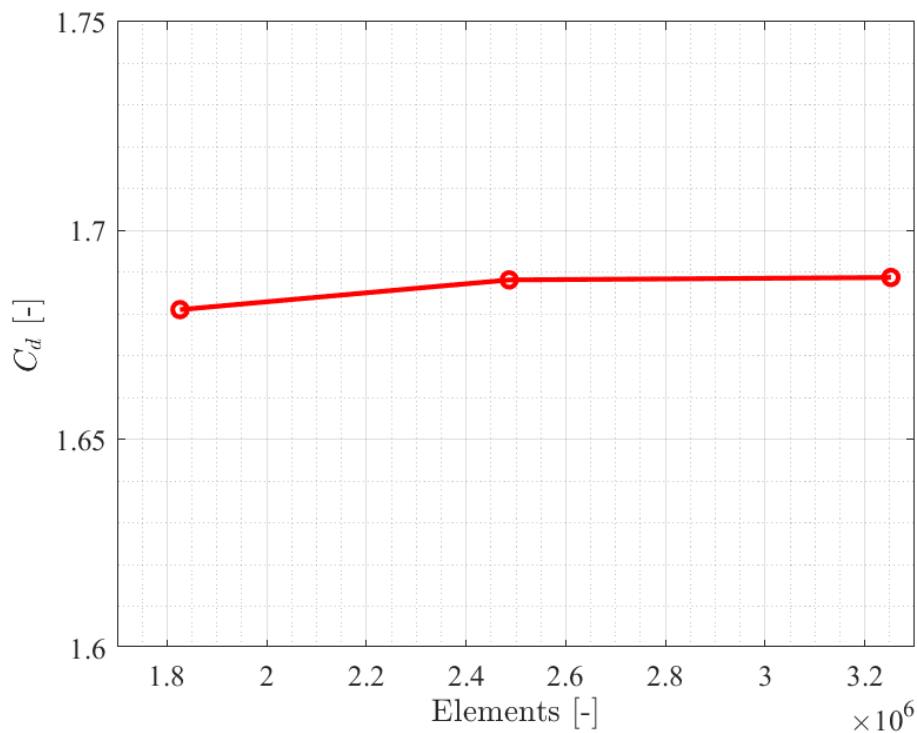
**Figure 4.2:** The results of C_d for different numbers of meshes with an incoming flow in the sway direction

Table 4.2: The results of y^+ for different number of meshes

	No. of cells	y^+	C_d	% difference
Case 1	1826021	59	1.6811	0.46 %
Case 2	2486536	43	1.6882	0.04 %
Case 3	3252411	43	1.6888	-

The relative difference is also under 1 % and can be neglected by interpreting the result in this convergence study. Case 2 is chosen to achieve the balance between the mesh number and the accuracy, and this mesh resolution is chosen for further investigation.

4.1.1 Comparison of the Hydrodynamic Forces of V1 and V2

The simulations for V2 are conducted to study the effect of the thin side plates. Although, based on physical intuitions, these plates may only influence the drag in the sway direction, this has to be examined carefully. Two simulations in both surge and sway are conducted for V1 and V2. Table 4.3 presents the drag coefficient and force for the surge and sway direction.

Table 4.3: Comparison of V1 and V2 by studying the drag coefficient and drag force

<i>(a) Flow in surge, comparing V1 and V2</i>				<i>(b) Flow in sway, comparing V1 and V2</i>			
	V1	V2	% difference		V1	V2	% difference
C_d	0.9081	0.9120	0.43 %	C_d	1.4682	1.6880	14.97 %
F_x	1021.6 N	1025.9 N	0.43 %	F_y	1651.7 N	1899.0 N	14.97 %

When comparing surge direction, the difference in drag is under 1 % and is negligible. However, there are differences in the sway direction. The thin plates are exposed to the flow, and the drag increases by 15 %.

Therefore, using basic fluid dynamics understanding, V1 is chosen when simulating flow or movement in surge, heave, and pitch direction since the thin plates are not directly exposed to the flow in these directions. V2 is used when investigating parameters for flow or movement in sway, roll, and yaw when the thin plates are directly exposed to the incoming flow.

When comparing the different versions of the ROV, the mesh is essential to consider. Due to the side plates, V2 requires more elements compared to V1. To preserve the details of the plates, the mesh number of V2 is almost three times as large as that used for V1. Therefore, V1 is preferable to V2, and the mesh of V1 should be used. However, there are still conditions where the mesh of V2 should be used, such as the flow in the sway direction.

4.2 Towing Tank Simulation

The hydrodynamic damping will be obtained in all three translational DOF by recreating a towing tank test numerically. These three directions are the most important because the ROV frequently moves in these directions. Nevertheless, the rotational directions should also be investigated. Incorrect damping values in the rotational directions can result in overestimated rotational motion amplitudes, which affects the translational movement. The following section will investigate the rotational damping by simulating a rotating arm test.

For the study of hydrodynamic damping in the translational directions, the velocity of the incoming flow is chosen to be in the range of 0.25 m/s to 1.5 m/s with an incremental of 0.25 m/s. Here, the goal is to find the force as a function of the flow velocity. Equation 2.34 is used to obtain the linear and quadratic damping in surge, sway, and heave.

4.2.1 Surge

The first investigated direction is the surge, in which the ROV moves in most circumstances. Six cases are simulated under different incoming flow velocities in the surge direction. Figure 4.5 shows the contours of U_x and the pressure distribution under the incoming flow velocity of 1 m/s.

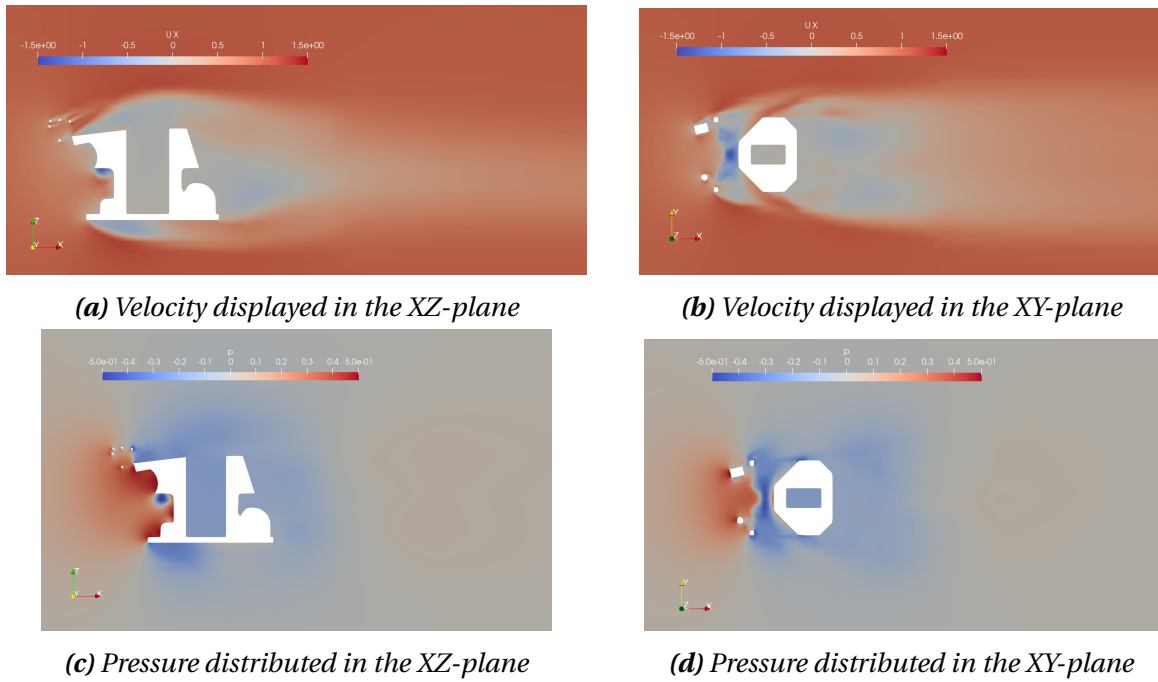


Figure 4.3: Contours of the stream-wise velocity and the pressure under the incoming flow velocity of 1 m/s

Here, the velocity contours and the formation of the wake are smooth. The pressure distribution is as expected, with the highest pressure in the front due to the incoming flow. The relationship between the incoming flow velocity and the drag force is presented in Figure 4.4. After six simulations with different flow velocities are completed, the linear and quadratic damping values can be calculated. Here, the linear rate of increase is the linear damping, and the quadratic rate of increase is the quadratic damping. The linear and quadratic damping values are obtained by curve fitting the simulation data using Equation 2.34.

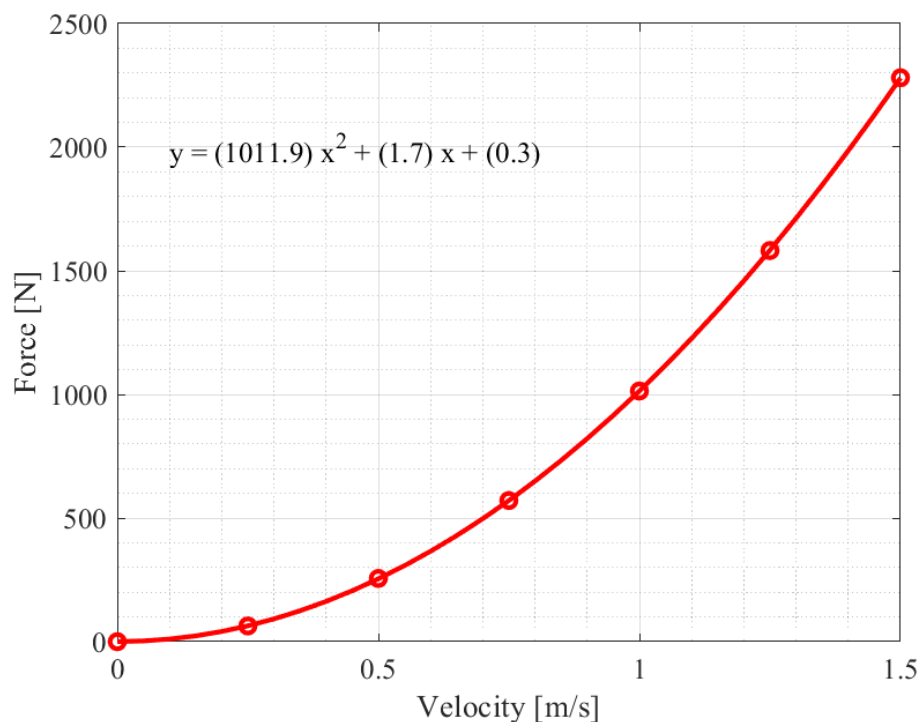


Figure 4.4: The linear and quadratic damping in surge found by using polyfit in MATLAB

The linear damping in the surge direction due to a constant velocity in this direction, X_u , is calculated to be 1.7 Ns/m, and the quadratic damping, $X_{u|u|}$, is 1011.9 Ns/m. The value of the linear damping is relatively negligible compared to quadratic damping. Therefore, the linear value can be neglected, which is reasonable based on literature [2] [7] [9] [35].

4.2.2 Sway

The hydrodynamic damping for sway is calculated using the same method presented in the section above. The contours of the velocity in the y-direction under the incoming flow velocity of 1 m/s are shown in Figure 4.5.

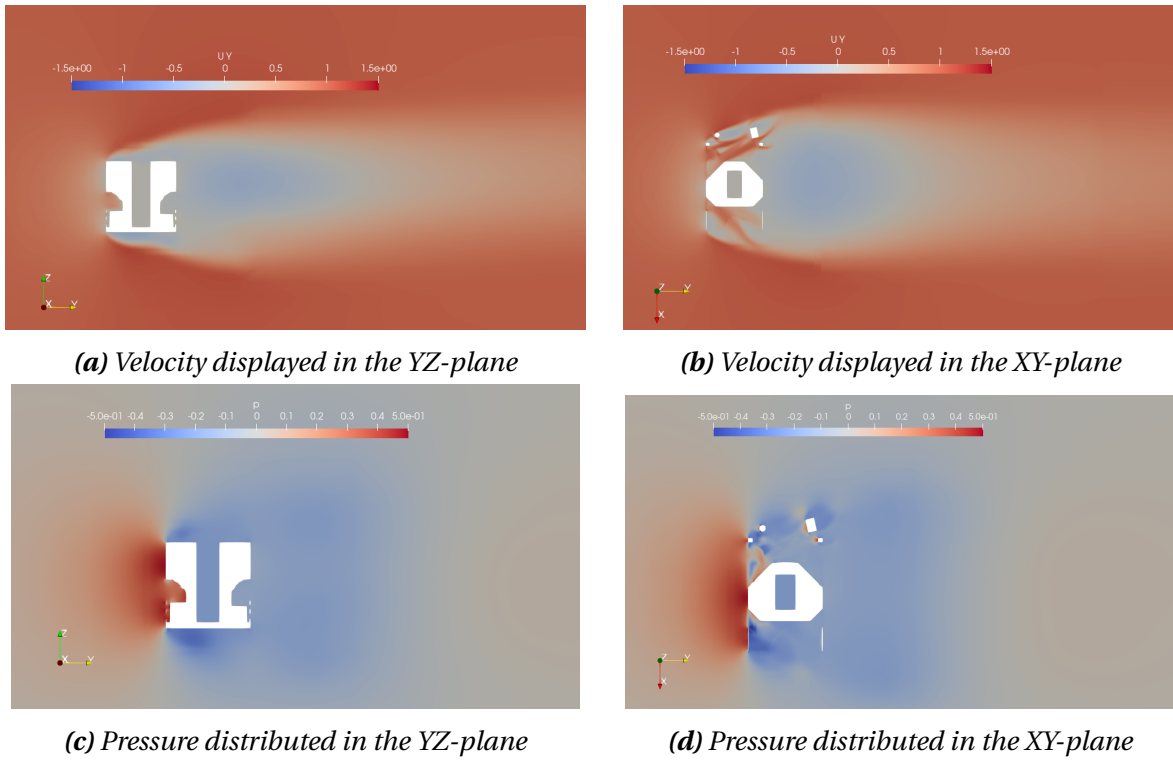


Figure 4.5: Contours of the stream-wise velocity and the distributed pressure under the incoming flow velocity of 1 m/s

In this Figure, the flow and pressure are smooth. The wake is pointing obliquely towards the z-direction due to the geometry of the ROV. After six simulations under six different velocities in the sway direction have been completed, the linear and quadratic damping can be obtained using curve fitting together with Equation 2.34. The equation is modified for a force in sway as a function of the flow velocity in the same direction. The plot for the relationship between the velocity of the incoming flow and force in the sway direction is presented in Figure 4.6.

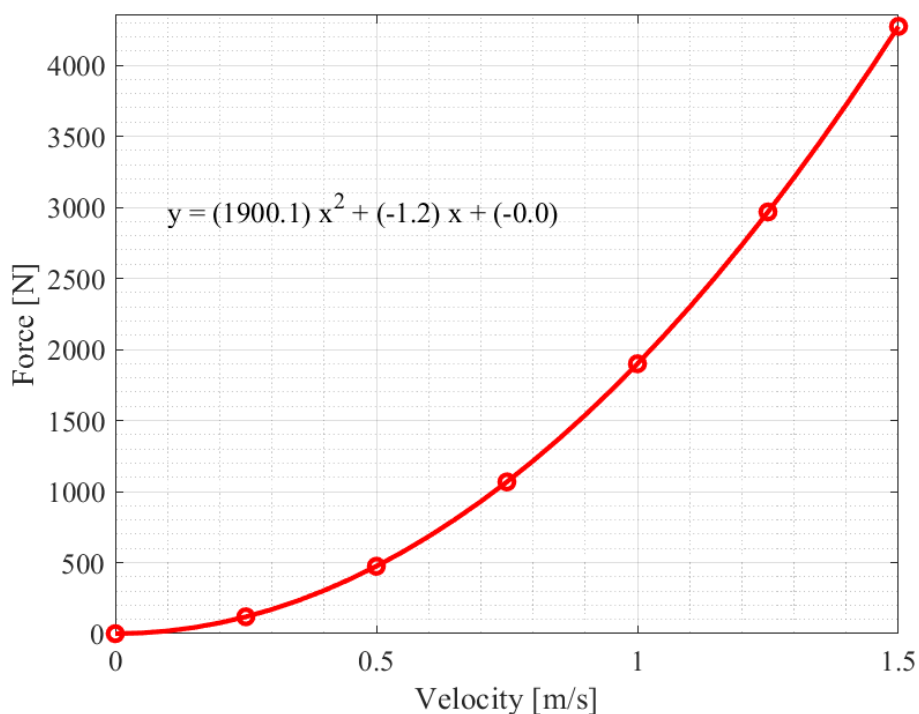


Figure 4.6: The linear and quadratic damping in sway found by using polyfit in MATLAB

As expected, the damping is more significant in sway compared to surge. The linear damping in sway direction due to a constant flow in this direction, Y_v , is -1.2 Ns/m, and the quadratic damping $Y_{v|v|}$, is 1900.1 Ns/m. Note that the linear damping is negative, which seems to be unreasonable. Nevertheless, the value of the linear damping is small compared with the quadratic damping, indicating that it can be neglected as the linear damping found in surge. In this case, the value of the quadratic damping is almost twice the value of surge since the cross-section area is bigger in sway than surge.

4.2.3 Heave

The last translational direction considered is heave. The same method used previously for surge and sway is adopted and individualized for heave. Figure 4.7 shows the contour plots of the flow velocity and the pressure distribution in the z-direction under the incoming flow of 1 m/s.

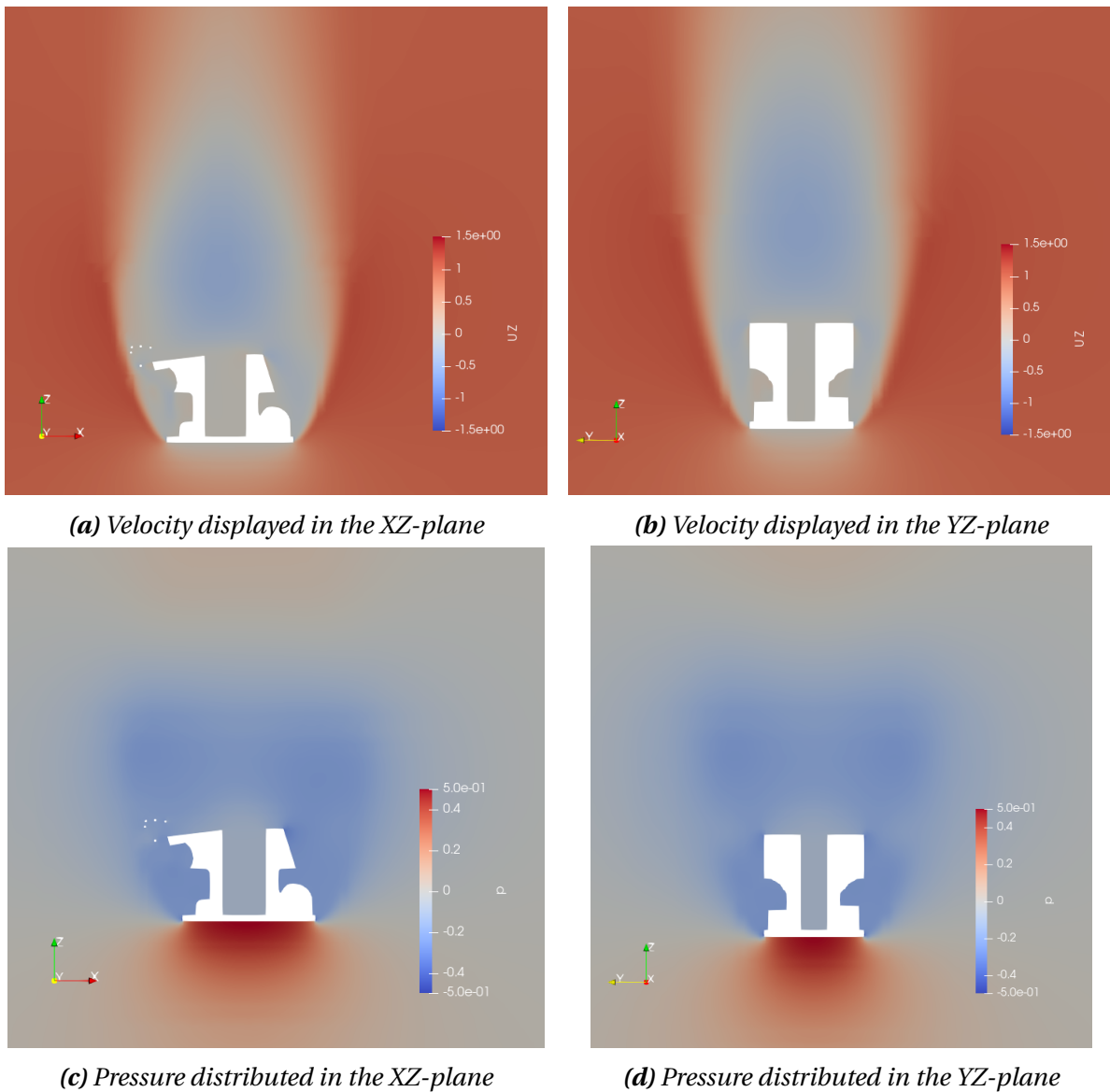


Figure 4.7: Contours of the stream-wise velocity and the pressure distributed under the incoming flow velocity of 1 m/s in heave

The flow and pressure distribution around the ROV seems symmetric, likely due to the geometry of the ROV. The bottom plate of the ROV is straight and symmetric around both the x- and y-axis. Also, six simulations have been made under six different incoming flow velocities for the last translational direction. Equation 2.34 is individualized and used to obtain the force in heave as a function of the flow velocity in the same direction. The plot for the relationship between the velocity of the incoming flow and the force in the heave direction is presented in Figure 4.8.

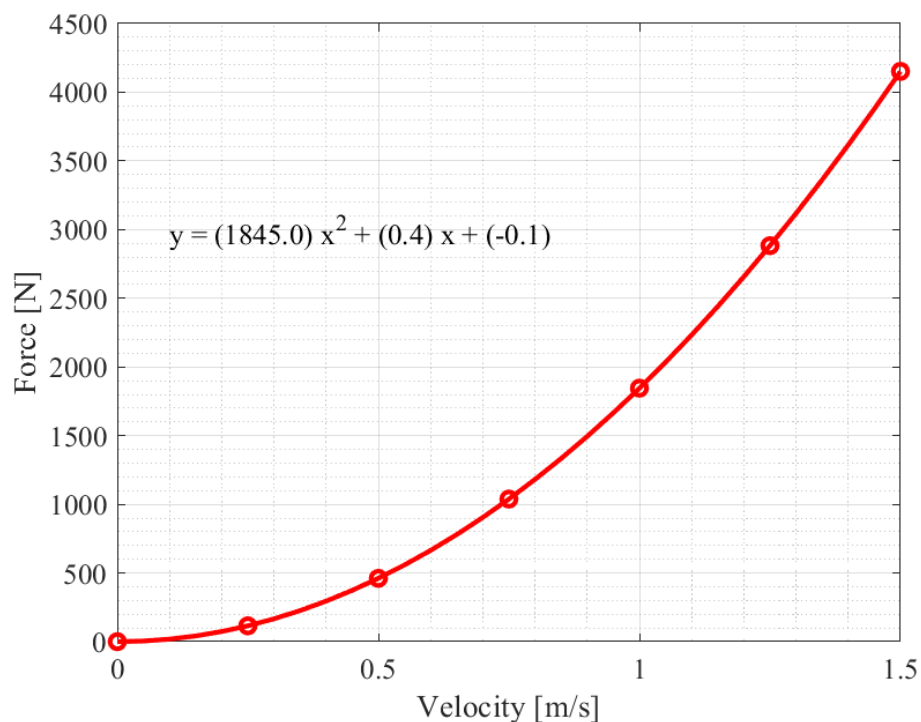


Figure 4.8: The linear and quadratic damping in heave found by using polyfit in MATLAB

The linear damping in heave due to a constant flow in this direction, Z_w , is found to be 0.4 Ns/m, and the quadratic damping, $Z_{w|w|}$, is 1845.0 Ns/m. Due to a similar cross-section as sway, the damping in heave is expected to be of similar magnitude to the damping in sway. In addition, the linear damping is also negligible, as for surge and sway. The damping for the translational directions is consistent with each other and relevant literature [2] [7] [9] [35]. Therefore, it is reasonable to assume that all these results are correct.

4.3 Rotation Arm Simulation

The rotating arm test will be recreated numerically, where the goal is to obtain the moment as a function of the angular velocity. Therefore, three different simulations will be carried out for the rotational DOF. The different angular velocities chosen are 0.1 rad/s, 0.2 rad/s, 0.3 rad/s, and 0.4 rad/s. Furthermore, Equation 2.35 is fitted together with angular velocity and the corresponding moment obtained from the simulations. Then, the linear and quadratic damping in the rotational motions is obtained. The equation is individualized for all rotational DOF to find the damping as a function of angular velocity in the corresponding directions.

4.3.1 Roll

The first direction considered is roll, the angular rotation about the x-axis. Here, four simulations are carried out with the velocities 0.1 rad/s, 0.2 rad/s, 0.3 rad/s, and 0.4 rad/s. Figure 4.9 presents the contour plots of the velocity along the y- and the z-axis and pressure distribution when the angular velocity is 0.2 rad/s.

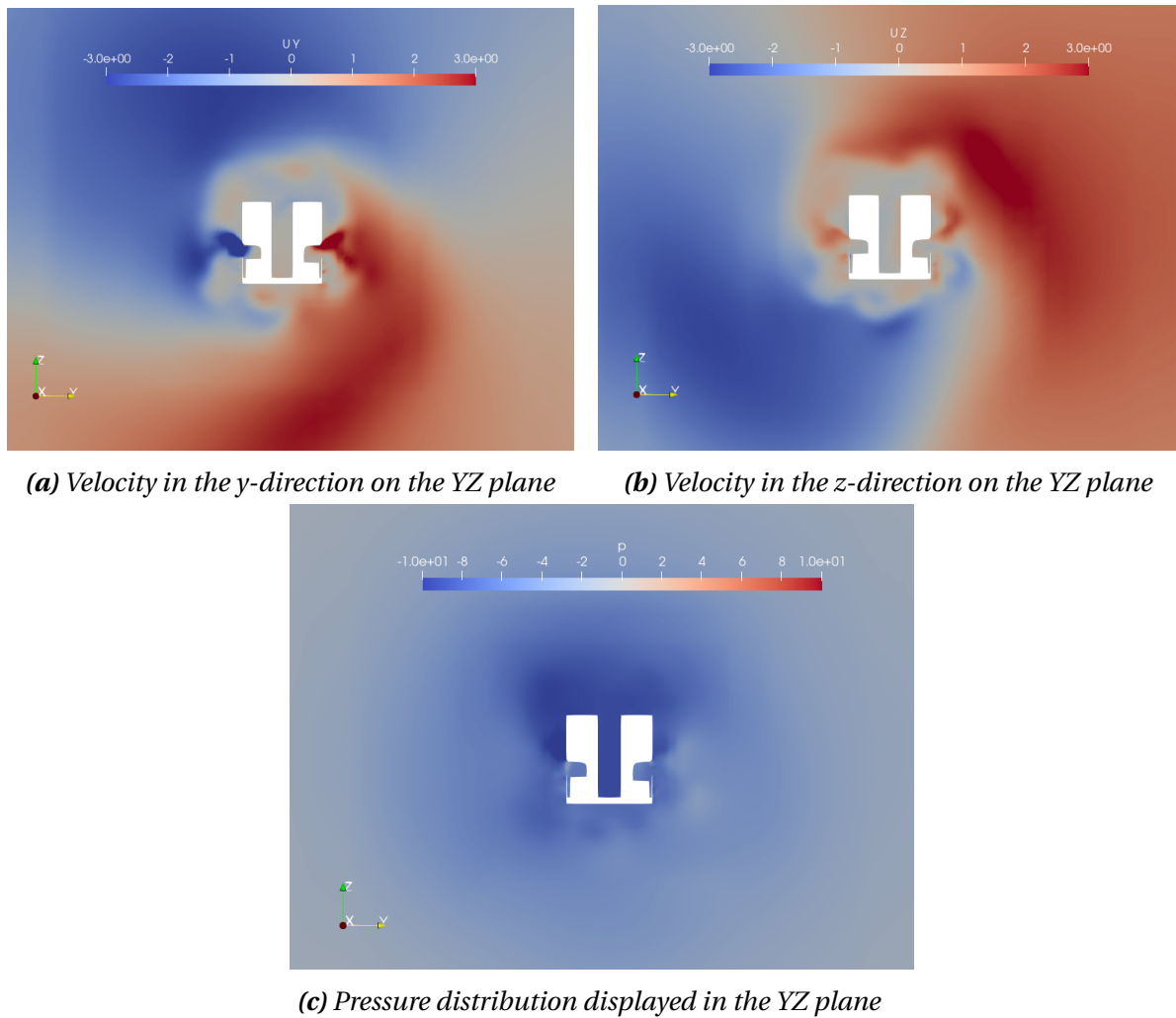


Figure 4.9: Contours of the flow velocity and the distributed pressure, 0.2 rad/s

The computational domain has a constant angular velocity around the x -axis. By studying the contour plots of the velocity, it is easy to see that the flow is moving counterclockwise. Due to this, it is reasonable that there is a negative pressure region around the ROV. This discovery is logical because the increased velocity around a body decreases the pressure. Therefore, it can be assumed that the simulations are reasonable.

Furthermore, Equation 2.35 is fitted together with the moment around the x -axis as a function of angular velocity around the same axis. Then, the linear and quadratic damping is calculated from the identified function. The plot of the function is presented in Figure 4.10.

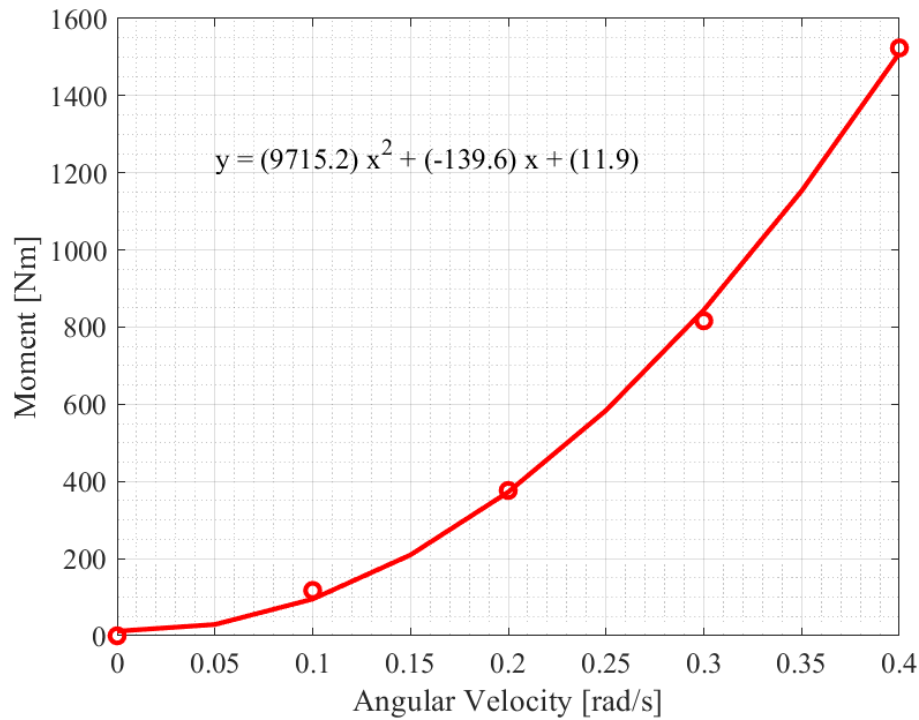


Figure 4.10: The linear and quadratic damping in roll found by using polyfit in MATLAB

Here, the quadratic damping, $K_{p|p|}$, is determined to be 9715.2 Nsm, and the linear damping, K_p , is calculated to be -139.6 Nsm. Upon examining the moment, it is observed that the fit of the function is acceptable. However, it is not as good as the functions produced in the linear directions due to a more complicated surrounding flow than the wake flow for translational motions.

Although the magnitude of the rotational directions is much higher than that of the linear directions, this is reasonable for the rotational damping of underwater vehicles. A study investigated the damping in surge and yaw, and the difference between them was significant [36]. Hence, even though the results obtained for roll are much higher than those in the translational directions, it is reasonable.

4.3.2 Pitch

The next direction simulated is pitch, the angular rotation about the y-axis. Four simulations are carried out with the same angular velocities as for roll. Figure 4.11 presents the contour plots of the velocity along the x- and the z-axis and pressure distribution when the angular velocity is 0.2 rad/s.

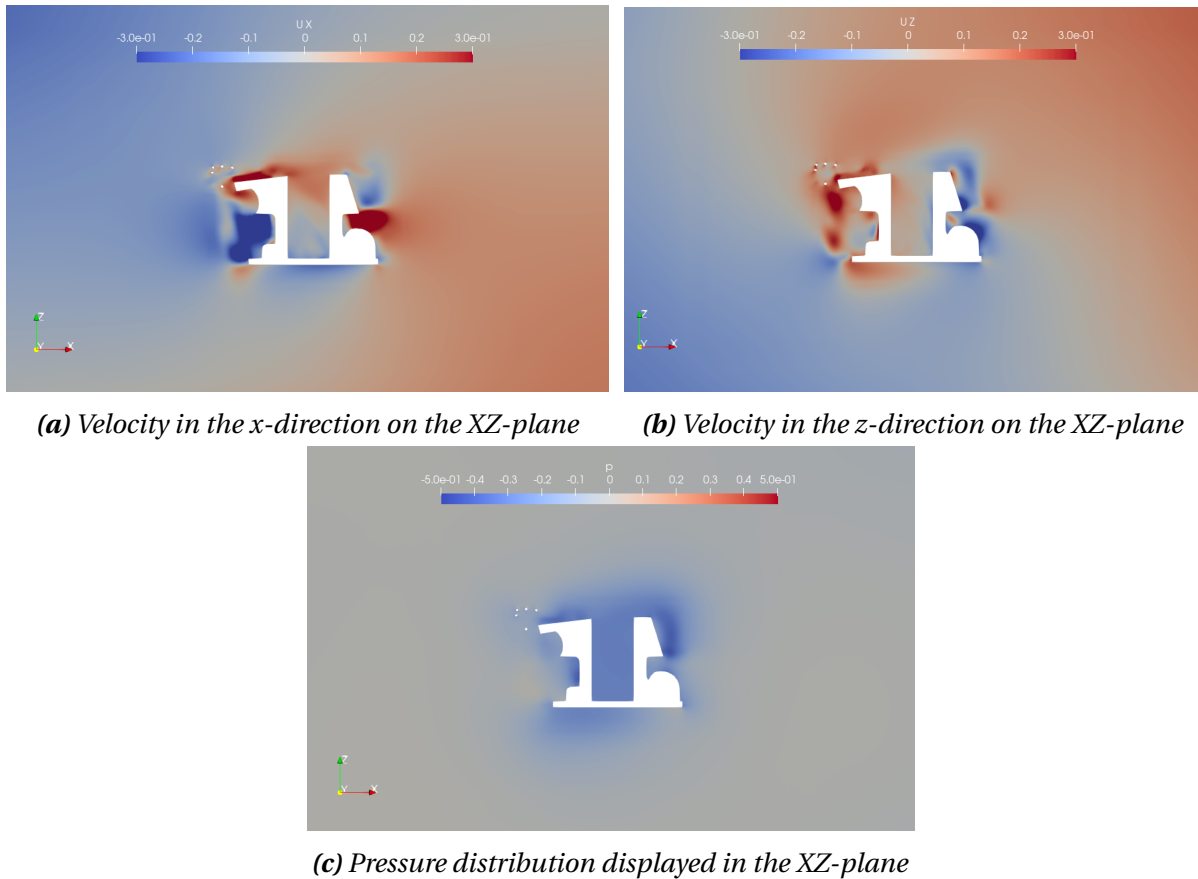


Figure 4.11: Contours of the flow velocity and the distributed pressure, 0.2 rad/s

By studying the contour plots of the velocity, it is shown that there is a constant angular velocity around the ROV. The result is constant and stable under pressure in the same area. The velocity and pressure values in pitch are smaller than those in roll. In addition, the transition between the positive and negative velocity is smoother. The reasoning could be a more stabilized simulation resulting in a more constant angular velocity.

This result is likely due to the simpler geometry of the ROV in the XZ-plane compared to the YZ-plane. This assertion is further supported by an excellent quadratic fit in Figure 4.12. Equation 2.35 specified for a pitch motion and fitted together with the angular velocity and the corresponding moment obtained from the simulations. The linear and quadratic damping in pitch can be calculated using data fitting.

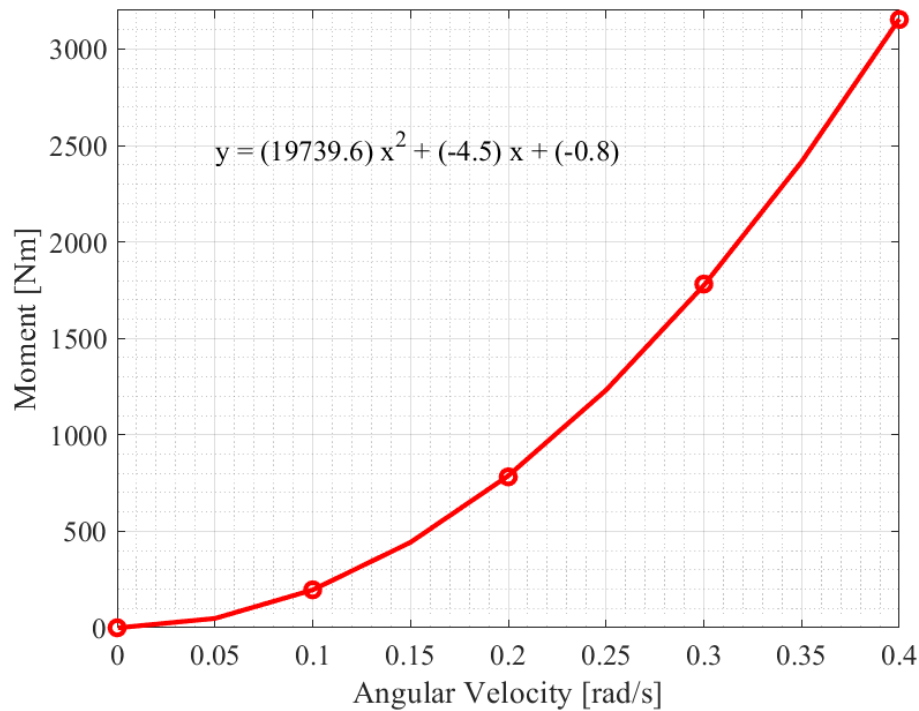


Figure 4.12: The linear and quadratic damping in pitch found by using polyfit in MATLAB

The quadratic damping is significantly higher for pitch than the damping in the translational directions. The linear damping, M_q , is negligible and is calculated to be -4.5 Nsm, and the quadratic damping $M_{q|q|}$ is 19739.6 Nsm. The quadratic damping in pitch is over twice as significant as in roll. This result is consistent with the findings of previous studies that have examined the rotational damping of underwater vehicles. However, the same studies found that the magnitude of the rotational damping is generally lower than the translational damping [9] [35] [37]. This result contrasts with the present study's observations and other papers [36]. Regardless, due to different discoveries in different literature, the pitch result is assumed to be reasonable. The field of research is small, and it is hard to predict the rotational damping of new and complex geometry.

4.3.3 Yaw

The last direction studied to obtain the damping is the yaw direction. As for the other rotational directions, the same four rotational velocities are simulated, and the rotation is about the z-axis. In Figure 4.13, the contour plots of the velocity along the x- and the y-axis is shown together with the pressure distribution.

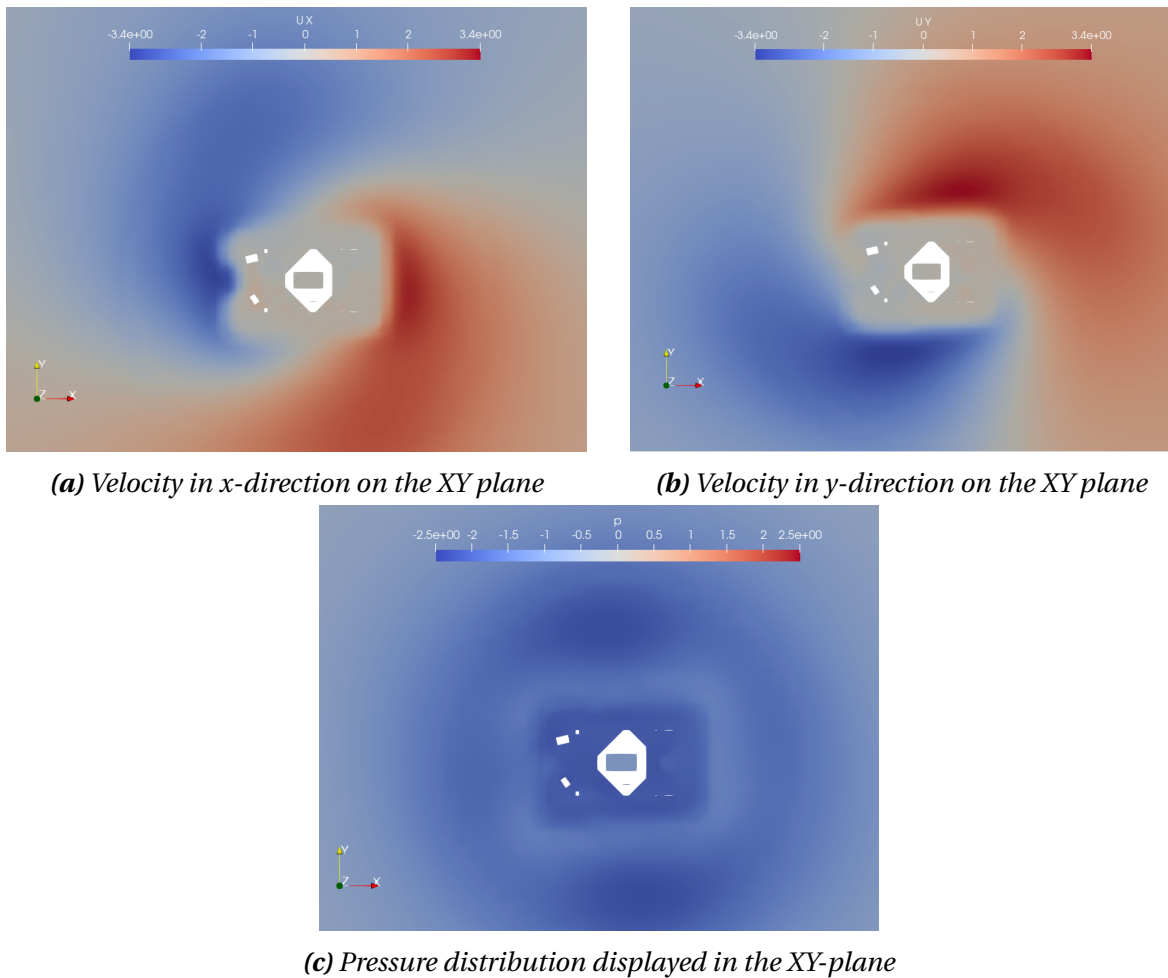


Figure 4.13: Contours of the flow velocity and the distributed pressure, 0.2 rad/s

By inspecting the two velocity contour plots, it is easy to see that the flow is rotating counter-clockwise. The ROV is surrounded by negative pressure due to the constant angular velocity. However, the magnitude of the velocities and pressure are close to the same as found in roll. A common feature between these two directions is that the thin plates are exposed to the flow. The linear and quadratic damping in yaw due to angular velocity in the same direction is calculated. Equation 2.35 is individualized to fit the current cases in yaw and is fitted to the simulated moment as a function of the angular velocity. The function is presented in Figure 4.14.

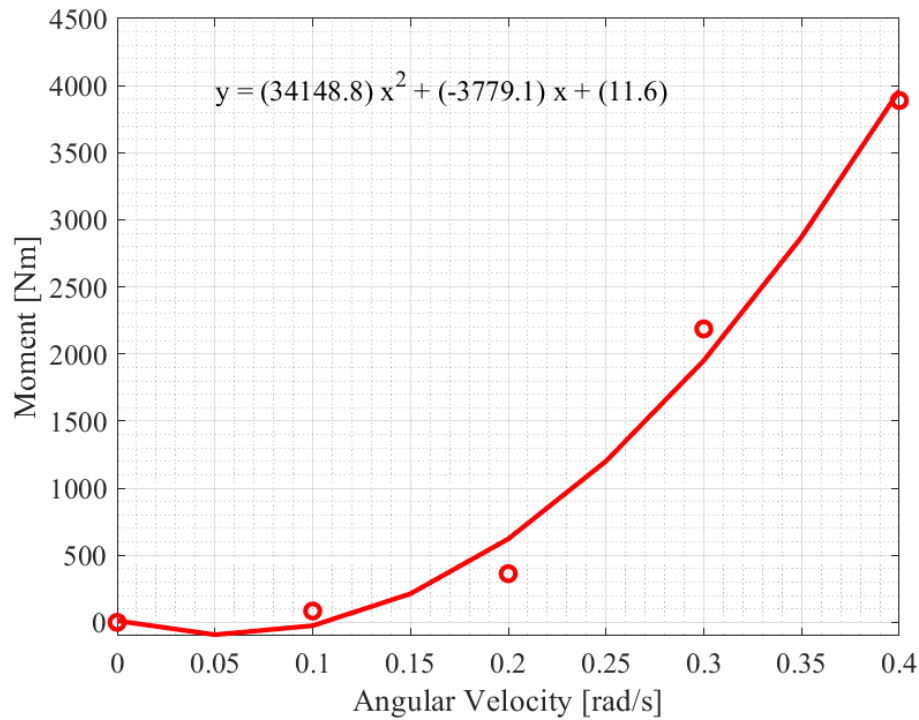


Figure 4.14: The linear and quadratic damping in yaw found by using polyfit in MATLAB

The damping in yaw is also higher than in the translational directions. However, the quadratic damping in yaw is the largest of the rotational directions. The quadratic damping in yaw, $N_r|r|$, is estimated to be 34148.8 Nsm, and the linear damping, N_r , is estimated to be -3779.1 Nsm.

When comparing the fit of the function, the fit in yaw is similar to roll. The moment as a function of the angular velocity gives a close fit to the simulated data, with some imperfections due to numerical errors. However, the fitted function in pitch is almost perfect to the simulated values. This finding substantiates the assumption that the geometry of the ROV makes the simulations of angular velocity in pitch more stable in the near wall region compared to roll and yaw.

The quadratic damping in yaw is almost twice the magnitude of the quadratic damping in pitch. This discovery is reasonable according to a previous study on a similar compact ROV, such as the study that found a similar relationship between the quadratic damping in pitch and yaw [37]. Nevertheless, the same study finds that rotational quadratic damping is much smaller than the translational quadratic damping. However, the relationship between the rotational quadratic damping and translational quadratic damping obtained in this work is also found in other papers [36]. Consequently, the damping found in the rotational directions can be assumed to be reasonable.

Moreover, it is essential to note that these simulations are complex, and the relevant research is limited. Therefore, the results of the present study can provide good guidance for the hydrodynamic analysis of ROVs with complex shapes.

4.4 Planar Motion Mechanism Simulation

PMM tests are simulated using CFD to find the added mass and inertia in all DOF. The equations used to describe the movement, total force, and to obtain the added mass and inertia are explained in Section 2.7.2. Oscillating linear and rotational displacement is simulated with different frequencies to calculate the added mass and inertia of the ROV for all DOF. A morphological mesh moves the ROV to create the oscillatory movement, shown in Figure 3.6. This method makes the forced oscillatory displacement in the desired directions possible.

4.4.1 Surge

The first direction considered is surge, and the displacement amplitude is 0.25 m. Five different simulations with different frequencies have been completed, which are 0.2 Hz, 0.4 Hz, 0.6 Hz, 0.8 Hz, and 1.0 Hz. Since the ROV oscillates, the surrounding flow field will change over time. The time-dependent flow field at some representative timesteps is shown. The timesteps chosen is when the force is at its minimum (t_1), when it is at its maximum (t_2), and when it is about zero (t_3). It is worth noting that when the force is about zero, the flow moves from the negative direction to the positive direction.

When there is an oscillatory movement, the flow field is more complex than the constant flow cases. The vorticity is selected to provide a qualitative view of the complicated and unsteady flow structures around the ROV. Figure 4.15 presents the pressure and vorticity for each timestep.

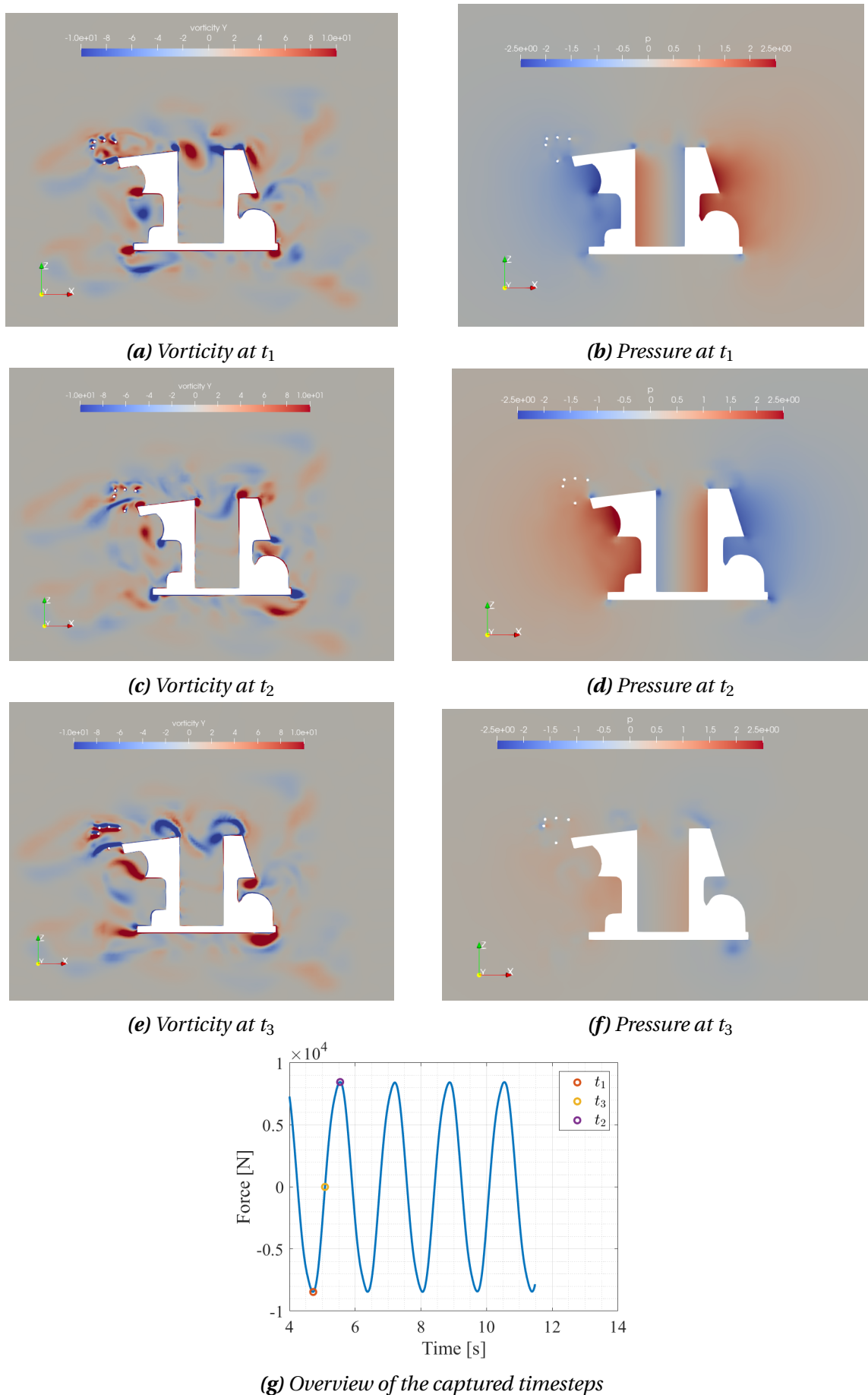


Figure 4.15: Vorticity and pressure as a result of an oscillating movement in surge with an oscillating frequency of $f = 0.6$ Hz

At t_1 , the ROV is moving in the positive surge direction and is generating a positive force. At t_2 , the ROV moves in the negative surge direction, generating a negative force. At t_3 , the ROV is moving from t_1 to t_2 , which is from negative directed force to positive directed force.

Here, the vortex generation is similar when comparing t_1 and t_3 . At t_1 , the vortex intensity is near the sharp edges of the ROV, increasing the pressures on the surface of the ROV at specific points. When studying the vorticity at t_3 , the vortices are also generated around the sharp corners, but the vortices are shedded from the walls. The vortex shedding causes the pressure to decrease, which is possible to confirm when studying the pressure at t_1 and t_3 . However, the directions of the vortices at t_1 and t_2 are the opposite, which leads to forces with the same amplitudes and different signs at t_1 and t_2 .

When all five simulations are completed, the added mass is calculated. Equation 2.38 is used with the MATLAB fit function to find the in-phase and out-phase components. X_{ii} is calculated for all simulations using Equation 2.39. The added mass is constant for all frequencies, presented in Figure 4.16. The final added mass in surge is calculated to be 2290.1 kg.

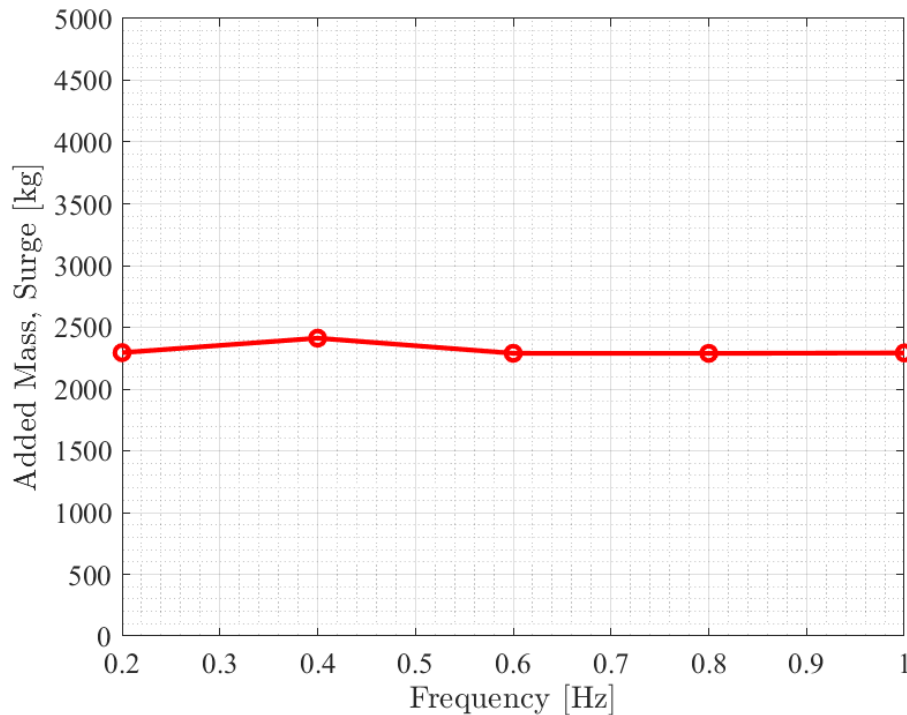


Figure 4.16: Added mass in surge for the different frequencies

4.4.2 Sway

Oscillatory motion simulations in the sway direction are carried out using V2. As stated earlier in Section 4.1.1, the number of cells used for V2 is almost three times as used for V1. Based on this information, the simulations in sway are expected to require a long time to complete. Due to the finding that the added mass in surge is constant for all frequencies checked, it is assumed that the added mass in sway should also be constant with different frequencies. Therefore, only two simulations with the same amplitude as surge and the frequencies 0.6 Hz and 0.8 Hz have been completed to obtain the added mass in sway.

As presented in Equation 2.37, an inlet velocity in surge is implemented when performing a sway motion. The velocity is set to 0.25 m/s, equivalent to about 0.5 knots, a reasonable operating velocity for this ROV. The contours for the vorticity at $f = 0.6$ Hz are presented in Figure 4.17. Here, t_1 , t_2 , and t_3 are timesteps captured in the same order as presented in Figure 4.15g.

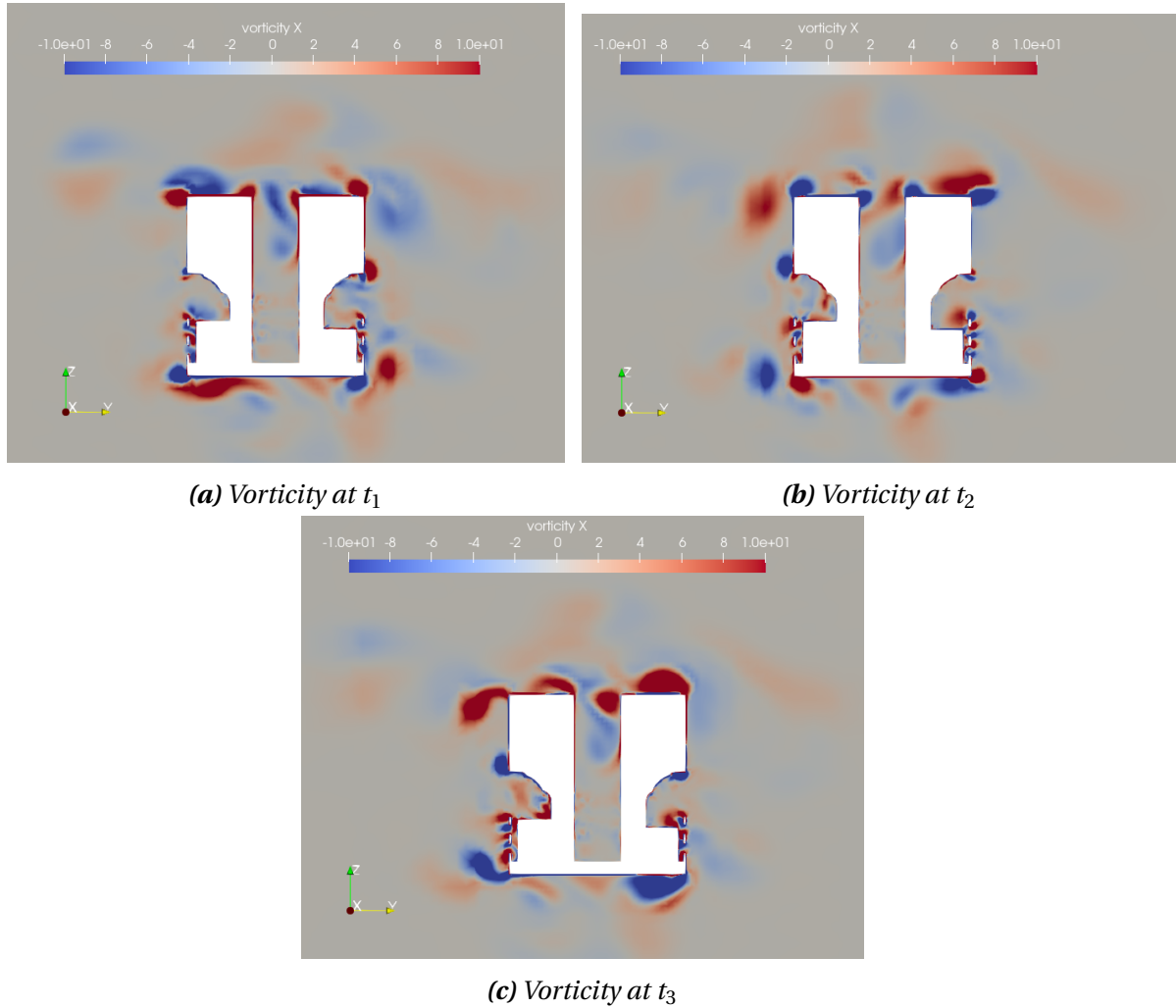


Figure 4.17: Vorticity as a result of an oscillating movement in sway with an oscillating frequency of $f = 0.6$ Hz

Here, similar characteristics can be viewed in the sway to those for the surge directions. At t_3 , the vortices are shedding compared to the previous timestep, t_1 . As found when studying the surge direction, this will reduce the pressure and further reduce the force generated. This outcome is logical since t_3 is the timestep where the force is close to zero.

Subsequently, the ROV is almost symmetric about the x/surge-axis. This fact is relevant when comparing the vorticity at t_1 and t_2 . Here, the characteristic opposites can be found when comparing the similar timesteps in surge. The difference here is that the flow fields for the sway directions are more symmetric, making the opposites more visible. In sway, when the t_1 and t_2 are captured, the vortex intensity is almost identical, but the directions are switched, and their spatial locations are mirrored.

The added mass is calculated using the same method and equations as when calculated in

surge. The added mass is constant for all the frequencies, similar to Figure 4.16. The final added mass in sway, $Y_{\dot{v}}$, is calculated to be 4164.6 kg.

When comparing to surge, it is essential to note that the magnitude of the added mass in sway is almost twice as large as in surge, and this is reasonable since the cross-section area is almost twice as big in sway compared to surge.

4.4.3 Heave

The same method as used in surge and sway is used to calculate the added mass in heave. The same amplitude, frequencies, and inlet velocity in sway are also used for heave. In Figure 4.18, the contour of the vorticity is presented under an oscillating frequency of 0.6 Hz. The figure shows three different timesteps when the force is at its minimum and maximum and when the force is about zero. These are known as t_1 , t_2 , and t_3 and have the same order and placement as shown in Figure 4.15g.

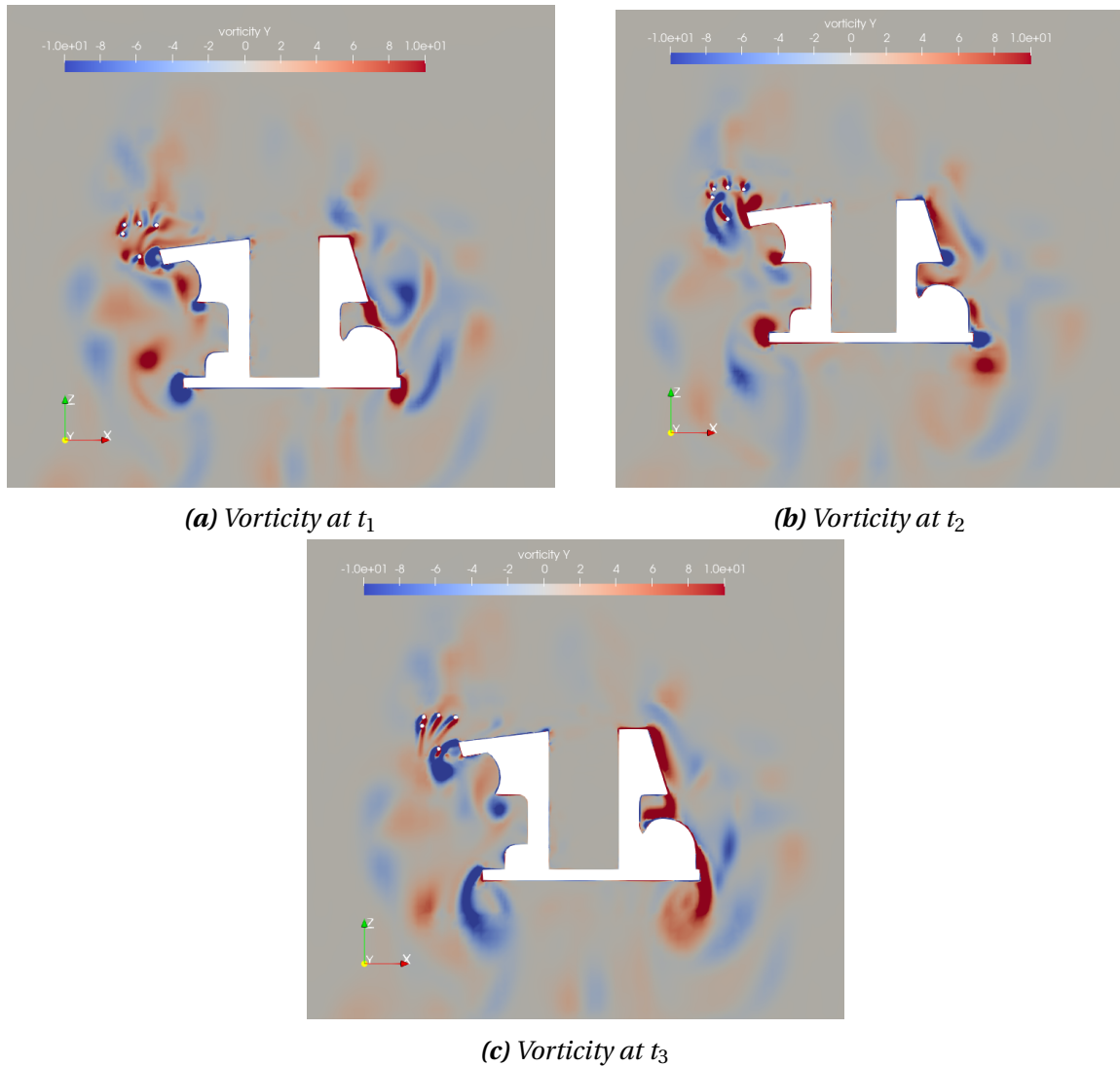


Figure 4.18: Vorticity as a result of an oscillating movement in heave with an oscillating frequency of $f = 0.6$ Hz

Vortexes generated under an oscillatory heave motion are similar to surge and sway. The generation locations of vortexes are similar when comparing t_1 and t_3 . Vortex shedding will occur during the time change from t_1 to t_3 . At the timesteps t_1 and t_2 , the magnitude of the vorticity is high and located near the sharp edges. As experienced when studying the surge motion, this results in large pressure near the wall. This flow behavior increases the magnitude of the force generated at these timesteps.

Eventually, the common denominator is that all three translational directions have similar characteristics. When the force is about zero (t_3), the pressure drops to about zero due to the vortex shedding. When the force is at its negative and positive peak, the generation of vortexes is more concentrated at the near wall of the ROV. This phenomenon causes an increase in

pressure and an increase in force. The signs of the generated vortices at the timesteps of t_1 and t_2 are opposite with similar amplitudes. However, the symmetry of the overall shape in the plane normal to the oscillating axis tends to influence the vorticity pattern with opposite signs.

Nevertheless, the results from the simulations in heave are used to calculate the added mass, and the same equations used in surge and sway are used. Equation 2.38 is used together with the MATLAB fit function to find the in-phase and out-phase components. Equation 2.39 is used to obtain the added mass in heave, Z_w . The added mass is calculated to be 5277.1 kg and is constant for both frequencies, similar to Figure 4.16.

The added mass in the sway and heave direction is higher than in the surge direction. The added mass in heave is also the largest of all the translational directions. This observation may be because of the hole where the tether is placed, exemplified in Figure 4.18, as the rectangular form in the middle of the ROV. This hole will trap the flow inside and create an extra drag when the ROV moves in the negative heave direction. It can be discussed if this is the correct simplification of the ROV, and it could be an idea to check the change in drag if the hole is filled. This finding is reasonable due to the dissimilarity of cross-section area and other geometrical differences.

4.4.4 Roll

The hydrodynamic added inertia is also studied in the rotational directions. A forced oscillatory rotational motion is exerted on the ROV, and the angular displacement, velocity, and acceleration are expressed in Equation 2.40. Here, a similar method to find the added inertia is used, and Equation 2.42 and 2.43 is used to obtain the added inertia.

Roll is the first direction studied and is the rotation about the x-axis. An oscillatory rotational movement is forced, and the amplitude of the rotational motion is 15° relative to the rotating axis. This means that the maximum forth and back angle of the ROV roll is 15° . Four different frequencies are chosen for this rotating movement: 0.25 Hz, 0.5 Hz, 0.75 Hz, and 1.00 Hz, and are in the range of expected roll frequencies.

Since the movement is an oscillatory motion, studying the vorticity distributed around the ROV is also interesting. Figure 4.19 presents the contour plots for the velocity and pressure. Here, three representative timesteps are chosen, which are when the magnitude of the moment is minimal, maximal, and zero. These timesteps are marked in Figure 4.19g, where t_1 is the minimal moment, t_2 is the maximum moment, and t_3 is when the moment is about zero.

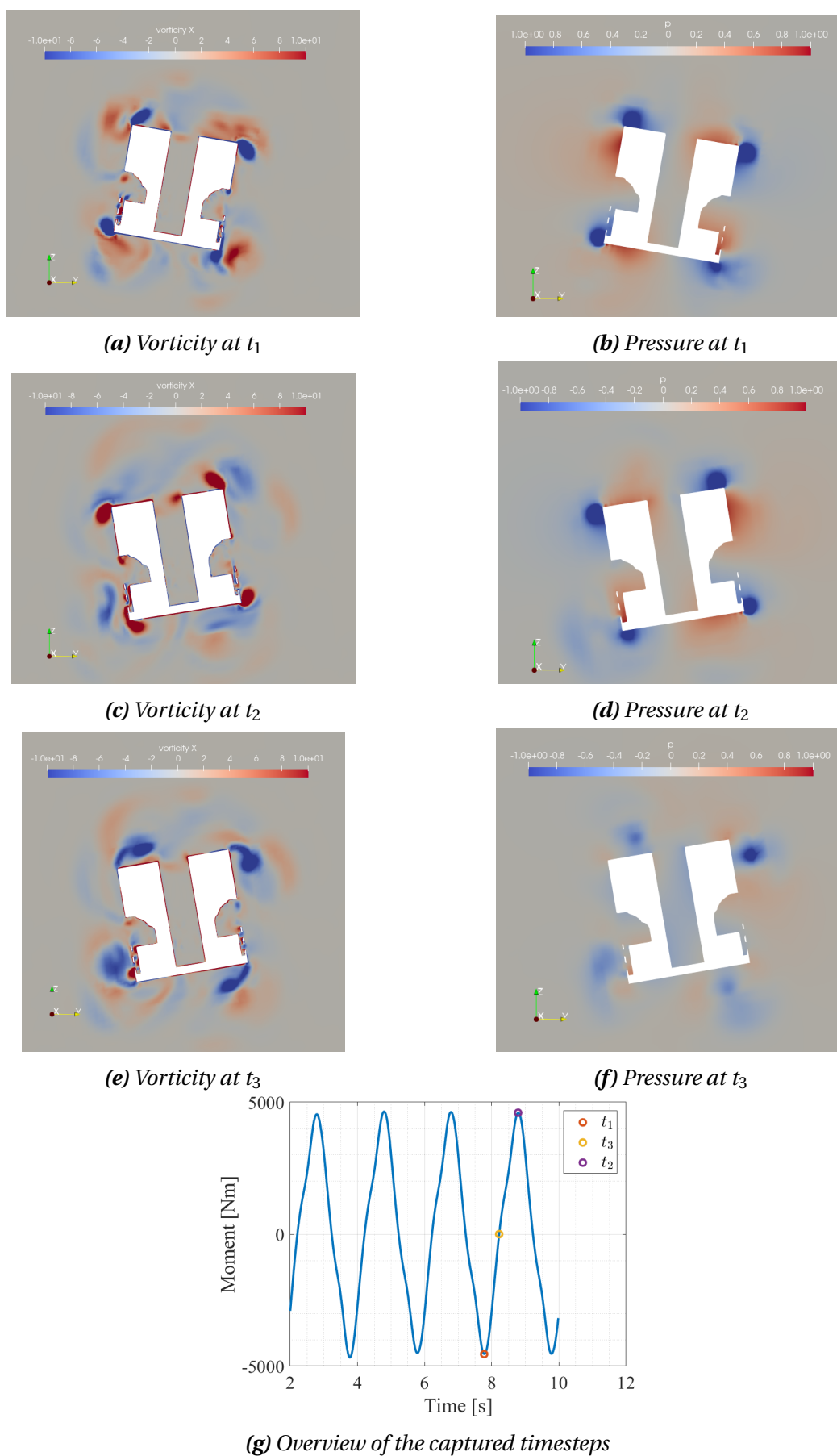


Figure 4.19: The vorticity and pressure measured at the representative stages of the roll motion with an oscillating frequency of $f = 0.5$ Hz

In Figure 4.19a and 4.19c, the formation and organization of the vortexes appear similar, but they are mirrored about the z-axis. The vortexes also rotate in opposite directions. The mirroring pattern is also visible for the pressure at the applicable timesteps. This phenomenon is reasonable since the moment generated at t_1 and t_2 have about the same magnitude but has the opposite direction. A roll motion is a rotation about the x-axis, and the ROV is almost symmetric about the x-axis. Therefore, it is logical that the moment, vorticity, and pressure generated at t_1 and t_2 are of the same magnitude but have different directions.

Another circumstance worth studying is the angle of Figure 4.19e, t_3 . The ROV is not leveled here, even though the moment is almost zero. Figure 4.19g shows that t_3 is captured during the transition from negative to positive moments, resulting in the tilting of the ROV at t_3 . However, the ROV is leveled from t_1 to t_3 at a specific timestep. There is no forced movement when it is leveled, but there are still negative moments from the flow acting on the ROV. Hence, the ROV must move beyond the leveled position to generate a positive moment. Over time, the moment is eventually equalized, resulting in a total moment of zero. This timestep corresponds to the generation of t_3 .

Other parameters are studied to check if this simulation is reasonable. Therefore, in Figure 4.19, the pressure distribution is also presented for all three timesteps captured. This figure uses the same pressure scale for the different timesteps to view the relative difference. The magnitude of pressure is larger at both t_1 and t_2 compared to t_3 . This contrast is expected since this pressure difference will create a force, further creating a moment. The pressure is generated from an accelerating angular movement. When studying the pressure field, positive and negative pressure regions are shown on both sides of the ROV. The positive pressure indicates that the ROV is pushing against the fluid and creating a positive pressure gradient due to the acceleration. The negative pressure indicates that the ROV under suction effects by the fluid.

The vorticity is at its largest magnitude for t_1 and t_2 , where the pressure is the most negative. The stronger vorticities lead to higher pressure-induced forces and moments. The vortexes begin to grow at t_1 and t_2 and are not shed, creating the large negative pressure regions at these timesteps. It is worth noting that at t_3 , vortexes are shed from the corners. As expected, the strength of the large negative pressure zones is reduced. Figure 4.19 indicates that the desired roll motion is accomplished. Therefore, it is reasonable to assume that this method is also accurate for pitch and yaw.

At last, the added inertia in roll, $K_{\dot{p}}$, is calculated using Equation 2.42, and finding the in-phase and out-phase components using MATLAB the fit function. The calculation of added inertia has been performed for all four cases using Equation 2.43. The results are consistent and are presented in Figure 4.20. The added inertia in roll is $1148.4 \text{ kg}\cdot\text{m}^2$.

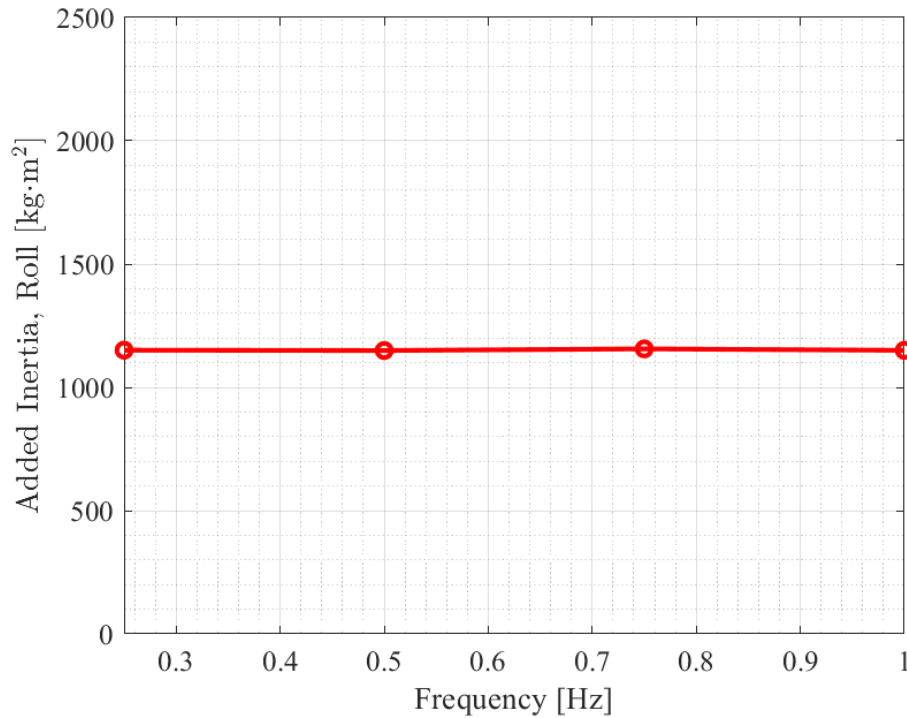


Figure 4.20: Added inertia in roll for the different frequencies

4.4.5 Pitch

The next rotating direction studied is pitch. Here, the same method as the previous section is carried out, and a forced oscillatory rotating motion with the same amplitude is utilized. The difference from the roll cases is that an inlet flow of 0.25 m/s is implemented, which is equal to a normal operating velocity of this ROV. The motion for the pitch simulations is expressed in Equation 2.41. Simultaneously only two cases are constructed, with frequencies of 0.25 Hz and 0.50 Hz . The reasoning for the reduction in cases is that the added inertia in roll is stable for all four frequencies. Therefore, pitch is expected to be stable, and only two cases are needed to verify the stability of the added inertia.

Since this motion is an oscillatory movement, the vortex intensity at specific timesteps is interesting. Figure 4.21 displays the vortex intensity for a pitch motion at 0.5 Hz . The timestep chosen to be studied is when the moment is at the minimal and maximum magnitude and when the total moment is about zero. These are written respectively as t_1 , t_2 , and t_3 . The

timesteps are named accordingly, as shown in Figure 4.19g.

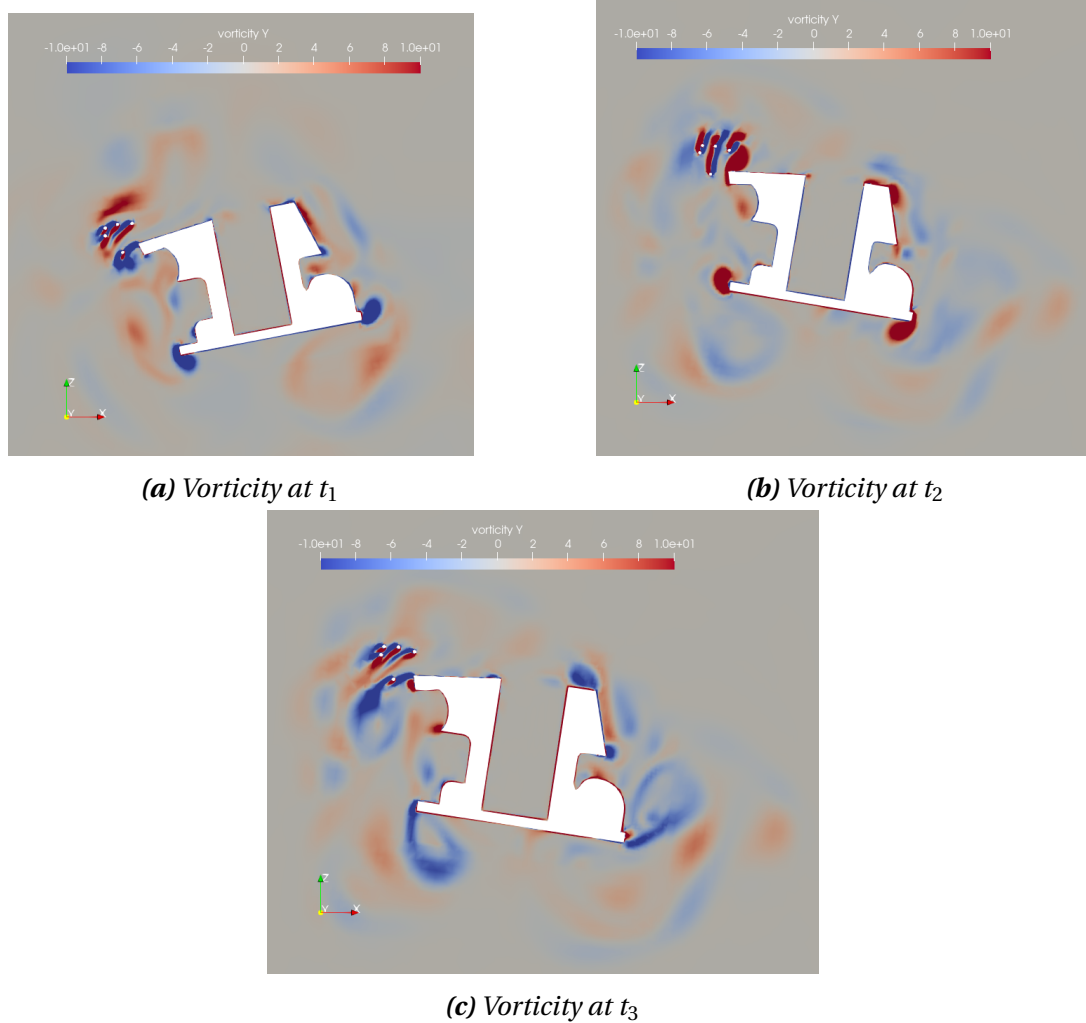


Figure 4.21: The vortex intensity measured at the representative stages of the pitch motion with an oscillating frequency of $f = 0.5$ Hz

Here, similar trends are common denominators when comparing pitch and roll motion. At t_1 , the vortex intensity is dominated by a negative contour in the near wall region, while at t_2 , the surrounding flow is dominated by positive vorticity. Unlike the roll motion, the similarity of the vorticity patterns is not obvious between t_1 and t_2 . The roll motion is rotation about the x-axis, and the ROV is almost symmetric about this axis, while pitch is rotation about the y-axis, where the ROV is not symmetric. Therefore, the formation of vortices at t_1 and t_2 are expected to differ.

Another phenomenon found when studying Figure 4.21 is that at t_1 and t_2 , the vortices shedding has not occurred around the two lower corners of the ROV. As found in the previous section, when the vortices begin to form around the corners, large negative pressure zones

are created, which lead to the minimum and maximum moments at t_1 and t_2 . In addition, there are massive flow separations around the circular frames in the upper front of the ROV, which also contribute to the moment.

Furthermore, the added inertia in pitch, $M_{\dot{q}}$, is calculated using Equation 2.42, but defined for the pitch motion. The MATLAB fit function is used to find the in-phase and out-phase components, and the in-phase value is afterward used to calculate the added inertia. The added inertia is calculated for the two different frequencies for both cases using Equation 2.43. As expected, the added inertia for pitch is the same for both frequencies, and the consistency is similar to Figure 4.20. The added inertia is calculated to be $2016.0 \text{ kg}\cdot\text{m}^2$.

4.4.6 Yaw

The last direction studied in the present PMM test study is yaw. The same method, amplitude, and frequency as for pitch are implemented when forcing a yaw motion, and the same timesteps are found when studying the vortex intensity. In Figure 4.22a and 4.22b, the vortexes are presented when the time captured is t_1 and t_2 . In Figure 4.22c, the time captured is t_3 . The timesteps referred to are in the same order as in roll and pitch and are presented in Figure 4.19g.

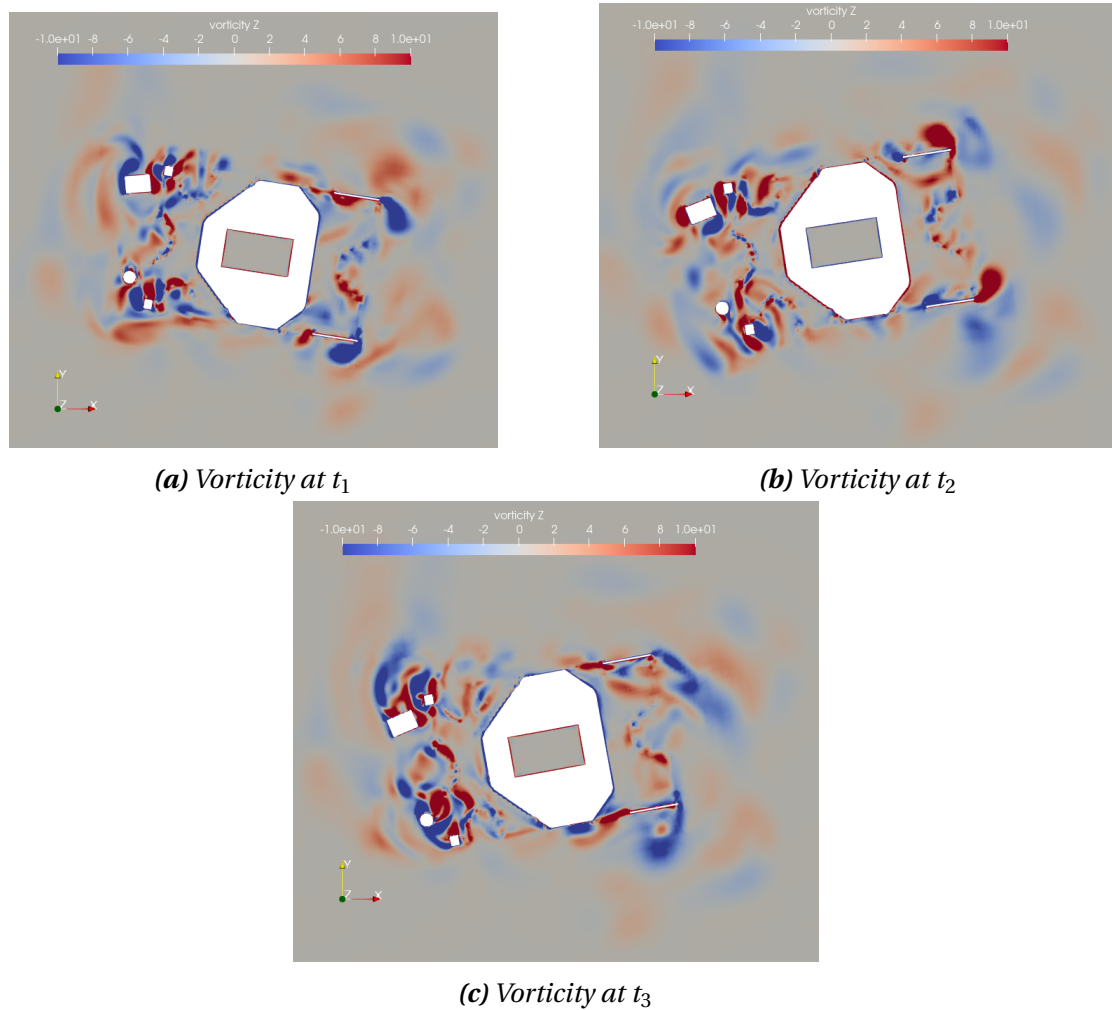


Figure 4.22: The vortex intensity measured at the representative stages of the yaw motion with an oscillating frequency of $f = 0.5$ Hz

Here, the view is displayed from the top view. The flow is moving through all the detailed parts of the ROV. Therefore, the vortices seem more chaotic than the other two rotational directions. Regardless, the same similarities between t_1 and t_2 are visible and more noticeable at the back corners of the ROV. In these two points, the intensity is large and has different rotational directions at t_1 and t_2 .

By understanding the formation of vorticity in roll and pitch, it is possible to predict that the high concentration of vortices in yaw also will create large negative pressure regions. When the time is at t_3 , the vortex shedding has taken place, and the strength of large negative pressure regions will be reduced.

The added inertia for the yaw motion, $N_{\dot{\gamma}}$, is calculated by implementing a yaw-defined Equation 2.42 and 2.43. The in-phase and out-phase components are found using the MATLAB

fit function. The in-phase component is further used to find the added inertia in yaw. As expected, the added inertia is the same for both frequencies considered, and the consistency is similar, as presented in Figure 4.20. The calculated value is $1709.6 \text{ kg}\cdot\text{m}^2$.

4.5 Validation with Operational ROV

Sea tests are carried out to validate the hydrodynamic added mass and damping obtained by using CFD. The operational ROV stationed at SNB is used to validate the results. The central equipment mounted on the ROV and the cage is the SPRINT and the current meter. These two instruments make it possible to measure the linear and angular position, velocity, and current in the near region of the ROV.

During this work, there have been discovered errors with the SPRINT's DVL. Therefore, the logged data of the linear positioning and velocity is inaccurate. This issue is because the accelerator alone measures the position and velocity, which makes the data's uncertainty high [29]. Even though there are problems with the SPRINT, new logged movement datasets from 2023 are obtained. Ten sea trials were carried out in 2023 to capture the described movement, and the current was measured to be about 0.15 m/s on average.

Due to the problems with the SPRINT, a sea test from 2021 is studied to validate the numerical results. IKM Subsea performed a sea trial in 2021 when the SPRINT gave valid data, but the current meter was not mounted on the cage, which may affect the positions and velocities of the ROV. The purpose of this dataset was to investigate the possibilities of developing a new ROV simulator. Hence, the movements of the ROV are in all four DOF surge, sway, heave, and yaw, and combined movement between these DOF. Although this dataset may not be optimal for validating the singular DOF parameter, capturing a complicated ROV movement should still be feasible.

The simulator uses the added mass and quadratic damping obtained by CFD to validate the hydrodynamic parameters, while the linear damping is neglected. The linear damping is small for the translational direction and can therefore be neglected, which is also the case for pitch. According to [2] [7] [9] [35], the linear damping in roll and yaw may also be negligible. Furthermore, the added mass and damping may require adjustment for all DOF. The goal is to evaluate the efficiency of the method and whether agreement with the recorded data can be achieved. Only some of the directions are presented as an example.

The simulator code is set up with a thrust conversion function without dead-zone, presented in Equation 2.31. The weight, W , is set to 2750.0 kg, and the buoyancy, B , is set to 2753.2 kg. The offset from the CB to the CO, x_b , y_b , and z_b are respectively set to -0.025 m, -0.001 m, and -0.3 m. These parameters are unknown since the ROV is in operation, but the weight is chosen

as the estimated weight. The buoyancy and the offset are also close to the estimation, but they must be adjusted to achieve the best fit to the logged data for the future use of the simulator [1] [4]. For the thruster data, the commanded input RPM is chosen.

Different variants of these parameters are tested, and the selected ones which provide the best fit between the simulated and recorded movement are used to build the simulator. These parameters are the same for CFD estimated added mass and damping and the adjusted hydrodynamic parameters. This method is to properly and systematically adjust the hydrodynamic added mass and damping.

4.5.1 Validation of the Translational Directions

The logged dataset from 2021 must be studied to validate the linear damping and added mass. The position and velocity in heave are studied. Figure 4.23 presents the logged and simulated position and velocity in heave.

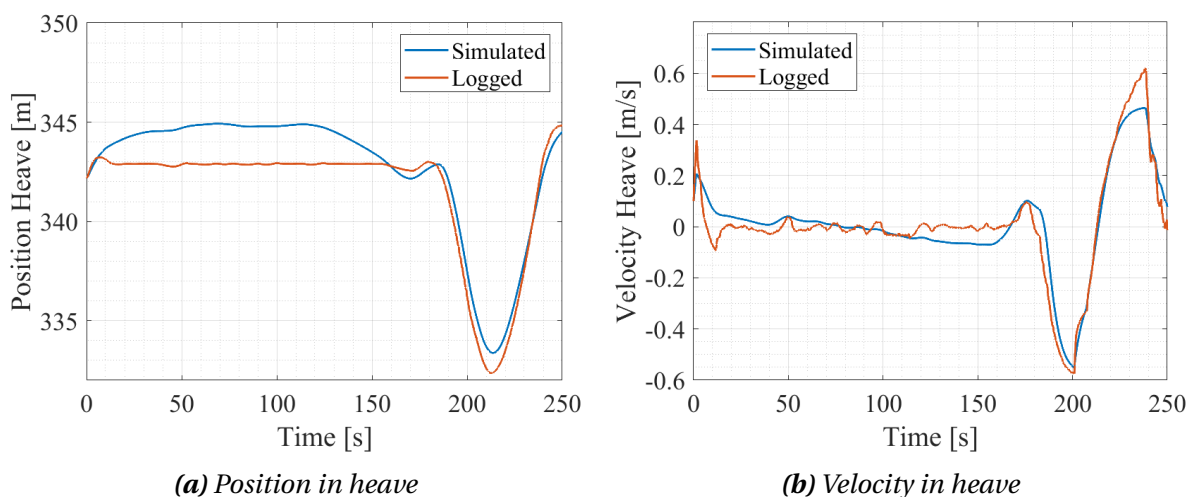


Figure 4.23: Logged and simulated position and velocity in heave

These figures show similar trends between logged and simulated position and velocity. Note that the z-axis is the same for NED and BODY and is the ROV's depth. The overall agreement of the simulated position and velocity in heave with the recorded data is satisfactory. However, the position is off from 10 s to 150 s. The offset is not large, and the maximum offset is about 2.0 m. The position offset could be because the ROV uses the auto depth function in this interval, and this function initiates regular thrust to keep the ROV at the same depth. The combination of this function and the gravitation and bouncy forces in heave may explain the deviation. However, afterward, the fit is close in position. The peak value is at 215 s with an

offset of about a meter and occurs almost simultaneously, indicating that the added mass is well-estimated.

Similarities are found when the logged and simulated velocity in heave is studied. The primary three representative timesteps are 175 s, 202 s, and 239 s. Here, some characteristics are observed in logged and simulated velocity.

The first peak at 175 s has approximately equal logged and simulated velocity. The only difference is that the logged velocity is steeper than the simulated velocity. At 202 s and 239 s, there are negative and positive peak values for the logged and simulated velocity in heave. At the negative peak timestep, the difference is negligible, but at the positive peak timestep, the difference is about 0.15 m/s. There is almost no delay in the plots, indicating that the estimation of the added mass is good.

Even though the simulator cannot fully recreate the logged data with the present hydrodynamic parameters, similar trends are observed. The general agreement between logged and simulated position and velocity in heave are acceptable, indicating reasonable values for the added mass and damping.

The last two translational directions, surge and sway, are also important. Even though the current is present in these directions, it is vital to study the results. Movement in the surge direction is the most common operation for a working ROV. However, in Figure 4.24, only the velocity in surge and sway is presented. The position is not shown due to the dependency on highly accurate yaw since the position is calculated in NED. Therefore, the logged and simulated position is not close and may be misleading. Hence, the velocity is independent of yaw in the BODY reference frame.

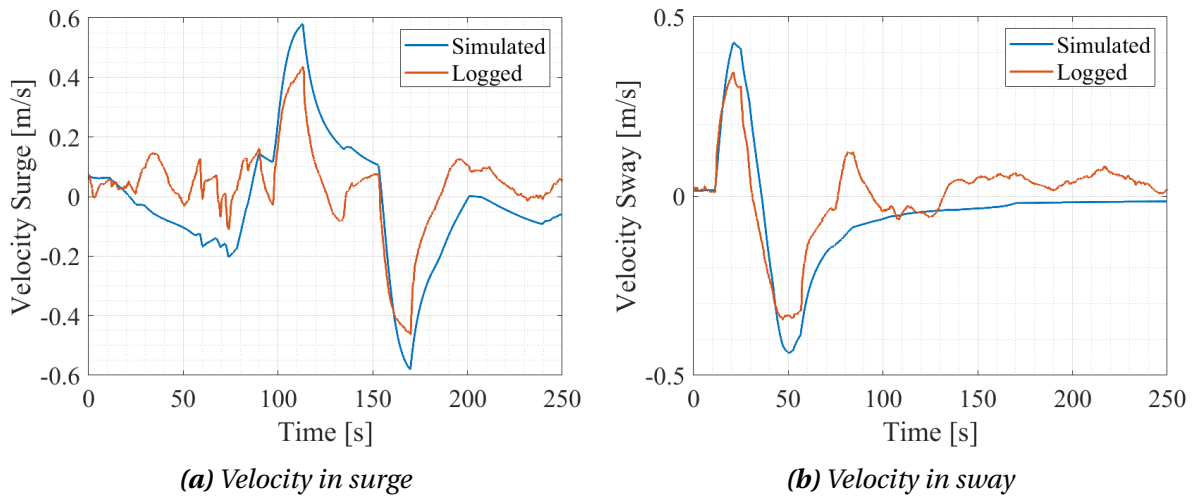


Figure 4.24: Logged and simulated velocity in surge and sway

Here, the overall fit is also acceptable but less satisfactory than the velocity in heave. Note that the simulated velocity has more significant peaks than the recorded velocity in surge and sway. This phenomenon is expected, and it is assumed that this is because of the current and a higher tether drag in the horizontal directions. At SNB, the tether is designed with an added buoyancy, causing the tether to float vertically. This setup leads to increased resistance in horizontal directions while resistance in heave is reduced. Therefore, the RPM of the thrusters must increase to achieve the same velocity as if there is no extra drag. An explanation for these findings is that the tether is too tight near the peaks.

Nevertheless, another explanation could be the sea current. Throughout this work, the current at SNB is measured to be about 0.15 m/s on average, and the differences in the peaks are from about 0.10 m/s to 0.15 m/s. Therefore, the current could be a contributing factor to the deviation.

The simulator code does not consider the current and tether, and the velocity is expected to be overpredicted. Hence, the added mass and damping found using CFD are regarded as reasonable for all translational directions. However, the effects of the current and tether should be investigated to find the contribution of the movement of the ROV.

4.5.2 Validation of the Rotational Directions

The same dataset is studied to validate the rotational directions. In this work, the whole dataset is studied, and it is found that the first 120 s fully represents the behavior of the ROV. Therefore, only the first 120 s of the logged data are shown to understand the characteristics

of the oscillatory positions and velocities of roll and pitch. Figure 4.25 presents the simulated and logged positions and velocities for all the rotational directions.

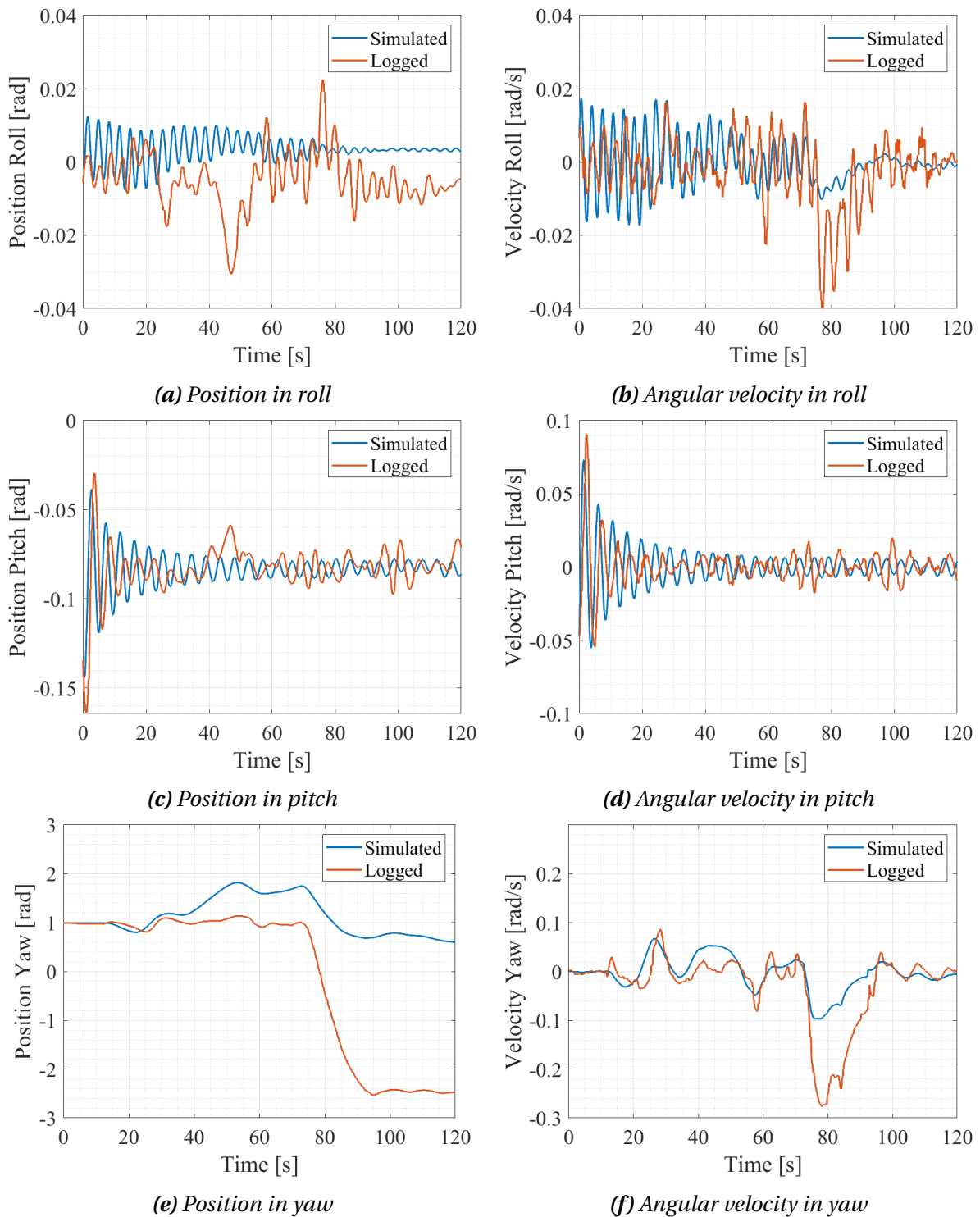


Figure 4.25: Logged and simulated positions and angular velocities in the rotational directions

Roll and pitch have similar characteristics of motions. In this case, the movements in the other directions induce the movements in roll and pitch. The position and velocity oscillate due to

the offset of the center of buoyancy to the center of origin. On the other hand, the movement in yaw is determined, and the position of yaw decides the heading of the movement. Thus, it is crucial to accurately predict the yaw to simulate an accurate position in surge and sway in NED.

The simulated position roll is in good agreement with the logged data during the initial 20 s. However, beyond that timestep, the simulated position deviates from the recorded data. Despite this, the simulated position in pitch consistently aligns with the logged position throughout the dataset. The added inertia and damping are found using the same method for these two directions, and the total fit should be the same. Nonetheless, the position in both roll and pitch depends on the offset of the CB to the CO. Since the ROV recorded is in operation, the equipment is often changing, resulting in the CB moving. Therefore, x_b , y_b , and z_b must be adjusted to fit the logged data as good as possible.

Moreover, the position range is from -0.04 rad to 0.04 rad for roll, and from -0.15 rad to 0 rad for pitch. Smaller ranges are more difficult to map accurately, which could contribute to the less accurate fit in roll compared to pitch. However, according to Table 2.2, the recorded data should be accurate and not be an error source. Notwithstanding, the amplitude of the simulated position in roll is reduced to a value much smaller than the recorded data. The values in pitch are also reduced during the first 120 s, but the amplitude of the simulated data matches well with the recorded data.

Similar characteristics can be found when studying the velocities in roll and pitch. Roll has a better fit at the start than in the end. The period of the simulated velocity is in the same phase as the recorded data for the whole dataset. This observation indicates that the estimated added inertia is reasonable. However, the magnitude of simulated velocity best fits the first 50 s, but then the magnitude of the velocity is reduced to be smaller than the recorded data. This finding indicates that the damping may be overestimated.

The simulated velocity in pitch fits well with the recorded data. The simulated amplitude is high at the start, but because of the damping, it is reduced and matches the recorded data well after 40 s. This observation demonstrates that the estimation of the damping in pitch is reasonable.

By studying the period, it is found that the periods of the simulated pitch velocity are shorter than the recorded data at the start. This discovery indicates that the added inertia in pitch

could be underestimated. However, around 100 s, the period in both the simulated position and velocity in pitch fit well with the recorded data. This finding indicates that the ROV motions are not completely periodic. Nevertheless, this is expected since external forces influence the recorded data. It is assumed that the added inertia and damping in roll and pitch are reasonable, but the reason of a better overall fit in pitch compared to roll should be investigated.

The simulated velocity and position in yaw fit well until 35 s and 75 s. Right before 80 s, the recorded velocity has its lowest point. The simulated velocity is not able to capture the magnitude of the point. The magnitude of the velocity is close to the recorded data at the start, but at the lowest value, it is far off from the logged data. An explanation could be external forces such as the sea current and the tether. However, another explanation could be that the estimated hydrodynamic parameters are inaccurate, and the simulator code needs to be more complex and accurate.

Nonetheless, the recorded velocity consists of some sharp transitions. The simulated velocity captures these turns and is aligned at the drop at 75 s. This observation indicates that the added inertia in yaw is valid. The same method is used to obtain the added inertia and damping in the rotational directions. The general agreement between logged and simulated position and velocity in the rotational directions is acceptable, indicating that the added inertia and damping are reasonable. However, it is essential to investigate the reason for a better fit in pitch than the fit in roll and yaw.

4.5.3 Adjustment of the Hydrodynamic Parameters

Another method to obtain applicable added mass and damping is to adjust the values so the simulated position and velocity match the recorded data. This method does not necessarily find the correct added mass and damping, but it is unnecessary when the parameters are used in an ROV simulator. In this work, the end study is to check if adjusting the parameters gives a better fit with the recorded data. Therefore, all the directions are adjusted to achieve a closer fit using the CFD values as the baseline, but not all directions are presented. Figure 4.26 shows the position in heave and velocity in sway and heave using adjusted added mass and damping.

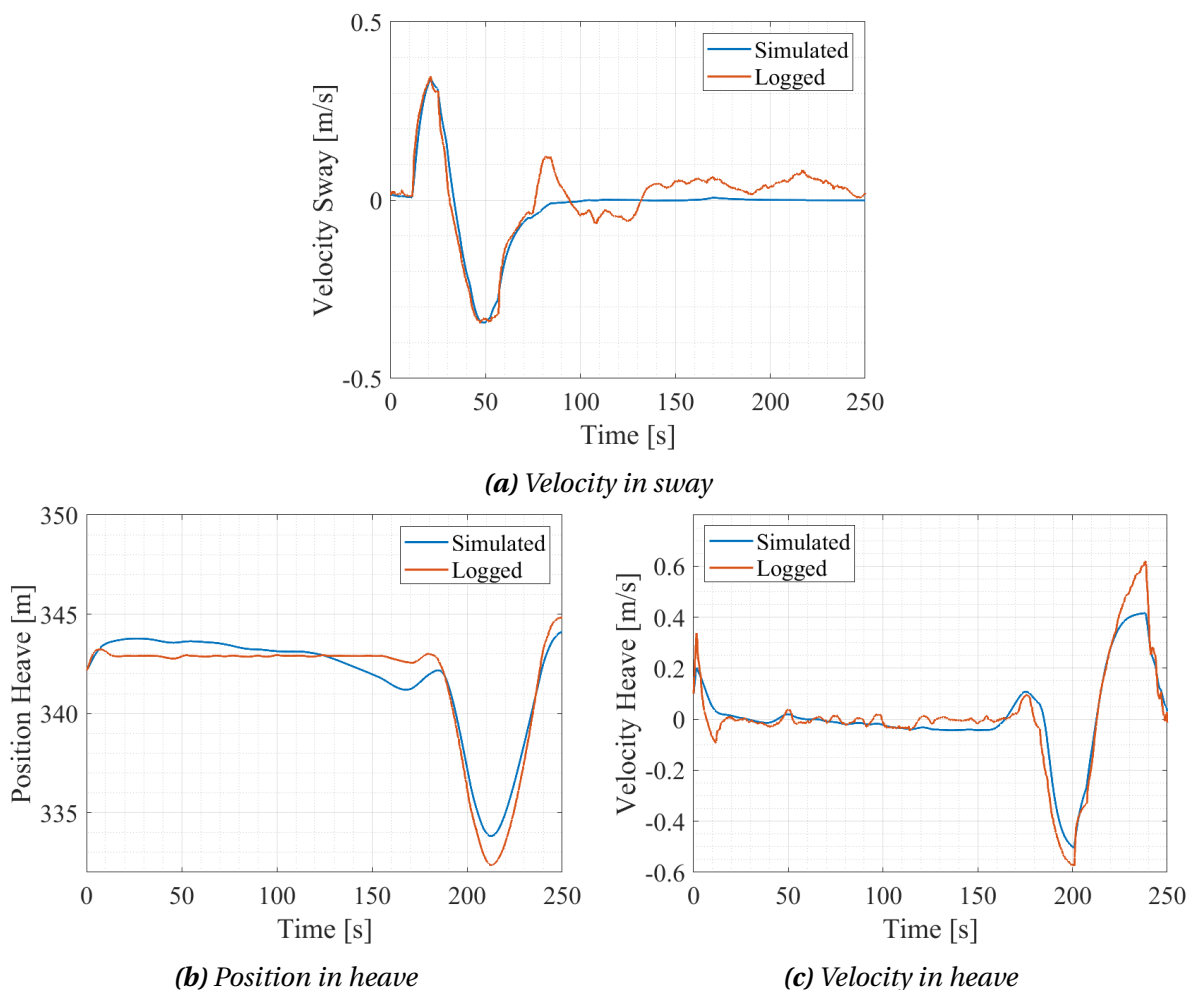


Figure 4.26: Logged and simulated data for the position in heave and velocities in sway and heave using adjusted hydrodynamic parameters

Adjusting the values in sway improves the fit with the logged data. Until 75 s, the overlap is almost identical, but after, the result is approximately the same as using the CFD estimated values. The same added mass and quadratic damping are used to achieve this result, but a linear damping of 500 Ns/m is implemented. However, other work finds that the linear damping for similar vehicles is small [2] [7] [9] [35]. An explanation could be that the linear damping recreates the extra drag from the tether and the current. However, the adjusted values cannot recreate the oscillating tendencies after 75 s. This ROV operates under a large water depth with negligible wave influence in this work. Hence, the ocean current is relatively strong at SNB and could be an explanation.

The same approach is used when adjusting the motion in heave. Here, a linear damping equal to 200 Ns/m is implemented. The challenge with the results in heave is the offset in the position in the dataset. However, this offset is flattened out and distributed by initiating linear

damping. Nevertheless, the peaks for the velocity at 202 s and 239 s do not fit as well as using only CFD estimated values.

It seems possible to improve the fit when adjusting the parameters obtained using CFD. While the improvement in sway is evident, achieving a good fit in certain aspects of heave may require compromising other areas. The peaks do not fit well when the offset at the start is flatter. However, it is assumed that a better result can be found with adjusted values using more time and a more complex simulator code. Regardless, the CFD values are relatively close to the adjusted values emphasizing that the estimated values are reasonable.

Even though the translational directions are the most important to adjust to a good fit, the rotational directions should also be studied. In Figure 4.27, the logged and simulated velocity in pitch and yaw are presented using adjusted hydrodynamic parameters.

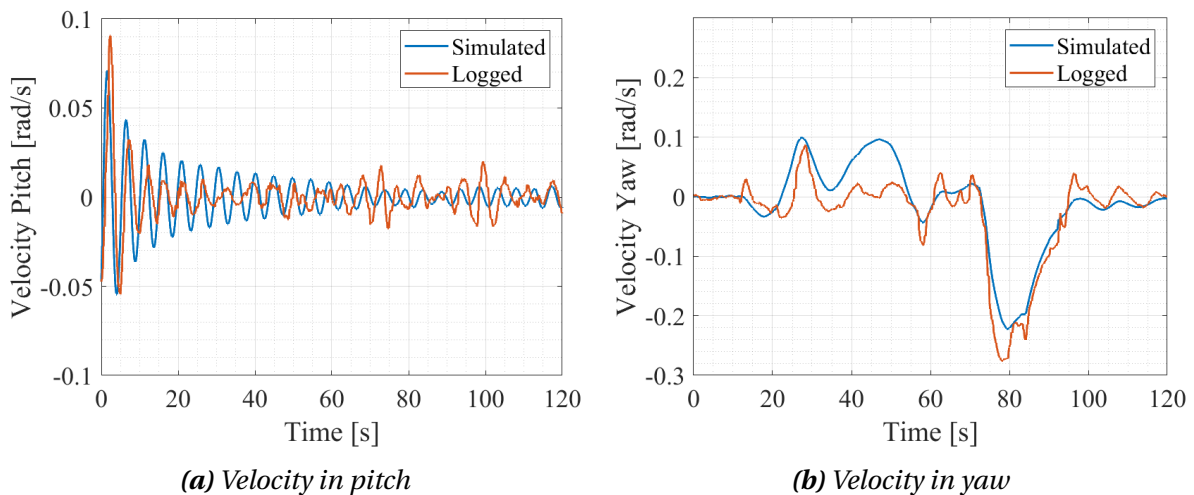


Figure 4.27: Logged and simulated data for the velocity in pitch and yaw using adjusted hydrodynamic parameters

When studying the velocity in pitch, the exact damping is used as estimated using CFD. Increasing the linear or quadratic damping makes it possible to match the amplitude at the start with the recorded data. However, the amplitude after 60 s is underpredicted. Therefore, it is assumed that the damping calculated using CFD is reasonable. In Figure 4.27b, the only change is the added inertia which is increased to $2500 \text{ kg}\cdot\text{m}^2$ to try to match the period. At the start, the period of the simulated velocity fit better with the recorded data. Despite this, after 50 s, the fitting of the periods is getting worse than using the added inertia estimated using CFD.

When adjusting hydrodynamic values in a simulator code to match recorded data, the adjusted

values are sometimes far from the estimated values. While this is the case for yaw, it does not necessarily indicate that the estimated values are incorrect. Although, after adjusting the parameters in yaw, the damping is far from the estimated values. The linear damping is set to 500 Nsm, and the quadratic damping is set to 600 Nsm. The added inertia used is the one estimated by using CFD. The lowest point of the velocity is recreated, but the velocity before is overpredicted by adjusting parameters. However, the overall fit is better using these values. This result could be because of a numerical issue due to a simplified simulator code and using high linear damping. Regardless, more recorded data in all DOF should be studied to validate the model.

4.6 Main Discussion

This work uses CFD to obtain the hydrodynamic added mass and damping. The parameters are later validated using a simulator code based on the equations of motion. Finally, the added mass and damping are adjusted to examine the applicability of the obtained parameters.

Since CFD and the equations of motion are numerical approaches, a perfect fit between the simulated movement with the recorded data cannot be expected. The overall fit with the CFD estimated parameters is satisfactory, but some deviations are not due to numerical approaches. Therefore, it is essential to discuss different sources of error for further optimization.

One of the sources could be the thrusters. The thrust conversion function is a numerical approach to determine the force corresponding to different thruster RPMs. As presented in the theory chapter, two different functions are studied. The functions are similar and present a relationship between the RPM and the thrust force. The first function is a steady-state description [23]. The second function is an evolved version with an implemented dead zone when the RPM reaches zero [24]. This work finds the best compliance by not using a dead zone. It is essential to note that a more evolved function should get a better result. However, this conversion is numerical, and not implementing a dead zone could be the most accurate for this type of vehicle and thrusters.

Another problem with the thruster conversion function is the experimental data used to determine the function. The pull tests to find the relationship between the thrust force and the RPM could be more robust. In this work, a combination of a pull test between a mounted thruster and the UCV is used. The different pull tests will exceed different forces for different RPMs. The overlap between these two tests could be better, and a more complementing pull test of the UCV could be helpful.

When logging data of the ROV, there are two different methods to read the thruster RPM. The first method is to read the measured values directly from the thrusters, and the other is to read the commanded input value. The measured values should be more accurate than the commanded input value. The commanded input RPM is the RPM the thrusters are trying to reach. Therefore, the measured value is slower than the input value. However, the measure RPM should be closer to the true RPM than the input value. Thus, the reason for the better conformity with the input RPM should be investigated. A possible reason for this could be the

RPM used in the pull tests. For the pull test of the UCV, the type of RPM is not considered. A possibility is that the input RPM is logged for the pull tests and is further used to make the thrust conversion function. If this is correct, it is reasonable that reading the input RPM in the simulator code gives a better overall fit.

There are also issues with the angles of the horizontal thrusters. All four horizontal thruster angles are 45° relative to the x- and y-axis. When performing different movements, turbulent flow from the thrusters will interfere with each other. An example is when the ROV moves forward, the wake from the thrusters in front will inflict the thrusters in the back. This disturbance may cause a force loss, and this phenomenon should be investigated.

The ROV skid is a prominent type of equipment often mounted on the ROV. However, the skid is not considered when performing the CFD simulations. In addition, the recorded data used are from 2021, before the present investigations were started, and detailed information of the ROV skid is missing. If the skid is considered in the CFD calculations, the damping and added mass will likely increase, especially in surge and sway. Since the skid is mounted on the bottom of the ROV, the damping and added mass in the heave would not be significantly affected. These factors could also explain the overprediction of the simulated velocity in surge and sway, but the velocity in heave is underpredicted. However, the main components are assumed to be considered when estimating the hydrodynamic parameters.

The buoyancy, total weight, and offset of the CB to the CO are unknown because the ROV is in operation. The weight, buoyancy, and the offset of the CB to the CO, x_b , y_b , and z_b are adjusted for the simulated data to match the recorded data as good as possible. There are mainly two possible outcomes of this method. The first outcome is that the overall fit could be better if the exact value of the different parameters is known. The other outcome is that the values of the parameters are over-adjusted, and the simulated data fit the recorded data better than it should. The overall fit found with the CFD estimated and adjusted hydrodynamic parameters could be off from the true fit. However, the adjusted buoyancy, weight, and offset are close to the initial estimation, indicating the accuracy [1]. Therefore, the gravitational and buoyancy forces are not vital sources of error. Nonetheless, it is necessary to conduct data recording using a UCV with known equipment to ensure accurate buoyancy estimation.

The uncertainty of the experimental logged data should also be questioned. The SPRINT is highly accurate and should be sufficiently accurate for this application. This assumption is

supported when comparing the logged and simulated data. The deviation shown in Table 2.2 for the SPRINT is minimal and will not affect the overall fit. However, since there are problems with the same SPRINT in 2023, there is no guarantee that similar errors were not present in 2021 for the dataset studied in this work. Therefore, the SPRINT should be fixed, and new data should be logged to validate the numerical estimated parameters.

The CFD results fit the recorded data in most of the investigated directions. This observation indicates that the results are satisfactory, but not for all directions. The deviations can be explained with proper augmentations, but the CFD results should also be investigated.

One crucial factor that could influence the estimation of the hydrodynamic parameters is the simplification of the ROV. The side plates are studied, and the plates increase the drag when directly exposed to the flow. Other details of the ROV should be studied to determine if they influence the flow around the ROV. An example is the thin plates in the back of the ROV. However, finding a perfect simplification of the ROV without discrepancies is difficult. Nevertheless, the estimated values are likely close to the actual values of the UCV and are sufficiently accurate for engineering purposes.

The base of the different simulations is built on reliable research of lab tests and belonging CFD simulations. Nevertheless, the method and results of some of the simulations can be criticized. The overall results of the rotating arm simulations are good, but there are struggles with instability. By comparing the velocity contour plot and the quadratic fit of the rotational direction, it is clear that the flow is more stable in pitch. The reason can be connected to the geometry of the ROV, the domain, and the mesh. However, a domain and mesh convergence study has been carried out to exclude this as a factor. At the same time, little research is available for rotating arm simulations, and it could be reasonable to perform the present simulations.

The PMM simulations for pitch and yaw do not follow the conventional procedure. According to other literature, the paths should be tangential [8] [27]. However, a tangential path is not currently considered because the ROV is a slow-moving vehicle, and the rotational angle is small. Therefore, the difference in added inertia should be checked for a pure pitch and yaw for the ROV. Simultaneously, lower frequencies should be studied when estimating the added mass and inertia to achieve the most accurate result [28]. However, several frequencies are tested, and the added mass and inertia is constant or all DOF. In addition, simulating lower

frequencies demand higher computational power, which is nonsensical with the already long runtime.

Regardless, the results should be validated with experiments in a controlled environment. There is much expensive work to validate these parameters in labs, but it is arguably the most accurate method. The present study can provide an efficient and cheap solution, and the CFD predictions combined with the adjusted values can give a generally good fit with the actual data.

Another factor in the final results could be the simulator code itself. The code is built on the equations of motions and numerical solve the movement of the ROV using a Runge–Kutta method. In addition, the equation itself is simplified to be easier to solve. Only the diagonal parameters of the added mass and damping matrices are assessed by considering different assumptions. All the parameters in these matrices should be estimated, which should be possible with the data from the CFD in this work. In addition, the Coriolis matrix should be considered to improve the simulator code.

Nevertheless, the agreement between logged and simulated position and velocity is acceptable. Therefore, the numerical results of the damping and added mass are reasonable.

(This page is intentionally left blank)

Chapter 5

Conclusion

In this work, the hydrodynamic added mass and damping of all DOF of an ROV are obtained using CFD. Furthermore, the CFD estimated parameters are validated by comparing the simulator code with recorded data. Then, the hydrodynamic parameters are adjusted to evaluate if a more accurate fit between simulated and recorded data is achievable. Firstly, the thin side plates of the UCV are studied. The plates increase the drag by 15 % in sway when the plates are directly exposed to the flow. It is assumed that they influence the added mass and damping when there is an acceleration or constant flow in sway, roll, or yaw.

Compared with published studies, the simulations to obtain the damping in the translational directions are stable and reasonable. The smallest damping is found in surge, which is almost twice as large in sway and heave. In sway and heave, the cross-section area is also larger than surge. Nevertheless, the quadratic damping part of the equation strongly dominates the damping for the translational directions. The damping in rotational directions is primarily stable but should be further investigated. The quadratic damping part of the equation also strongly influences these directions. The estimation of the added mass and inertia is also reasonable compared with other published studies, even though a pure pitch and yaw are not achieved.

The equations of motion are programmed and simulated using a Runge-Kutta method in MATLAB. The overall fit is good when comparing the simulated movement using CFD estimated added mass and damping to the logged data. The match with the logged data is not perfect for all directions, but CFD is a reliable tool for accurately estimating the hydrodynamic added mass and damping.

Simultaneously, the fit between simulated and recorded data using adjusted added mass and damping is arguably more accurate. In addition, adjusting the values are more efficient when recorded data of the ROV are available. The hydrodynamic parameters found using CFD may be closer to the actual added mass and damping, but it is not important when developing an ROV simulator. The primary objective is to achieve the most accurate fit between the simulated and actual movements.

Therefore, adjusting the added mass and damping can be more efficient if recorded data is available. However, recorded data will not be available if the goal is to make a digital prototype of an ROV, but the CFD estimated parameters are sufficiently accurate. The proposal of a new ROV can then be investigated better and more efficiently.

5.1 Suggestions for Future Work

The equivalent lab tests, towing tank, rotating arm, and PMM should be carried out to verify the hydrodynamic parameters individually. The reason is to exclude all the external forces at SNB and the unknown factor of a daily operating ROV.

The simulations should also be investigated further, and a detailed validation study should be carried out for the rotating arm simulations. There have been instances of instability, and the reason should be identified. Simultaneously, a coupled motion for pitch and yaw should be simulated to achieve a pure motion. The new simulations should be compared with the present estimated hydrodynamic parameters.

The ROV has been simplified to allow for efficient CFD simulations. However, it is difficult to judge whether the simplifications accurately replicate the flow of the real ROV. The UCV is a highly detailed ROV, and large equipment has been removed in the simplification process. As this work found, the small thin side plates influence the drag of the ROV. In the back of the ROV, smaller thin plates are installed. The effect of these plates should be studied together with other larger equipment, such as the thrusters and the skid.

CFD is a method that demands high computational power. The damping simulations have a short runtime since steady-RANS is implemented. However, unsteady-RANS is used for the PMM simulations, increasing the computational runtime. The PMM simulations may be accurate and well-documented in the literature. However, the efficiency should be improved. Therefore, other more efficient methods should be investigated.

To check if there is possible to achieve a better fit with the simulator code, a more complete equation should be implemented. The added mass and damping matrix are simplified, and only the diagonal parameters are used. All the parameters in these matrices should be included to improve the simulator. Simultaneously, the Coriolis matrix should be included.

Many external factors influence the operational ROV. However, some factors should be studied to see if they can be reduced or predicted. The drag from the tether and ocean current is assumed to be the most prominent external forces. Therefore, these forces should be investigated to find how much they influence the movement of the ROV.

(This page is intentionally left blank)

References

- [1] IKM Subsea. Personal communication of non-published data, 2022-09-26.
- [2] C. S. Chin, W. P. Lin, and J. Y. Lin. Experimental validation of open-frame ROV model for virtual reality simulation and control. *Journal of Marine Science and Technology (Japan)*, 23(2):267–287, 2018.
- [3] L. M. Knausgård. Development of DP System for Merlin WR200 ROV. Master's thesis, Norwegian University of Science and Technology, 2013.
- [4] IKM Subsea. Merlin ucv. <https://www.ikm.com/getfile.php/1340886-1553600603/IKM%20Selskaper/IKM%20Subsea/Data%20Sheets/Merlin%20UCV%20productsheet%20.pdf>. Accessed: 2023-01-26.
- [5] IKM Subsea. Our Products & Services - IKM Subsea. <https://www.ikm.com/ikm-subsea/products/services/electrical-rov-fleet>. Accessed: 2023-01-26.
- [6] S. Skorpa. Numerical Simulation of Flow Around Remotely Operated Vehicle (ROV). Master's thesis, Norwegian University of Science and Technology, 2012.
- [7] Q. Li, Y. Cao, B. Li, D. M. Ingram, and A. Kiprakis. Numerical modelling and experimental testing of the hydrodynamic characteristics for an open-frame remotely operated vehicle. *Journal of Marine Science and Engineering*, 8(9):1–15, 2020.
- [8] L. Hong, X. Wang, D. Zhang, and H. Xu. Numerical Study on Hydrodynamic Coefficient Estimation of an Underactuated Underwater Vehicle. *Journal of Marine Science and Engineering*, 10(8), 2022.
- [9] A. Hammoud, J. Sahili, M. Madi, and E. Maalouf. Design and dynamic modeling of ROVs: estimating the damping and added mass parameters. *Ocean Engineering*, 239, 2021.

- [10] S. F. Hoerner. *Fluid-Dynamic Drag*. Hoerner Fluid Dynamics, Bricktown New Jersey, 1965.
- [11] J. Bartl, K. F. Sagmo, T. Bracchi, and L. Sætran. Performance of the NREL S826 airfoil at low to moderate Reynolds numbers—A reference experiment for CFD models. *European Journal of Mechanics, B/Fluids*, 75:180–192, 2019.
- [12] Y. A. Çengel and J. M. Cimbala. *FLUID MECHANICS Fundamentals and Applications*. McGraw-Hill Education, 2006.
- [13] OpenFOAM. User guide. <https://www.openfoam.com/documentation/user-guide>. Accessed: 2022-11-21.
- [14] O. Reynolds. On the dynamical theory of incompressible viscous fluids and the determination of the criterion. *Philosophical Transactions of the Royal Society of London*, 1895.
- [15] G. Alfonsi. Reynolds-averaged Navier-Stokes equations for turbulence modeling. *Applied Mechanics Reviews*, 62(4):1–20, 2009.
- [16] F. R. Menter, M. Kuntz, and R. Langtry. Ten years of industrial experience with the sst turbulence model. *Heat and Mass Transfer*, 4:625–632, 01 2003.
- [17] OpenFOAM. k-omega shear stress transport (sst). <https://www.openfoam.com/documentation/guides/latest/doc/guide-turbulence-ras-k-omega-sst.html>. Accessed: 2022-12-16.
- [18] D. B. Spalding. A single formula for the “law of the wall”. *Journal of Applied Mechanics, Transactions ASME*, 28(3):455–458, 1960.
- [19] Wikipedia. Law of the wall. https://en.wikipedia.org/wiki/Law_of_the_wall. Accessed: 2022-12-16.
- [20] OpenFOAM. nutuspaldingwallfunction. <https://www.openfoam.com/documentation/guides/latest/doc/guide-bcs-wall-turbulence-nutUSpaldingWallFunction.html>. Accessed: 2022-11-17.
- [21] T. I. Fossen. *HANDBOOK OF MARINE CRAFT HYDRODYNAMICS AND MOTION CON-*

- TROL*. John Wiley & Sons, Chichester, West Sussex, 2011.
- [22] I. Masmitja, J. Gonzalez, C. Galarza, S. Gomariz, J. Aguzzi, and J. del Rio. New vectorial propulsion system and trajectory control designs for improved AUV mission autonomy. *Sensors (Switzerland)*, 2018.
- [23] D. R. Yoerger, J.G. Cooke, and J. E. Slotine. The influence of thruster dynamics on underwater vehicle behavior and their incorporation into control system design. *IEEE Journal of Oceanic Engineering*, 15(3):167–178, 1990.
- [24] W. M. Bessa, M. S. Dutra, and E. Kreuzer. Thruster dynamics compensation for the positioning of underwater robotic vehicles through a fuzzy sliding mode based approach. *ABCM Symposium in Mechatronics*, 2(1990):605–612, 2006.
- [25] T.Sarpkaya. *Hydrodynamic Damping*, page 265–284. Cambridge University Press, 2010.
- [26] J. N. Newman. *Marine Hydrodynamics*. The MIT Press, 1977.
- [27] S. A. Malik and P. Guang. Transient numerical simulations for hydrodynamic derivatives predictions of an axisymmetric submersible vehicle. *Research Journal of Applied Sciences, Engineering and Technology*, 5(21):5003–5011, 2013.
- [28] S. Ardeshiri, H. Mousavizadegan, and S. Kheradmand. Virtual simulation of PMM tests independent of test parameters. *Brodogradnja*, 71(2):55–73, 2020.
- [29] Sonardyne International Limited. User manual for type 8253 sprint 3rd generation. Issue A Rev 2, 2018.
- [30] Sonardyne International Limited. Datasheet sprint-nav. https://www.sonardyne.com/wp-content/uploads/2021/07/Sonardyne_8253_SPRINT_Nav.pdf. Accessed: 2023-02-07.
- [31] Valeport Limited. Model 803 ECM Operating Manual. <https://www.valeport.co.uk/content/uploads/2020/03/Model-803-EM-Current-Meter-Operating-Manual-0803805i.pdf>. Accessed: 2023-02-23.
- [32] Valeport Limited. Model 803 - roV current meter. <https://www.valeport.co.uk/content/uploads/2020/04/Model-803-ROV-Current-Meter-Datasheet-April-202>

- 0.pdf. Accessed: 2023-02-24.
- [33] B. Zhao, Y. Yun, F. Hu, J. Sun, D. Wu, and B. Huang. Hydrodynamic coefficients of the DARPA SUBOFF AFF-8 in rotating arm maneuver: Part I: Test technology and validation. *Ocean Engineering*, 266, 2022.
- [34] F. Juretic. cfMesh User Guide. http://cfmesh.com/wp-content/uploads/2015/09/User_Guide-cfMesh_v1.1.pdf. Accessed: 2022-09-28.
- [35] R. Yang, B. Clement, A. Mansour, M. Li, and N. Wu. Modeling of a Complex-Shaped Underwater Vehicle for Robust Control Scheme. *Journal of Intelligent and Robotic Systems: Theory and Applications*, 80(3-4):491–506, 2015.
- [36] X. Wu, Y. Wang, C. Huang, Z. Hu, and R. Yi. An effective CFD approach for marine-vehicle maneuvering simulation based on the hybrid reference frames method. *Ocean Engineering*, 109:83–92, 2015.
- [37] S. Tang, T. Ura, T. Nakatani, B. Thornton, and T. Jiang. Estimation of the hydrodynamic coefficients of the complex-shaped autonomous underwater vehicle TUNA-SAND. *Journal of Marine Science and Technology*, 14:373–386, 2009.

